

The Pennsylvania State University

The Graduate School

**CFD MODELING OF PARTICLE INGESTION DAMAGE AND ITS
IMPACT ON MULTISTAGE AXIAL COMPRESSOR
PERFORMANCE**

A Dissertation in
Mechanical Engineering

by

Emanuel Chirayath

© 2023 Emanuel Chirayath

Submitted in Partial Fulfillment
of the Requirements
for the Degree of

Doctor of Philosophy

December 2023

The dissertation of Emanuel Chirayath was reviewed and approved by the following:

Robert Kunz

Professor of Mechanical Engineering

Director of Graduate Studies

Dissertation Advisor, Chair of Committee

Karen Thole

Professor of Mechanical Engineering

John Cimbala

Professor of Mechanical Engineering

Elia Merzari

Professor of Nuclear Engineering

Abstract

The damage due to particulate matter ingestion by propulsion gas turbine engines can be significant, impacting the operability and performance of compressor, combustor and turbine components. Here, focus is on the axial compressor whose blades become damaged when operated in dusty/sandy environments for extended periods of time. This results in significant performance degradation of the compressor and hence, the entire plant. Accordingly, prediction of the impact of specific particle damage morphologies on compressor aerodynamics can be of significant benefit to aircraft operators concerned with fuel efficiency and on-wing platform readiness.

In this work, novel CFD methods are developed aimed at modeling the effects of particle ingestion airfoil damage on axial compressor performance. Specifically, the goal of the research is aimed at mechanistic (vs. empirical) prediction of the significant aero-thermodynamic, and attendant loss implications, for a range of damage morphologies. To this end, we study the first stage rotor blading of a GE T700-401C compressor. This five-stage axial machine is subject to current testing at NAVAIR, in a well instrumented facility. A secondary goal of this thesis research is to provide physics understanding and pre-test predictions associated with damage modes that have been observed in these systems.

In this work, thermoplastic additive manufacturing is used to build a number of baseline undamaged stage 1 rotor blades, and then heat and tooling treatments are applied to obtain representative physical models of three of these modes – ballistically bent/curved leading edges, spanwise cragged erosion of leading edges, and eroded leading/tailing edges at outer span locations. The resultant damaged plastic geometries are then optically scanned and incorporated into sublayer resolved Reynolds Averaged Navier-Stokes (RANS) analysis. Target conditions are imposed that conform to damaged compressor operation protocols, and an iterative process for accommodating corrected mass flow and off-design powering is developed and presented.

The code, modeling and meshing strategies pursued here are validated, using a study carried out for NASA Rotor 37 – these results are included and provide

confidence in the predictions of the T700 geometry studied.

The results for the steady-state calculations for the rotor only configuration, in the rotating frame of reference, are presented in terms of compressible wave field and secondary/tip flows, spanwise performance parameter distributions and efficiency. A method to estimate the effect of rotor damage on engine SFC is devised and presented. This enabled the rank ordering of the different damage modes in terms of the overall performance parameters.

Time accurate rotor-stator calculations are then performed for the full stage configuration. These results are also presented in terms of compressible wave field and secondary/tip flows, spanwise performance parameter distributions, efficiency and estimated impact on plant Specific Fuel Consumption (SFC). The different damage modes are classified based on the overall performance parameters. Relevant observations include significant differences between the steady state rotor only calculations and the full stage unsteady calculations with different damage morphologies.

A combined Eulerian-Lagrangian methodology was also deployed on the axial compressor configuration in this research, in order to initiate a "full-field" simulation approach wherein the damage process itself is modelled. Method validation is performed using a well-documented data-set for sand in air erosion at high Reynolds number. The results are presented in terms of eroded surface profiles and eroded surface time evolution history and conclusions are made. A qualitative assessment of the impact of erosion on the NASA Rotor 37 blade surface is performed and discussed. Assessments and recommendations for future multiphase flow damage modeling are made.

Table of Contents

| | |
|---|-------------|
| List of Figures | viii |
| List of Tables | xv |
| List of Symbols | xvi |
| Acknowledgments | xx |
| Chapter 1 | |
| Introduction | 1 |
| 1.1 Overview | 1 |
| 1.2 Literature Review | 2 |
| 1.3 Outline of Dissertation | 23 |
| Chapter 2 | |
| Technical Approach | 25 |
| 2.1 Methodology | 25 |
| 2.1.1 Geometry | 25 |
| 2.1.2 Damaged Blades | 27 |
| 2.1.3 Meshing Strategy | 30 |
| 2.1.4 Simulation Parameters and Boundary Conditions | 32 |
| 2.1.5 Grid Independence Studies | 34 |
| 2.1.5.1 Rotor 37 | 34 |
| 2.1.5.2 T700 | 35 |
| 2.1.6 Target Operating Conditions | 35 |
| 2.2 Method Validation - NASA Rotor 37 | 39 |
| 2.2.1 Conclusion - Method Validation | 43 |
| Chapter 3 | |
| Steady-State Rotor only Simulations | 44 |
| 3.1 Computational Domain and Simulation Parameters | 44 |

| | | |
|------------------|---|------------|
| 3.2 | Results | 46 |
| 3.2.1 | Undamaged Rotor | 46 |
| 3.2.2 | Damaged Configurations | 49 |
| 3.2.3 | Impact on SFC | 57 |
| | | |
| Chapter 4 | | |
| | Unsteady Full Stage Simulations | 61 |
| 4.1 | Computational Domain and Simulation Parameters | 61 |
| 4.2 | Results | 63 |
| 4.2.1 | Undamaged Stage | 63 |
| 4.2.2 | Damaged Configurations | 69 |
| 4.2.3 | Impact on SFC | 79 |
| 4.3 | Results Comparison - Full Stage and Half Stage calculations | 80 |
| | | |
| Chapter 5 | | |
| | Erosion Modeling Due to Particle Ingestion | 86 |
| 5.1 | Lagrangian Multiphase Simulation | 87 |
| 5.2 | Description of the Method Validation Case | 87 |
| 5.3 | Technical Approach | 90 |
| 5.3.1 | Computational Domain and Boundary Conditions | 93 |
| 5.3.2 | Meshing Strategy | 94 |
| 5.3.3 | Eulerian Modeling of Fluid Phase | 95 |
| 5.3.4 | Lagrangian Modeling of Particle Phase | 95 |
| 5.3.5 | Force Models | 97 |
| 5.3.6 | Particle Injection | 99 |
| 5.3.7 | Erosion Models | 100 |
| 5.3.8 | Coefficients of Restitution | 102 |
| 5.3.9 | Grid Independence Study | 103 |
| 5.4 | Results | 105 |
| 5.4.1 | Method Validation Case | 105 |
| 5.4.2 | Erosion Characterization of NASA Rotor 37 Blade Surface | 114 |
| 5.4.3 | Erosion Coupled Deformation of NASA Rotor 37 Blade Surface | 119 |
| | | |
| Chapter 6 | | |
| | Summary and Future Work | 123 |
| 6.1 | Summary | 123 |
| 6.2 | Original Contributions of this Dissertation | 125 |
| 6.3 | Scope for Future Work | 127 |
| 6.3.1 | Full annulus CFD simulations of the T700 | 128 |
| 6.3.2 | CFD simulation with real damaged blades | 129 |

| | | |
|-------|---|-----|
| 6.3.3 | Time-dependent erosion models | 129 |
| 6.3.4 | Deposition Damage and Surface Roughness | 130 |

Appendix A

| | |
|---|------------|
| Averaging Techniques | 132 |
| A.1 Averaging of Stagnation Temperature | 132 |
| A.2 Averaging of Stagnation Pressure | 133 |

| | |
|---------------------|------------|
| Bibliography | 134 |
|---------------------|------------|

List of Figures

| | | |
|------|---|----|
| 1.1 | Concentration of airborne particles smaller than $2.5\mu\text{m}$ [6] | 3 |
| 1.2 | A view of sand being ingested into a C-17 at take-off [9] | 4 |
| 1.3 | Eroded blades of the HPC rotor of the JTD9 after different stages of operation [15] | 6 |
| 1.4 | Erosion of the rotor pressure side and tip region by sand ingestion [16] | 6 |
| 1.5 | Profile erosion of 16 th stage rotor blade at 80% span (left), erosion of tip region of 13 th stage rotor blade (right) [17] [18] | 7 |
| 1.6 | Undamaged blade (left), blade with nick (middle), blade with bend (right) [20] | 8 |
| 1.7 | Erosion patterns of the rotor blade, pressure side (left), suction side (right) [21] | 9 |
| 1.8 | Stagnation pressure ratio vs mass flow characteristics at 70 percent span for the different roughness configurations in the study [22] | 11 |
| 1.9 | Salt deposits at the leading edge of the second-stage stator vanes [26] | 13 |
| 1.10 | Examples of fouled compressor blades: (a) Heavily-fouled air inlet bell-mouth and blading on a 35 MW gas turbine; (b) Oily deposits on blading; (c) Compressor blades fouled with a mixture of salts and oil [28] | 14 |

| | | |
|------|---|----|
| 1.11 | Magnified images of sample surfaces post sand impact study: cut features on the sample surface (top), platelet features on sample surface (bottom) [32] | 16 |
| 1.12 | Fouling of the IGV blade: (a) Pressure side (b) Suction side [35] . . . | 17 |
| 1.13 | Comparison of erosion patterns: Experimental (left), CFD (right) [41] | 19 |
| 1.14 | Erosion patterns of the first stage rotor [42] | 19 |
| 1.15 | Time evolution of deformed pipe geometry due to erosion [52] | 22 |
| 2.1 | A sectional view of the T700 engine [56] | 26 |
| 2.2 | Two views of the T700 first stage rotor blade | 26 |
| 2.3 | Creality 3D Ender-3 V2 3D printer | 27 |
| 2.4 | Scanned geometry before cleanup (left), CFD ready geometry (right) | 28 |
| 2.5 | Original [12] and 3D printed blades with Cragged damage | 29 |
| 2.6 | Original [12] and 3D printed blades with the Eroded damage | 29 |
| 2.7 | Original [12] and 3D printed blades with the Curled damage | 30 |
| 2.8 | A 3D view of the mesh used for the Rotor 37 validation study | 31 |
| 2.9 | Top view of the mesh used for the Rotor 37 validation study at 50% span | 32 |
| 2.10 | Velocity triangles at design point (left), off-design point (at increased Ω) (right) | 37 |
| 2.11 | $\frac{\Delta v_{\theta,f}}{\Delta v_{\theta,i}}$ vs. $\frac{\Omega_f}{\Omega_i}$ for five selected compressor shaft speeds in range of interest and linear fit | 38 |
| 2.12 | Rotor 37 instantaneous relative Mach number contours at 70% span | 41 |

| | | |
|------|--|----|
| 2.13 | Rotor 37 spanwise distribution of stagnation temperature ratio at the outlet | 42 |
| 2.14 | Rotor 37 spanwise distribution of stagnation pressure ratio at the outlet | 43 |
| 3.1 | A view of the computational domain for the rotor only simulation | 45 |
| 3.2 | A view of the full stage computational domain at 50% span | 45 |
| 3.3 | Relative Mach number contours at 90% span of the Undamaged case | 46 |
| 3.4 | Relative Mach number contours at $(x/c)_{hub} = 0.27$; Undamaged | 47 |
| 3.5 | Tip clearance gap streamlines of Undamaged case with contours of vorticity at several planes downstream | 48 |
| 3.6 | Streamlines in the tip clearance gap region with contours of relative Mach number at 98% span for the Undamaged case | 49 |
| 3.7 | Relative Mach number contours at 90% span; undamaged (left), Cragged damage (right) | 50 |
| 3.8 | Relative Mach number contours at 90% span; undamaged (left), Eroded damage (right) | 51 |
| 3.9 | Relative Mach number contours at 90% span; undamaged (left), Curled damage (right) | 52 |
| 3.10 | Instantaneous relative stagnation pressure contours at $(x/c)_{hub} = 0.66$; Undamaged (top-left), Eroded (bottom-left), Cragged (top-right), Curled (bottom-right) | 53 |
| 3.11 | Spanwise distribution of normalized stagnation temperature ratio at the outlet | 55 |
| 3.12 | Spanwise distribution of normalized stagnation pressure ratio at the outlet | 55 |

| | | |
|------|--|----|
| 3.13 | Spanwise distribution of absolute flow angle at the outlet | 56 |
| 3.14 | Spanwise distribution of normalized adiabatic efficiency at the outlet | 57 |
| 3.15 | Side cut-away view of T700 compressor section [56] | 58 |
| 3.16 | Normalized SFC vs Normalized Stage 1 Adiabatic Efficiency | 60 |
| 3.17 | Normalized SFC vs Normalized Compressor Pressure Ratio | 60 |
| 4.1 | A view of the full stage computational domain | 62 |
| 4.2 | A view of the mesh for the Undamaged case at 50% span | 62 |
| 4.3 | Instantaneous relative Mach number contours at 90% span of the Undamaged case | 64 |
| 4.4 | Instantaneous relative Mach number contours at $(x/c)_{hub} = 0.27$: Undamaged | 65 |
| 4.5 | Tip clearance gap streamlines of Undamaged case with contours of relative velocity at several axial planes in the passage | 66 |
| 4.6 | Streamlines in the tip clearance gap region with contours of relative velocity at 98% span | 67 |
| 4.7 | Spanwise distributions of time-averaged normalized STR (left) and normalized SPR (right) with min-max values for the Undamaged case | 68 |
| 4.8 | Instantaneous relative Mach number contours at 90% span; Undam- aged (left), Cragged damage (right) | 69 |
| 4.9 | Instantaneous relative Mach number contours at 90% span; Undam- aged (left), Eroded damage (right) | 70 |
| 4.10 | Instantaneous relative Mach number contours at 90% span; Undam- aged (left), Curled damage (right) | 72 |

| | | |
|------|--|----|
| 4.11 | Instantaneous relative stagnation pressure contours at $(x/c)_{hub} = 0.66$; Undamaged (top-left), Eroded (bottom-left), Cragged (top-right), Curled (bottom-right) | 73 |
| 4.12 | Tip clearance gap streamlines with contours of relative velocity at several axial planes in the passage: Eroded (top), Curled (bottom) . | 74 |
| 4.13 | Spanwise distribution of normalized adiabatic efficiency at the stator outlet | 76 |
| 4.14 | Spanwise distribution of normalized stagnation temperature ratio at the stator outlet | 77 |
| 4.15 | Spanwise distribution of normalized stagnation pressure ratio at the stator outlet | 78 |
| 4.16 | Spanwise distribution of normalized absolute flow angle at the rotor-stator interface | 78 |
| 4.17 | Normalized SFC vs Normalized Stage 1 Adiabatic Efficiency | 79 |
| 4.18 | Normalized SFC vs Normalized Compressor Pressure Ratio | 80 |
| 4.19 | Comparison of relative Mach number contours at 90% span for the Eroded case: steady rotor only (left), unsteady full stage (right) . . | 81 |
| 4.20 | Comparison of relative Mach number contours at 90% span for the Curled case: steady rotor only (left), unsteady full stage (right) . . | 82 |
| 4.21 | Normalized STR at the rotor-stator interface for each case | 83 |
| 4.22 | Normalized SPR at the rotor-stator interface for each case | 84 |
| 5.1 | 3D surface profilometer measurement of the sample for 90° impact angle [48] | 89 |
| 5.2 | Surface profile evolution history of the sample for 90° impact angle [48] | 90 |
| 5.3 | Flowchart of the methodology employed for the erosion studies . . . | 92 |

| | | |
|------|---|-----|
| 5.4 | CFD domain for the method validation case | 93 |
| 5.5 | CFD domain for the method validation case | 94 |
| 5.6 | Definition of a parcel and its interaction with the wall [59] | 96 |
| 5.7 | Surface profiles of the sample at 30s of erosion for the different grids | 104 |
| 5.8 | Mid-section view of velocity magnitude contours of the fluid phase . | 106 |
| 5.9 | Mid-section view of the velocity vectors: fluid phase (left), particle phase (right) | 107 |
| 5.10 | Sample surface contours of time-averaged eroded depth at 30s of erosion for a single realization | 107 |
| 5.11 | Comparison of ensemble averaged surface profiles using 2 to 6 real- izations | 108 |
| 5.12 | Comparison of ensemble averaged surface profiles using 6 to 10 realizations | 109 |
| 5.13 | Comparison of ensemble averaged sample surface profile at 30s of erosion | 110 |
| 5.14 | Ensemble averaged sample surface contours of eroded depth at 30s of erosion | 111 |
| 5.15 | Comparison of ensemble averaged sample surface profile at 60s of erosion | 112 |
| 5.16 | Comparison of ensemble averaged sample surface profile at 120s of erosion | 112 |
| 5.17 | Comparison of time evolution history of maximum depth of cut of the sample surface | 113 |
| 5.18 | Cumulative distribution of sand particle size as per MIL-E-5007E [92] | 115 |
| 5.19 | Surface erosion patterns on blade pressure side of NASA Rotor 37 . | 116 |

| | | |
|------|--|-----|
| 5.20 | Surface erosion patterns on blade suction side of NASA Rotor 37 . . | 117 |
| 5.21 | A close up view of surface erosion patterns on leading (left) and trailing (right) edges of NASA Rotor 37 | 118 |
| 5.22 | A close up view of surface erosion patterns on the shroud (left) and hub (right) of NASA Rotor 37 | 119 |
| 5.23 | Surface erosion patterns on the section of Rotor 37, pressure side (top), suction side (bottom) | 120 |
| 5.24 | Surface erosion patterns on the section of Rotor 37, leading edge (left), trailing edge (right) | 121 |
| 5.25 | Pressure side leading edge of Rotor 37, before damage (top), after damage (bottom) | 122 |
| 6.1 | Different examples of deposition of particulate matter on axial compressor blades [12] | 130 |

List of Tables

| | | |
|-----|---|-----|
| 2.1 | Results - Grid Independence Study - Rotor 37 | 35 |
| 2.2 | Results - Grid Independence Study - T700 | 36 |
| 2.3 | Rotor 37 overall performance parameters | 40 |
| 3.1 | Comparison of Overall Performance Parameters | 54 |
| 4.1 | Comparison of Overall Performance Parameters | 75 |
| 5.1 | Particle size distribution for 90 mesh sand | 88 |
| 5.2 | Maximum depth of cut for sample at 90° impact angle [48] | 89 |
| 5.3 | Erosion Model Comparison | 101 |
| 5.4 | Values of A_i in angle function $F(\theta)$ in DNV model [88] | 102 |
| 5.5 | Results - Grid Independence Study - Validation Case | 104 |

List of Symbols

Roman Letters

A_p Projected area of particle

c Axial chord length

CoR_{norm} Normal coefficient of restitution

CoR_{tang} Tangential coefficient of restitution

CPR Compressor Pressure Ratio

C_D Drag coefficient

C_{vm} Virtual mass coefficient

$crag$ Cragged rotor 1 stage

$curl$ Curled rotor 1 stage

d^* Erosion model reference diameter

$erod$ Eroded rotor 1 stage

E Weight loss of the target material

ER Reference erosion ratio

ER_V Volumetric erosion rate

ER_{90} Volumetric erosion rate at normal impact angle

F_B Body forces

| | |
|----------------------|--|
| F_C | Contact forces |
| F_D | Drag force |
| F_P | Force due to pressure gradients |
| F_S | Surface forces |
| $F(\theta)$ | Angle function |
| F_{vm} | Virtual mass force |
| h_0 | Specific stagnation enthalpy |
| $\Delta h_{0,k}$ | Stagnation enthalpy rise for stage k |
| $\Delta h_{0,1,tgt}$ | Target $\Delta h_{0,k}$ for stage 1 |
| HPC | High Pressure Compressor |
| H_V | Vicker Hardness value |
| K | Erosion model constant, particle property factor |
| k_1 | Hardness exponent |
| k_2 | Velocity exponent |
| k_3 | Diameter exponent |
| LE | Leading Edge |
| LPC | Low Pressure Compressor |
| \dot{m} | Mass flow rate |
| \dot{m}_c | Mass flow rate at choke |
| m_p | Mass of particle |
| M_p | Total mass of impacting particles |
| n | Erosion model exponent |
| n_1 | Angle exponent 1 |
| n_2 | Angle exponent 2 |

| | |
|-----------------------|---|
| ∇p_{static} | Static pressure gradient |
| $p_{0,k}$ | Stagnation pressure at inlet of rotor stage k |
| q_1 | Angle exponent 1 formula exponent |
| q_2 | Angle exponent 2 formula exponent |
| r | Radius |
| Re | Reynolds number |
| Re_p | Particle Reynolds number |
| S_1 | Angle exponent 1 formula constant |
| S_2 | Angle exponent 2 formula constant |
| SFC | Specific Fuel Consumption |
| SPR | Stagnation Pressure Ratio |
| STR | Stagnation Temperature Ratio |
| Δt | Time-step |
| TE | Trailing Edge |
| T_{end} | End time of erosion study |
| $T_{0,k}$ | Stagnation temperature at stage k inlet |
| und | Undamaged rotor 1 stage |
| v^* | Erosion model reference velocity |
| v_p | Particle impact velocity |
| V_p | Volume of particle |
| v_s | Particle slip velocity |
| v_z | Absolute velocity in axial direction |
| v_θ | Absolute velocity in tangential direction |
| $\Delta v_{\theta,k}$ | Flow turning for rotor stage k |
| x | Axial location along the axis of rotation, x-axis |

Greek Symbols

| | |
|-----------------|---------------------------------------|
| α | Absolute flow angle |
| η_{tt} | Adiabatic efficiency |
| θ | Impact angle of particle with surface |
| μ | Dynamic viscosity |
| Ω | Compressor shaft speed |
| ρ | Fluid density |
| ρ_{sample} | Sample wall material density |
| τ | Time scale factor in erosion study |

Subscripts/Superscripts

| | |
|----------|---------------------------------|
| a | Station 2a at outlet of Stage 1 |
| b | Station 2b at outlet of Stage 5 |
| f | Final/off-design condition |
| i | Initial/on-design condition |
| mag | Magnitude |
| mid | Mid-span value |
| rel | Relative frame of reference |
| SC | Centrifugal compressor stage |
| $S1$ | Axial compressor stage 1 |
| $S2 - 5$ | Axial compressor stages 2-5 |
| und | Undamaged rotor 1 stage |
| 2 | Station 2 at compressor inlet |
| 3 | Station 3 at compressor outlet |

Acknowledgments

I want to express my sincere thanks to my advisor, Dr. Robert Kunz, for his constant guidance, support, and remarkable patience over the past 5 years. We have learnt a lot through this long journey, and I am thankful for where we have reached. His mentorship has helped me grow as a researcher, and more importantly, as a person.

I would also like to thank the other members of my thesis committee: Dr. Karen Thole, Dr. John Cimbala, and Dr. Elia Merzari, for their invaluable suggestions and comments. I would also like to thank Dr. Xiang Yang and his former graduate student Dr. Haosen Xu for their insights during our research collaboration.

This dissertation would not have been possible without the constant love, support and encouragement from my family and friends. I am thankful for my parents, Pious and Rani and my sister, Fatima and all my extended family (too many to name). My friends from India who have always answered my calls: Freddy, Ratan, Rohit and Safvan. My family of friends at Penn State (alphabetically): Charles, George, Haley, Kevork, Lauren, Leen, Mario, Mirko, Nick and Samer. This dissertation would not have happened without you. My friends from all over the United States, who encouraged me from far away, Aritra, Mo Nasser and Mo Orabi.

I am thankful for the support and friendship from my former and current colleagues in the CMPL lab, namely, Naman, Leland, Thao and Sam.

I am grateful for the financial support provided through the Office of Naval Research (ONR) Grant Number (N00014-19-1-2232) with Dr. Steven Martens as Technical Monitor. The findings and conclusions in this dissertation do not necessarily reflect the view of the funding agency. I am also grateful to the Department of Mechanical Engineering at the Pennsylvania State University for providing the opportunities and the computational resources. I would also like to thank the folks at NAVAIR for their valuable input during the course of this research. I would also like to acknowledge the Department of Defense High Performance Computing cluster for enabling this research.

Dedication

Familiam meam, sanguinis et electionis

Chapter 1 |

Introduction

1.1 Overview

Gas turbines find application in propulsion (aerial, terrestrial and marine) and power generation. The performance of gas turbines is integral to several factors taken into account by operators, such as efficiency, fuel costs, maintenance costs, etc. In this scenario, predictions of gas turbine performance are essential in making design, production and operational decisions. The axial compressor is the first major section of a gas turbine engine [1], [2], [3]. The role of the axial compressor is to compress incoming air to an optimal stagnation pressure such that the fuel combustion in the combustor takes place at the highest possible efficiency. The increase in gas turbine efficiency is dependent on two primary parameters: increase in pressure ratio and increase in firing temperature [4]. Hence, its performance is integral to the performance of the whole machine. In many environments, especially in propulsion, large amounts of particles like sand, dust and ash can be ingested into the axial compressor, which leads to damage that can significantly reduce the performance of the compressor. In this chapter, we review some of the previous

efforts made for prediction of axial compressor performance as well as discuss some of the damages that it encounters due to particle ingestion.

1.2 Literature Review

Damage to gas turbines due to particle ingestion is a very critical area of research, relevant to both gas turbine manufacturers and operators around the world. Particularly, as air traffic increases in developing countries, this area of research has gained increased importance due to the high concentration of particulate matter in their environments. Another factor is the continued presence of major militaries in the Middle East and Asia, where the concentration of airborne particulate matter is high as shown in Figure 1.1, which renders research into particle ingestion damage of gas turbines operated by them, even more critical in terms of standby military readiness. In general, industrial gas turbines are installed with inlet filters that stop the passage of particles [5]. Unlike land-based gas turbines, filters cannot be used for most aero-engines except in the case of military helicopters.

In certain environments, solid particles such as sand, dust, ice and volcanic ash can be ingested by a gas turbine engine in significant quantities. The higher inertia of some of these particles can cause them to deviate from the gas path streamlines and impact the fore-stages of axial fans and compressors [7]. Neilson and Gilchrist [8] determined that for an accelerating gas-particle mixture, particle size, shape and density, initial particle velocity, the concentration of particles and the length of the experimental domain are all important variables affecting final particle velocity, which in turn impacts the erosion rate. The damage to the

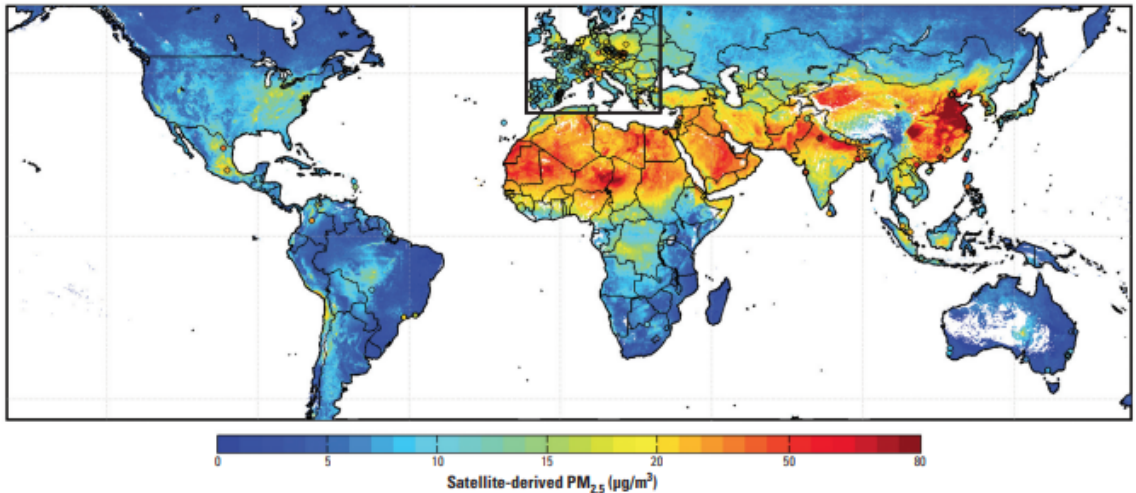


Figure 1.1. Concentration of airborne particles smaller than $2.5\mu\text{m}$ [6]

blades is caused by direct impingement of large particles as well as the impact and deposition of finer particles due to secondary flows through the blade passage.

In the case of aeroengines, particle ingestion into the core occurs during all phases of flight operation, however, it is most critical during takeoff and landing where particle/dust densities are typically higher. Figure 1.2 shows sand being ingested into the engines of a C-17 during takeoff [9].

Some studies have been performed to estimate the amount of sand being ingested by land-based gas turbines. According to Zaba and Lombardi [10], a power gas turbine in residential areas can ingest up to 1.5kg of solid contaminants per day despite the installation of filtration systems. Osborne [11] reported that particle ingestion in high quantities over long periods of time led to reduction in engine life.

Aust and Pons [12] created a taxonomy of various gas turbine defects and their associated causes. Damage modes associated with particle impact with compressor blades and endwalls include pitting, material loss and curling of blade leading and trailing edges, increased effective tip clearances and erosive blade surface



Figure 1.2. A view of sand being ingested into a C-17 at take-off [9]

roughness. The aerodynamic performance of the compressor blades is affected by these geometry changes. This, in turn, affects the efficiency and operating range of the compressor.

A number of research groups have studied these various damage modes in axial compressors. Balan and Tabakoff [13] studied the effect of sand erosion on axial compressor cascade aerodynamics and performance deterioration. They observed particularly severe erosion at the rotor leading edge and on the pressure surface. They concluded that the decreases in performance could be attributed to the changes in the blade leading and trailing edge geometries, increased tip leakages, surface roughness and altered pressure distribution. They also performed trajectory calculations of particles within the compressor cascade and found good agreement with experimental results.

Tabakoff et al. [14] simulated and investigated the effects of erosion in cascades,

single-stage and multi-stage compressors. They illustrated that the stage stacking technique might be useful to systematically study the effect of individual stage erosion in multi-stage compressor performance. Their theoretical prediction of performance deterioration using an erosion fault model based on chord length reduction compared well with both cascade and single-stage compressor experimental results. Particle rebound characteristics, in terms of coefficients of restitution for turbomachinery applications, were also modeled as part of this study.

Sallee [15] reported significant in-service damage to various components, including the high pressure compressor (HPC) for the JT9D engine. They also reported an assessment of the effect of compressor operation time on rotor blade damage. Figure 1.3 shows erosion of the JTD9 HPC rotor blade after several thousand hours of operation.

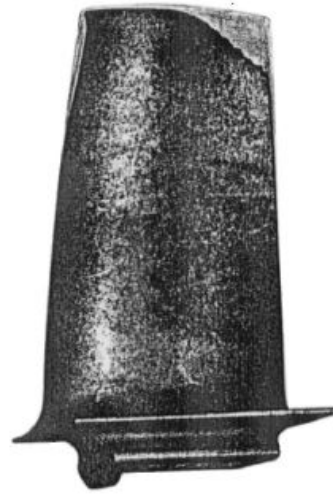
Ghenaiet et al. [16] assessed the damage to an axial fan due to sand ingestion through a qualitative study of erosion patterns and quantitative measurements of degradation in aerodynamic characteristics. Their tests indicated that there is significant leading edge erosion extending towards the tip corner of the blade pressure side. On blade suction side, the erosion was observed to be concentrated on the leading edge and mostly absent on the remaining areas. This has been attributed to the high velocity and incidence angle of particles upstream of the rotor leading edge. They also observed significant erosion of the rotor tip due to migration of particles across the tip clearance region from the pressure side to the suction side. Erosion of the IGV blades was observed on the tip corner pressure side close to and around the leading edge. Figure 1.4 shows a rotor blade from their experiments illustrating the damage to the pressure side and tip region.



JT9D 9th Stage HPC Rotor Comparison



8000 Hrs
2000 Cycles



8700 Hrs
5500 Cycles

7-10

PS107-10
770710

Figure 1.3. Eroded blades of the HPC rotor of the JT9D after different stages of operation [15]

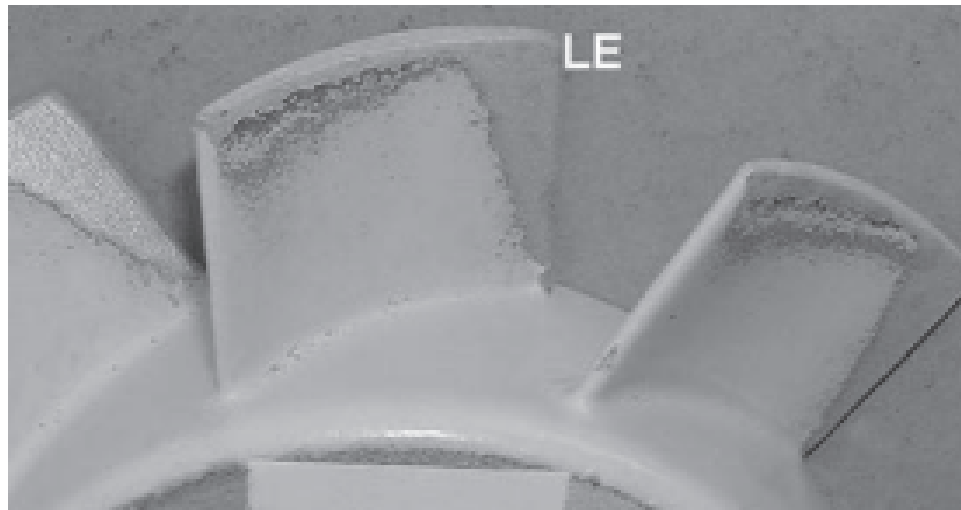


Figure 1.4. Erosion of the rotor pressure side and tip region by sand ingestion [16]

Batcho et al. [17] [18] performed experiments on the Pratt and Whitney TF33

turbofan and J57 turbojet engines to assess particle ingestion damage on the performance of the respective axial compressors. They observed that solid particle erosion led to increased tip clearance and diminished blade leading edge, as shown in Figure 1.5, which in turn, led to the performance deterioration of both the Low Pressure Compressor (LPC) and the High Pressure Compressor (HPC). They also determined that the deteriorated engine was more susceptible to surge at low power settings. The performance deterioration was predicted based on semi-empirical stage stacking models. Based on their analysis, they also recommended mitigation strategies in terms of intercompressor bleed and anti-ice air to reduce the likelihood of surge as a result of erosion damage.

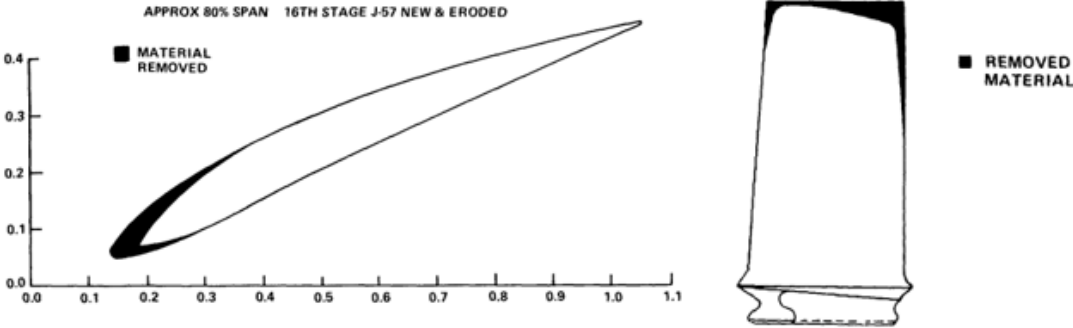


Figure 1.5. Profile erosion of 16th stage rotor blade at 80% span (left), erosion of tip region of 13th stage rotor blade (right) [17] [18]

Several groups have studied compressor damage using CFD. Li and Sayma [19] assessed the effect of tip curl damage on the stall margin of a transonic axial compressor. They observed that the presence of one damaged blade prevented the stall cells from growing and improved stability by acting as a buffer preventing stall cells from neighboring passages from growing and merging together by altering the separation pattern. This was in contrast to the undamaged case, where the

rotating stall formed a large stall cell and led to the abrupt ending of the simulation indicating surge.

Fedechkin et al. [20] modeled different "nicks" and bending of the first stage rotor blade leading edge in a 4-stage axial compressor as shown in Figure 1.6. Their methodology was validated with experimental results using the undamaged case. Their initial study showed that there was insignificant impact on the fan performance. Hence, they performed an analysis to determine the critical values of the nicks and bending, for which a significant deterioration in axial fan performance could be observed. They determined limits for each of these damage modes (nicks and bends) for observable performance degradation at multiple operating conditions.

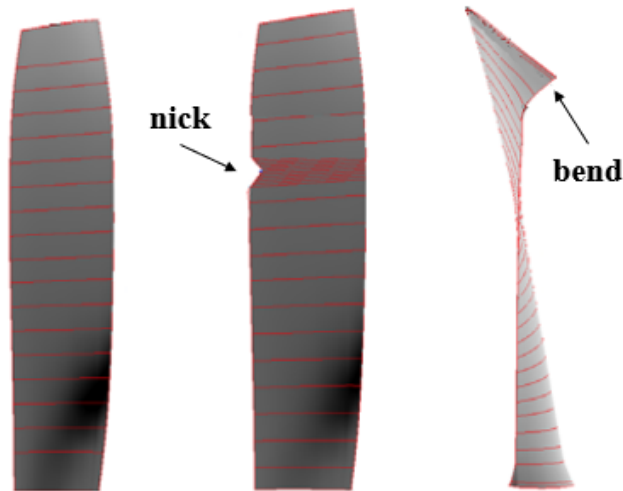


Figure 1.6. Undamaged blade (left), blade with nick (middle), blade with bend (right) [20]

Suzuki and Yamamoto [21] performed two-phase CFD analysis of a single stage axial compressor. The particle trajectories and impaction were used to model erosion depth explicitly in a subsequent CFD analysis. They reported localized damage patterns and performance deterioration consistent with experimental results.

They observed that the major particle impaction took place at the leading edge, pressure side and the tip region of the rotor blade as shown in Figure 1.7. It was observed that when particle-wall collisions occurred and reduced the momentum of the particles, they became susceptible to the centrifugal forces and moved toward the tip clearance region leading to the erosion of the rotor tip as well as the shroud. They determined that, in general, particle erosion damage had the following tendencies: the leading edge damage was larger than that of the trailing edge, tip region damage was larger than that of the hub region and the pressure side damage was larger than that of the suction side damage. They also observed that the blade surfaces as well as the end walls became rougher leading to stagnation pressure loss as the friction drag of the boundary layer increased.

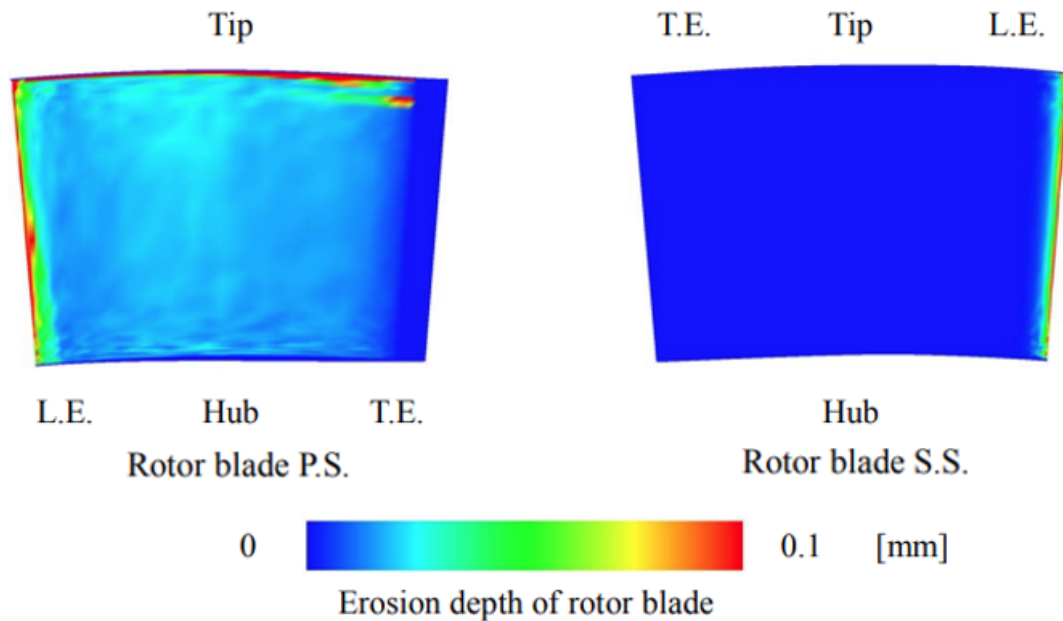


Figure 1.7. Erosion patterns of the rotor blade, pressure side (left), suction side (right) [21]

The research above focuses on ballistically impaired geometry. Other researchers

have focused their studies on less severe damage modes including increased surface roughness and fouling/deposition. Suder et al. [22] performed laser anemometry experiments and some attendant CFD analyses on roughened and thickened compressor blading and observed significant performance degradation ($> 5\%$ reduction in stagnation pressure ratio and adiabatic efficiency) for the well-studied NASA Rotor 37. The negative impact of roughness on the stagnation pressure ratio is shown in Figure 1.8. Most of these losses were attributed to roughening/thickening of the leading edge and suction side and transition effects. They observed that the blades should be maintained as smooth as possible during the manufacturing process as well as during its operation. Their measurements indicate that the sensitivity of Rotor 37 to thickness/roughness is primarily due to blockage changes in the rear of the blade passage as it has a tight throat area margin and high exit Mach number.

Morini et al. [23] performed CFD simulations of NASA Stage 37 to assess the effect of compressor fouling by imposing different combinations of added thickness and surface roughness to the baseline geometry. They observed that the geometric modifications led to decreased mass flow rate and stagnation pressure ratio. Efficiency loss was a result of the blockage in the rotor blade passage. They also noted that the stage stacking performance assessment procedure needs to be revised as it is currently unable to capture some of the trends in the analysis. Their computational results were in the same order of magnitude as the experimental results. This indicated that their study required further analysis to significantly increase prediction accuracy.

Gbadebo et al. [24] performed experimental and CFD studies on an artificially

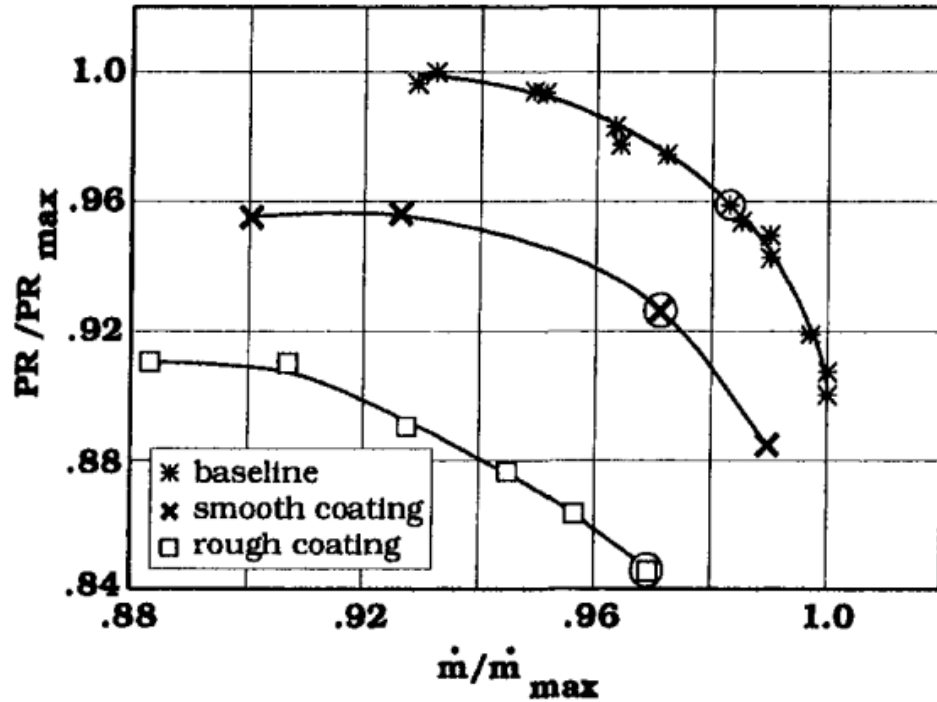


Figure 1.8. Stagnation pressure ratio vs mass flow characteristics at 70 percent span for the different roughness configurations in the study [22]

roughened low speed compressor stator. Their findings concluded that surface roughness, typical of that which is likely to form during engine operating lifetime, led to a significant reduction in performance (in terms of stage stagnation pressure) over a wide range of flow due to its effect on 3D separation. Large corner hub separation of the stator blades led to high losses, increased blockage and deviation. As a result of blockage, significant radial movement of flow was observed, which in turn led to redistribution of loading and change of effective incidence at different spans.

Syverud and Bakken [25] performed a computational study of the impact of surface roughness on axial compressor performance deterioration. Particularly, they focused on the impact of surface morphology modifications due to salt deposits

on the performance of the axial compressor of the GE J85-I3 jet engine. They incorporated the effects of surface roughness by modeling the frictional losses, blockage and deviation. They observed a significant reduction in the flow coefficient, which is specifically impacted by the 3D separation affected by the surface roughness. This resulted in significant deterioration of compressor performance. Syverud et al. [26] also performed an experimental study on the impact of accelerated salt water ingestion into the GE J85-I3 and observed significant deterioration on stage performance. They observed that the deposited matter in the engine depended on the nature of the deposits i.e., the material, the particle size, and the adhesive capability of the material. Their study revealed that the salt deposits were mainly found in the front stages of the compressor, and the stator blades were found to have more deposits than the rotor blades. Figure 1.9 shows the studied blades with salt deposition.

Walton et al. [27] also quantified the significant leading edge surface roughness of ex-service compressor blades. Their research focused on the metrology of the roughness rather than its performance impact. They concluded that as a result of increased blade surface roughness of the leading edge, this surface region no longer had a circular edge and needed to be considered a distinct blade region in analysis. This was attributed to the modifications in flow features along the leading edge due to the change in surface geometry. Their study showed that the maximum surface roughness was found at the leading edge and recommended this region to be a target for further coating protections.

Meher-Homji et al. [28] provided a comprehensive overview of compressor fouling and washing for gas turbine engines. The causes, effects and control of axial

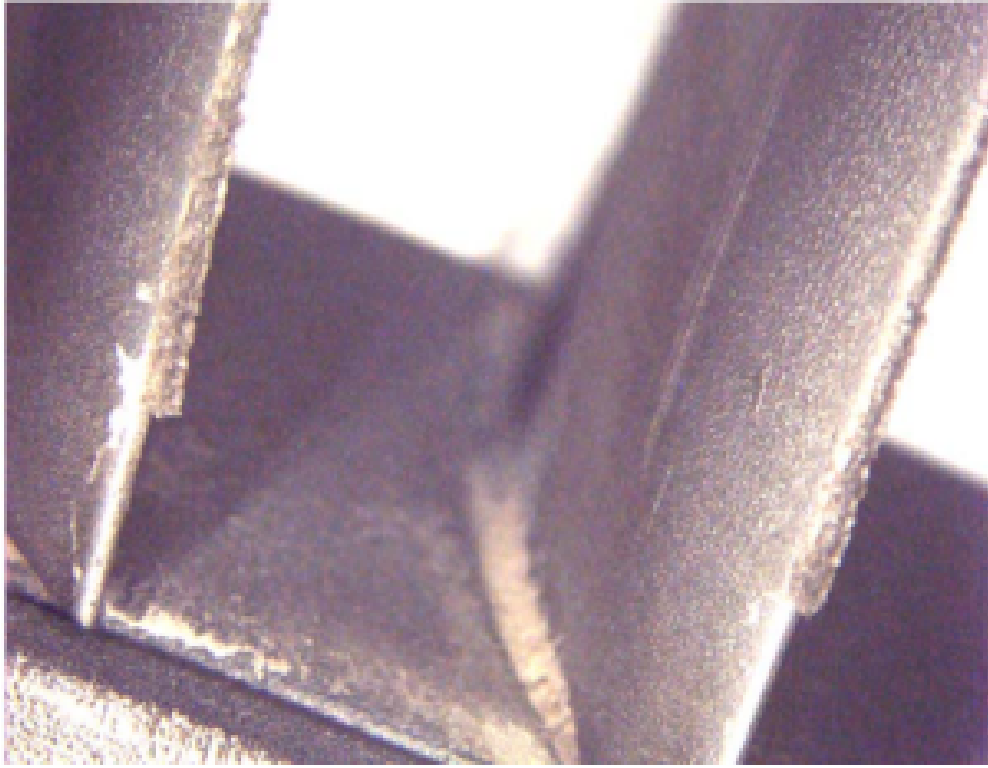


Figure 1.9. Salt deposits at the leading edge of the second-stage stator vanes [26]

compressor fouling are discussed in detail. Two major issues associated with fouling were studied, namely, the susceptibility of an engine to compressor fouling and the sensitivity of the engine to a certain degree of imposed fouling. Understanding compressor fouling leads to benefits related to selection of filtration systems, engine performance monitoring and operation and important maintenance practices such as compressor washing. Further discussion on the mitigation strategies was conducted in this study. Figure 1.10 shows different examples of fouling in gas turbines.

Kruz and Brun [29] observed that compressor fouling was primarily caused by adhesion of particles of size 0.01mm and below. They also observed that high humidity in the ambient conditions led to increased wetness, which in turn led to increased fouling. Nel [30] performed numerical modeling of effect of fillets and

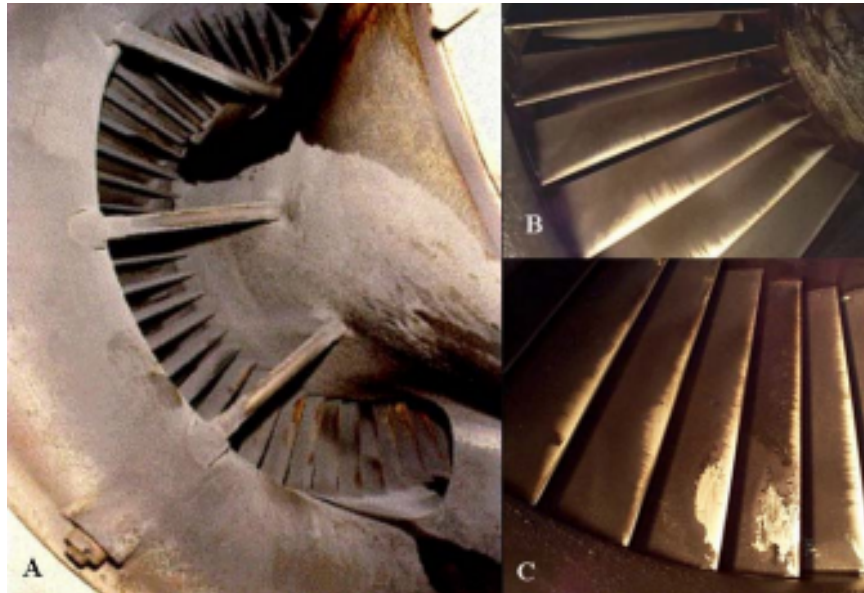


Figure 1.10. Examples of fouled compressor blades: (a) Heavily-fouled air inlet bell-mouth and blading on a 35 MW gas turbine; (b) Oily deposits on blading; (c) Compressor blades fouled with a mixture of salts and oil [28]

surface roughness on the performance of the transonic axial compressors namely, the Darmstadt R-1/S-1 and NASA Stage 37 using the mixing plane approach.

Particle damage is a very complex process and extensive research has been performed to attempt to understand the behaviour of materials and particles during erosion as well as deposition. Wilson et al. [31] studied the importance of shape in particle rebound behavior. Specifically, they focused on incorporating cubical particles in their simulations for characterizing particle rebound behavior. The use of cubical particles enables increased consideration of angularity, mass distribution and geometric complexity of particles compared to spherical particles used in most models. They identified additional factors related to particle shape that affect particle rotation and total rebound energy, which in turn affects the rebound characteristics and erosion mechanisms.

Pepi et al. [32] performed sand-air erosion testing for different helicopter rotor blade materials at the University of Dayton Research Institute (UDRI) Particle Erosion Testing facility. Different types of sand mixtures were used, and comprehensive post-test analysis included: visual examination, mass loss calculations, erosion rate determination, surface roughness testing, volume loss calculations, scanning electron microscopy characterization, and metallography. Figure 1.11 shows magnified images of damaged sample surface features due to sand impaction. Based on the results of these tests, a new test standard (MIL-STD-3033) was developed to evaluate materials that could potentially be used on the leading edge of helicopter rotor blades.

Oliani et al. [33] devised a methodology to increase the accuracy of particle tracking through general grid interfaces and mixing planes in multi-stage turbomachinery applications. A mass conservative particle redistribution technique was devised which would be requested at the interfaces between multiple stages as part of this augmented methodology. They tested their methodology against three different turbomachinery applications, focusing on erosion in an axial compressor, trajectory analysis in a centrifugal fan, and impact analysis in an axial turbine. The numerical results showed considerable agreement with results reported in literature.

Brandes et al. [34] proposed an approach to incorporate high-level computational and experimental results into an effective non-dimensional model for the severity estimation of flight missions due to compressor erosion. The severity of erosion was measured in terms of the shortening of the camber line at the blade leading edge. Their findings included the effect of bypass ratio, bleed setting, and degree of particle separation on the severity of erosion.

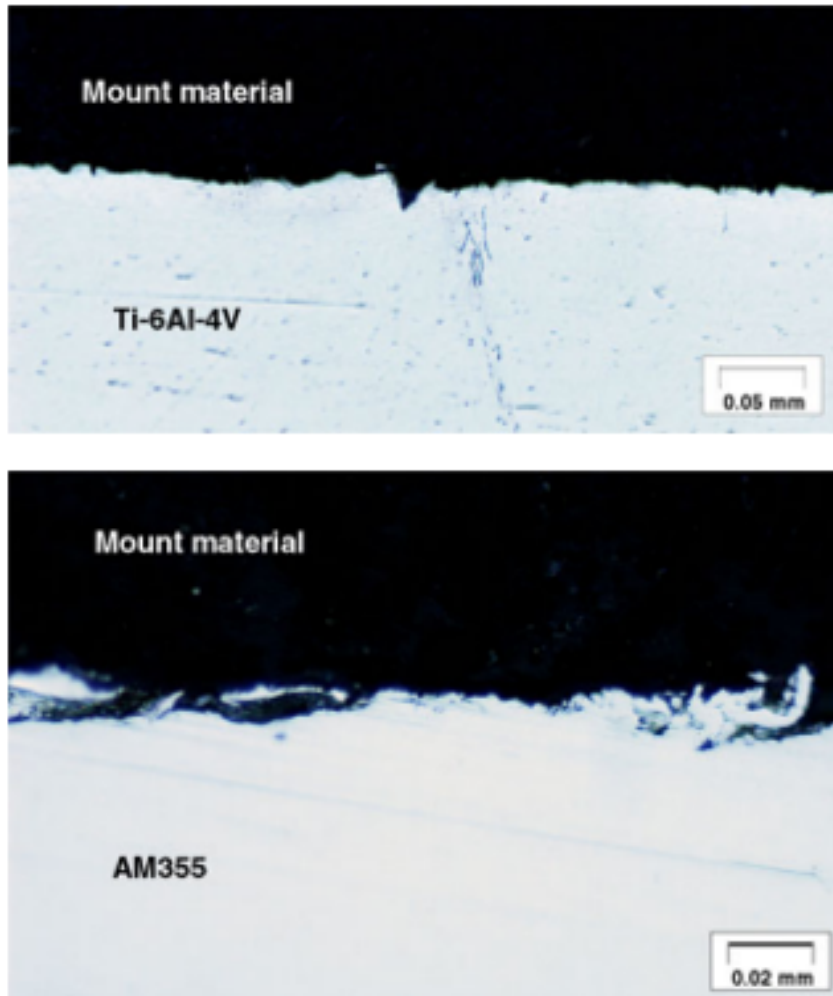


Figure 1.11. Magnified images of sample surfaces post sand impact study: cut features on the sample surface (top), platelet features on sample surface (bottom) [32]

Vulpio et al. [35] described a quantitative approach to predict particle deposition on the vanes of an axial compressor starting from the flow field obtained employing computational fluid dynamic (CFD) simulations. Figure 1.12 shows fouling damage of the IGV blade. The results were compared to experiments performed on the Allison 250 C18 compressor unit subject to particle ingestion under controlled conditions and showed good agreement in the estimation of the predicted values of the deposited mass and the corresponding patterns through the compressor stages

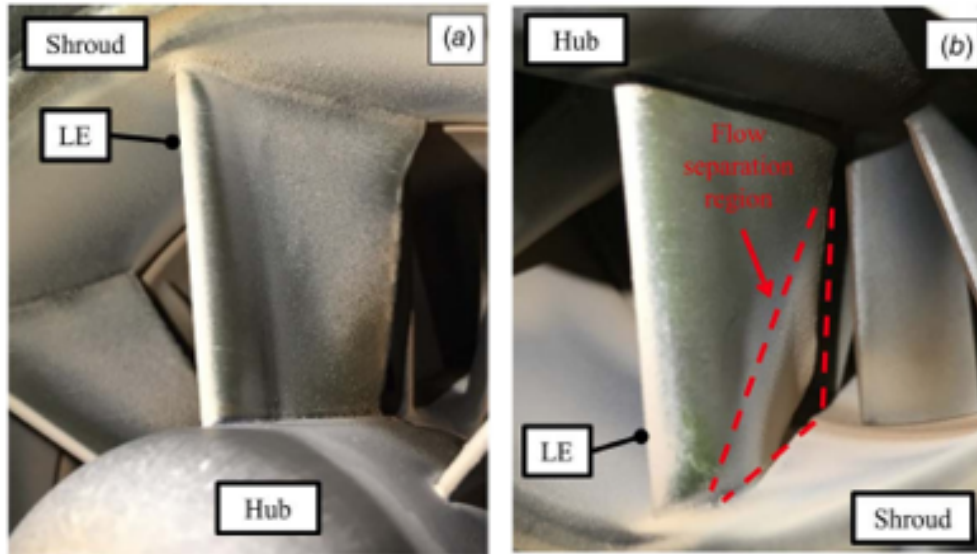


Figure 1.12. Fouling of the IGV blade: (a) Pressure side (b) Suction side [35]

and recommended possible applications of this approach to compressor design and maintenance.

Doring et al. [36] presented an experimental setup to create reproducible deposition patterns in aircraft engine compressor blade rows as well as to quantify both magnitude and timescale of the resulting performance deterioration. The methodology presented, composed of the experimental data and the model, provided the basis for predicting deposition effects on compressor and engine overall performance. Their results added credence to the fact that 95% of performance deterioration due to deposition occurs within the first 1000 flight cycles.

Saxena et al. [37] described a 3D CFD methodology for tracking particles along a multistage axial compressor and presented the particle ingestion analysis for a HPC section. ANSYS CFX was used to perform the simulations and the particle trajectories and radial particulate profiles are compared for particles of different diameters. Larger diameter particles were observed to centrifuge radially

out towards the compressor casing more significantly than smaller particles. They also examined the extraction of particles by the bleed flows at different extraction points as well as the effect of particle shape.

Bons et al. [38] developed a simple physics-based model that predicts particle rebound and deposition for particles ingested in gas-turbine which included the essential physics of the particle-wall interaction including elastic deformation, plastic deformation, adhesion, and shear removal. Particles were modeled as simple cylinders under compression. The simple algebraic formulation can be easily adopted into any CFD code. The model could be tuned to various factors. Five validation cases were performed with moderate successes at varying degrees.

Suman et al. [39] [40] used NASA Rotor 37 as a case study for the numerical investigation of small particle deposition effects on transonic axial compressor blading. Their results focused primarily on particle impact zones and the effect of particle size distribution on fouling behavior. They also focused on particle-blade interactions in terms of impact velocity and impact angle.

Yang and Boulanger [41] performed an unsteady analysis of a full annulus axial fan and verified the validity and need for unsteady CFD models compared to steady models for turbomachinery applications. They presented qualitative results in terms of erosion patterns and particle trajectories. Figure 1.13 shows a comparison of the erosion patterns between the experimental and CFD results.

Ghenaiet [42] performed a study of particle trajectories and erosion patterns for the IGV and first compression stage of the PW-JT8-D17 engine. Erosion was mainly observed at the leading edge and end-walls of the IGV. In the case of the first stage rotor, the erosion was mostly observed on the pressure side as well as

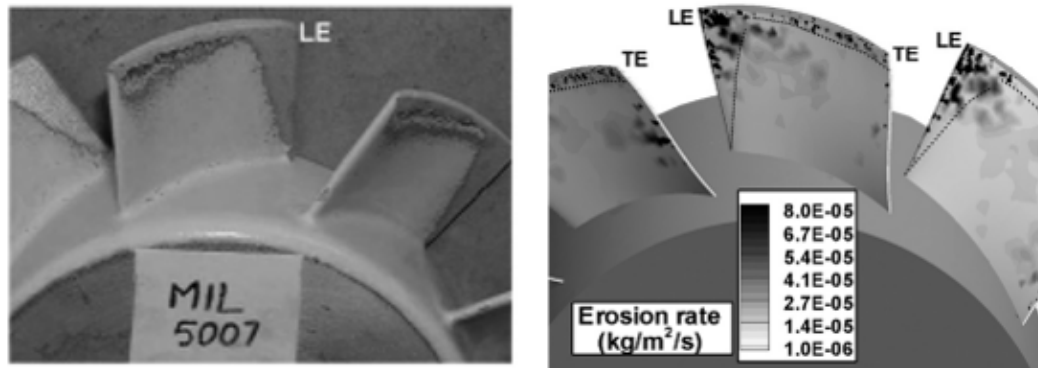


Figure 1.13. Comparison of erosion patterns: Experimental (left), CFD (right) [41]

the leading and trailing edges and tip region as shown in Figure 1.14. For the first stage stator, the erosion was spread over the blade surfaces in addition to the leading and trailing edges.

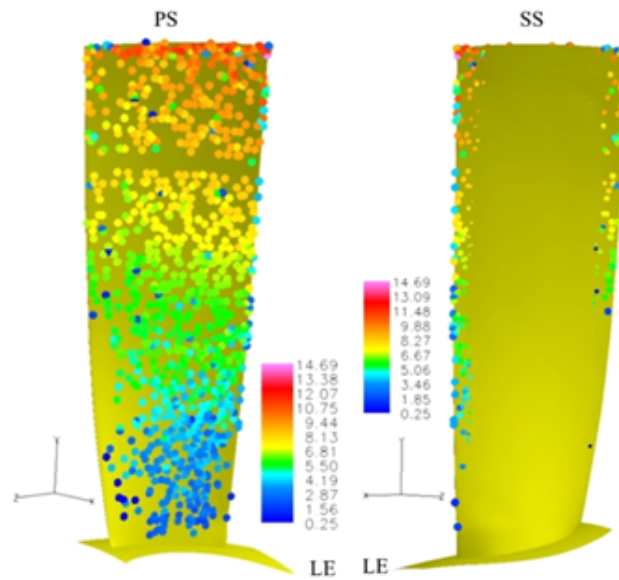


Figure 1.14. Erosion patterns of the first stage rotor [42]

Ghenaiet [43] explored the effects of particle erosion on centrifugal compressor blading and studied it in terms of eroded mass and erosion patterns. Most of the particle impacts were on the pressure side. Regions of high erosion were also

observed on the leading edge of the blades and the inducer top corner and along the blade tip.

Outside the sphere of turbomachinery, particle impact, and hence erosion, is a relevant topic in several other industries which has yielded advanced research. Particularly, the oil and gas industry is very much involved in erosion research [44]. Extracting oil and gas from the ground results in the erosion of drilling pipes and can result in maintenance and repair issues and hence warrants the need for erosion modeling and research [45]. Some of the following research has been motivated by their partners in the oil and gas industry.

Ediriweera [46] studied impact erosion by solid particles in gas-particle flows through experimental research and performed studies to understand the effects of several parameters such as impact angle and particle size distributions. Results were presented in terms of erosion rate and surface profiles.

Swaminathan et al. [47] provided an overview of prior elevated temperature solid particle erosion (SPE) testing capabilities of participating organizations and the status of development of a new international test standard. A round robin inter-laboratory test program was recommended to develop an elevated temperature SPE standard that would provide more appropriate reference conditions for SPE conditions encountered in current and next generation steam turbine applications.

Nguyen et al. [48] constructed a new erosion testing rig for sand-air erosion with incident velocities up to Mach 3. They performed a study on a SUS304 steel sample in terms of the impact angle and testing time. They obtained results in terms of erosion rate, surface profile evolution and surface micro-structure characteristics. For the sample tested and a given incidence velocity, maximum erosion was observed

at an incidence angle of 40° .

Mansouri [49] performed erosion testing using sand-air and sand-water jets on various samples to assess the impact of particle velocity, particle incidence angles and existing erosion models on erosion characteristics. In addition, Mansouri formulated an erosion model which showed good agreement for the parameter space chosen for this study.

Lopez et al. [50] developed an algorithm to predict erosion due to impingement of a jet of water containing sand particles on a stainless steel in OpenFOAM. The methodology involved the computation of the time-averaged erosion field and coupling it with a three dimensional mesh deformation algorithm to compute the surface geometry of the eroded surface over time. The methodology took into consideration the multiple time scales involved in this study as the physical processes (with significant impact) involved in the erosion phenomenon occur at time scales orders of magnitude higher than those of the flow field. Their methodology employed a scaling factor to match the experimental results of the water jet impingement test by Nguyen et al. [51] and was not explained in terms of any physical processes involved in erosion.

Agrawal et al. [52] also developed an algorithm to include the effect of dynamically changing pipe geometry in CFD based erosion modeling in ANSYS Fluent. They considered the case of sand erosion inside a slurry pipeline. The erosion rate was calculated using a combined Eulerian-Lagrangian framework and the solid wall geometry is deformed by coupling the computed time-averaged erosion field with the Moving-Deforming-Mesh (MDM) functionality available in Fluent. They also recommended several guidelines with respect to the erosion and turbulence

models to be used for similar studies. Their study on pipe erosion concluded that the erosion is maximum at the corner of the pipe and in regions of regions of re-circulation, where particle-boundary interactions are maximum. Figure 1.15 shows the evolution of the pipe geometry as a result of the erosion coupled mesh deformation over a time period of 40 hours. An experimental quantitative verification of the results was lacking in this study.

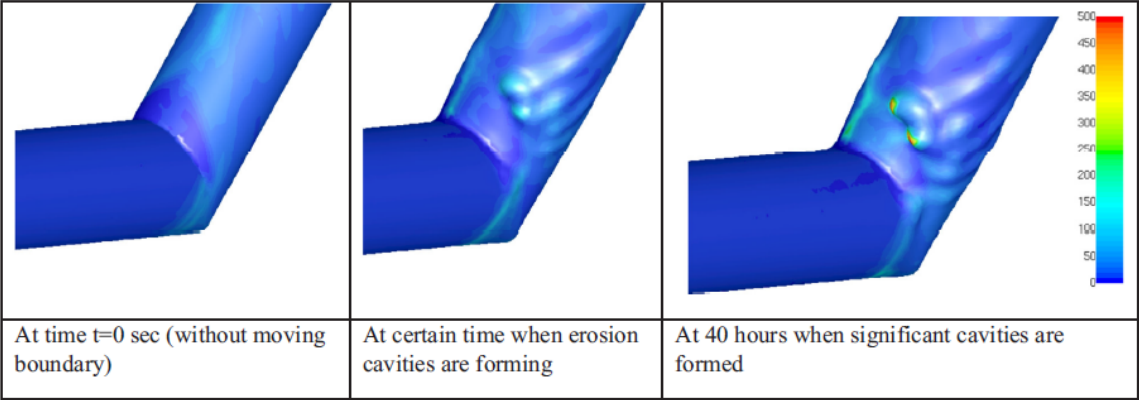


Figure 1.15. Time evolution of deformed pipe geometry due to erosion [52]

Duarte and de Souza [53] expanded on previous works using the erosion coupled mesh deformation algorithm to perform CFD studies to predict the evolution of geometry change due to erosion. Specifically, they studied three cases: erosion of a standard 90° elbow, erosion due to jet impingement and erosion in a bean choke. The results showed that a qualitative estimation of the erosion pattern and impact locations was very accurate. The quantitative estimates of the surface profiles and deformed geometries were in reasonable agreement with experimental results within the same order of magnitude.

1.3 Outline of Dissertation

This dissertation is organized as follows:

In Chapter 2, the technical approaches associated with geometry generation, CFD meshing and CFD modeling are discussed. The simulation setup and target conditions that conform to damaged compressor operation protocols are presented. The results of a validation study for the code, modeling and meshing strategies using NASA Rotor 37 are briefly included.

In Chapter 3, the results for the steady-state calculations for the three damaged and one undamaged configurations, solved in the rotating frame of reference, are presented in terms of compressible wave field and secondary/tip flows, spanwise performance parameter distributions and efficiency. A method to estimate the effect of rotor damage on engine SFC is devised and presented. The different configurations are rank ordered based on their impact on engine performance.

In Chapter 4, the results of a full stage unsteady analyses are presented. These are performed in order to go a step beyond the inherent averaging of local aerodynamic variables encountered in steady analyses. These results are also presented in terms of compressible wave field and secondary/tip flows, spanwise performance parameter distributions, efficiency, and impact on SFC. The results of a comparison study between the steady-state half stage simulations and the unsteady full stage simulations are also discussed and the need for transient analyses is justified.

In Chapter 5, an improved version of a combined Eulerian-Lagrangian method to study the effect of erosion is presented. A method validation using a well-documented data set is performed and the ensuing results and conclusions are

presented. The qualitative results of an erosion study of NASA Rotor 37 blade surface due to sand ingestion are presented. In addition, an illustrative study of erosion coupled surface deformation of a mid-section of Rotor 37 spanning from 40% to 60% is performed and discussed.

In Chapter 6, a summary of the research conducted to date, major research contributions and directions for future research work are discussed.

Chapter 2 |

Technical Approach

This chapter presents a discussion of the technical approach employed in the CFD studies performed for the method validation study using Rotor 37 and the CFD studies of the T700 axial compressor first stage in Chapters 3 and 4.

2.1 Methodology

2.1.1 Geometry

The geometry considered belongs to the compressor of the General Electric GE T700-401C [54] as shown in Figure 2.1. Different variants of the T700 are found in military helicopters like the Apache, Black Hawk, Viper, Venom etc. They are also found in several civilian helicopters as a variant called the CT7. The T700 is one of the most widely manufactured gas-turbine and in-service engines in the world for helicopter propulsion [55]. The compressor of the T700 consists of 5 axial stages and 1 centrifugal stage. The first stage rotor of the T700 is transonic and is the main focus of this study. The geometry files for the rotor and stator blades

as well as the endwalls were obtained from GE and Naval Air Systems Command (NAVAIR). NAVAIR is pursuing a highly instrumented test for the T700, and the results are expected in Fall 2023. Figure 2.2 shows several views of the stage 1 rotor blade geometry.

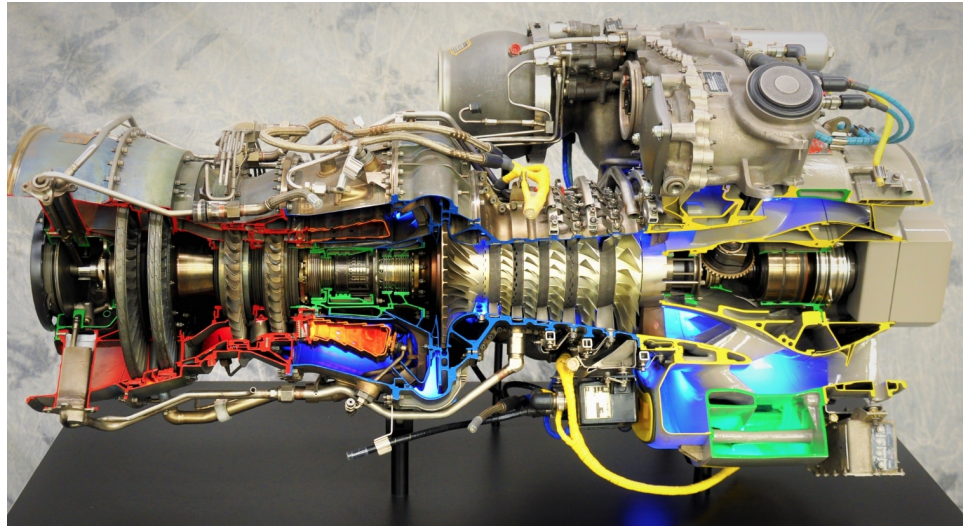


Figure 2.1. A sectional view of the T700 engine [56]

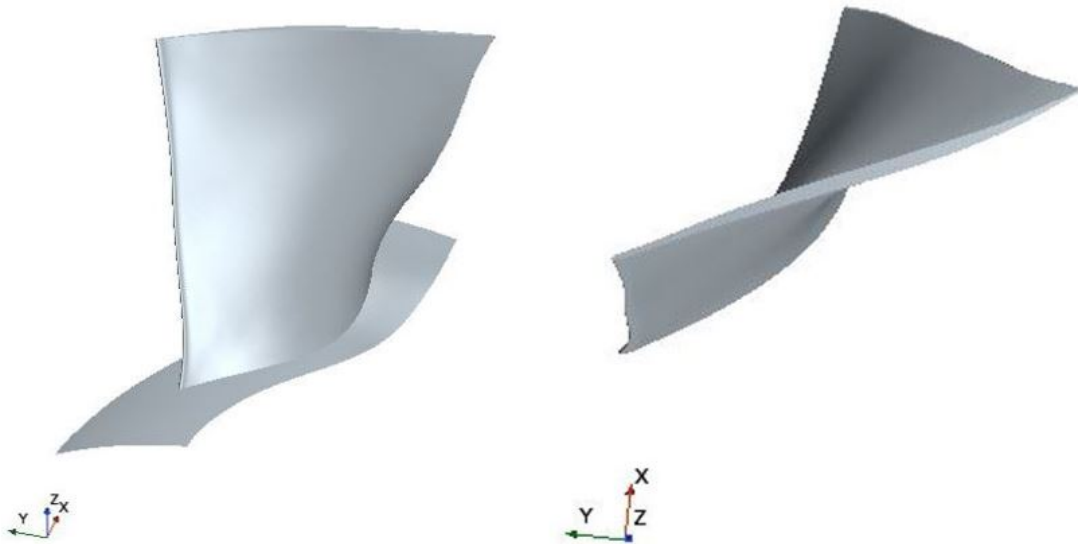


Figure 2.2. Two views of the T700 first stage rotor blade

2.1.2 Damaged Blades

Since the damaged blades from the T700 experimental tests at NAVAIR are forthcoming, an additive manufacturing (AM) based approach was used to represent damage for the CFD studies. The undamaged blades were first fabricated with a Creality3D Ender-3 V2 3D printer (shown in Figure 2.3) using Polylactic Acid (PLA) plastic which is easily amenable to local mechanical and thermal deformation without compromising the shape and aerodynamic design of the blade.



Figure 2.3. Creality 3D Ender-3 V2 3D printer

The plastic blades were then manually damaged using thermal and mechanical treatments to produce several damage configurations which will be described below. The damaged plastic blades were then 3D optically scanned to produce point clouds. The point clouds were then processed in SolidWorks [57] to produce 3D CAD models ready to be used for simulations. Figure 2.4 shows the blade geometry before and

after the clean-up resulting in a watertight CAD ready to be incorporated into a CFD simulation. Extraneous features resulting from the optical scanning process were successfully removed. The surface was smoothed using the default smoothing algorithm within SolidWorks [57].

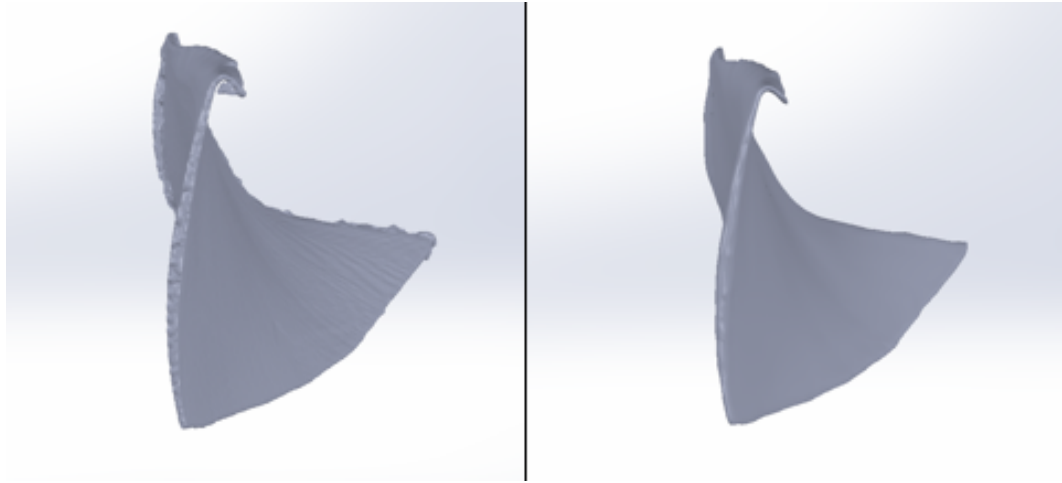


Figure 2.4. Scanned geometry before cleanup (left), CFD ready geometry (right)

The damage modes under consideration have been observed by many workers including Walton et al. [27], Aust and Pons [12] and Zuniga and Osvaldo [58]. Cragged and eroded damages arise from the surface abrasion/wear of the blades over long exposure times. Curled tip damage arises due to impact from singular foreign large scale object ingestion. These and other damage modes were explored by Aust and Pons [12] and the definitions, descriptions and photography in that reference were used to adapt geometries studied herein.

Figure 2.5 shows a compressor blade with representative cragged leading edge damage, and the corresponding 3D printed blade used in this study. The blade leading edge has notches of depth 1mm each at 20%, 35%, 46%, 65% and 84% spans. The notches were made and then mechanically smoothed.



Figure 2.5. Original [12] and 3D printed blades with Cragged damage

Figure 2.6 shows a blade with leading and trailing edge chord material loss, and the corresponding 3D printed blade. At the leading edge, there is blade material loss from 75% span to 25% chord length at 100% span. At the trailing edge, there is blade material loss from 70% span to 30% chord length at 100% span.

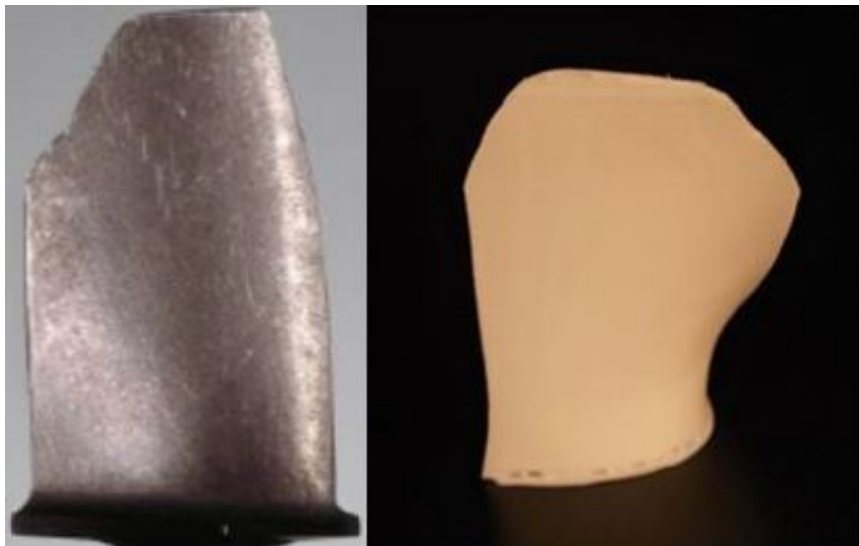


Figure 2.6. Original [12] and 3D printed blades with the Eroded damage

Figure 2.7 shows a blade with a curled tip, and the corresponding 3D printed blade. The blade tip is bent 45° towards the suction side along a line connecting

the leading edge at 75% span to 10% percent chord at the tip.

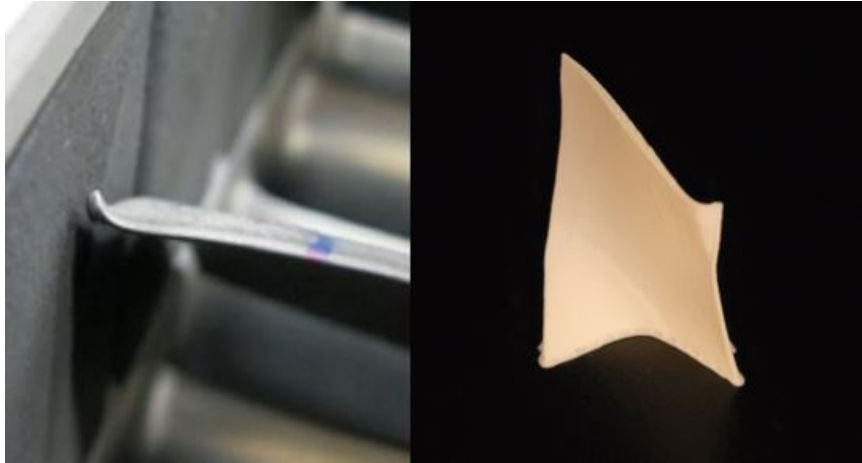


Figure 2.7. Original [12] and 3D printed blades with the Curled damage

2.1.3 Meshing Strategy

The automated mesher in STAR-CCM+ (v2021.1) [59] was used to create a sub-layer resolved unstructured polyhedral mesh with prism layers at the blade surfaces and end-walls. The automated mesher in STAR-CCM+ [59] has been proven to be a great tool for creating meshes for complex geometries seen in turbomachinery. The following meshing options were used:

1. **Polyhedral mesher:** generates a volume mesh that is composed of polyhedral-shaped cells. It is numerically more stable, less diffusive, and more accurate than an equivalent tetrahedral mesh. Moreover, it also contains approximately five times fewer cells than a tetrahedral mesh for a given starting surface.
2. **Advancing layer mesher:** creates a volume mesh composed of prismatic cell layers next to wall boundaries and a polyhedral mesh elsewhere. The mesher

creates a surface mesh on the wall and projects it to create the prismatic cell layers. The prismatic cell layers help capture the boundary layer, turbulence effects, and heat transfer near wall boundaries.

- 3. **Surface remesher:** remeshes the initial surface to provide a quality discretized mesh that is suitable for CFD. It is used to re-triangulate the surface based on a target edge length supplied and can also omit specific surfaces or boundaries preserving the original triangulation from the imported geometry.

A structured grid built in Pointwise [60] was used to extend the outlet domain. This was done to reduce the overall mesh count and to facilitate accurate spanwise averages at the stage exit. The grid had a y^+ of 1. The end walls and the tip clearance gap were explicitly resolved using 31 prism layers and had a growth rate of 1.19 for a smooth transition to the bulk mesh. Similar meshing strategies were used for the T700 as well as NASA Rotor 37. Views of the mesh used for the Rotor 37 validation study are shown in Figures 2.8 and 2.9.

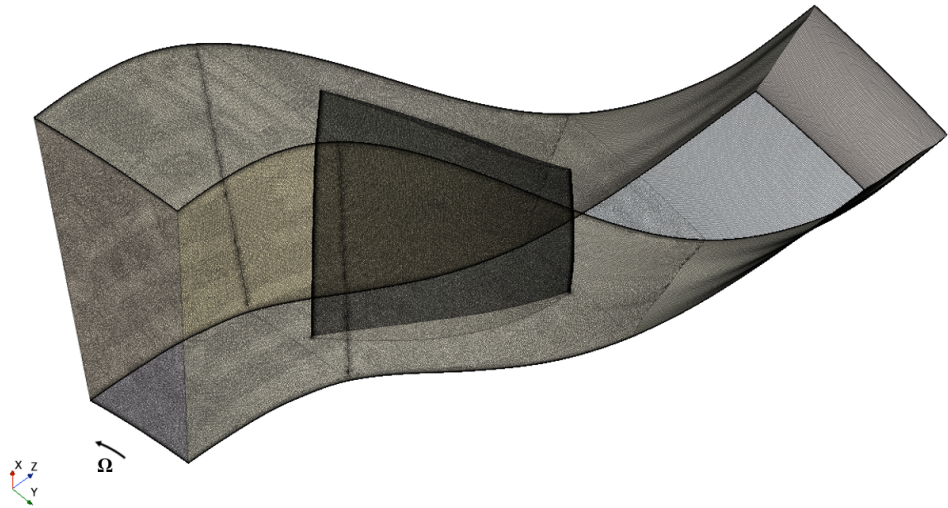


Figure 2.8. A 3D view of the mesh used for the Rotor 37 validation study

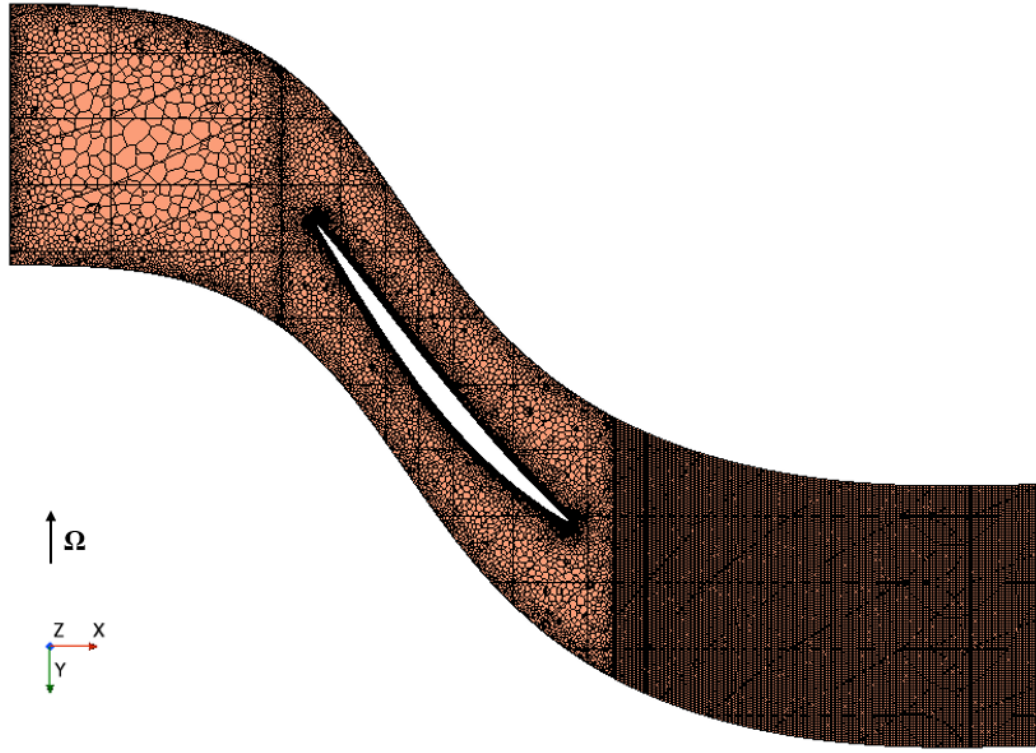


Figure 2.9. Top view of the mesh used for the Rotor 37 validation study at 50% span

2.1.4 Simulation Parameters and Boundary Conditions

The RANS simulations were performed in STAR-CCM+ (v2021.1) [59]. All cases were run three dimensional using the available coupled solver, with second order spatial discretization. The inviscid fluxes were evaluated using Roe’s Flux-Difference Splitting (FDS) scheme [61]. In Chapter 3, the half stage rotor only simulations were run as steady-state calculations in the rotating frame of reference. In Chapter 4, the full stage simulations were run as unsteady calculations with implicit second order discretization in time. The implicit scheme was chosen as it is unconditionally stable [62]. Perfect gas air was the working fluid.

The Menter $k-\omega$ SST turbulence model [63] was used for the studies. The SST

model is a zonal two-equation turbulence model that is $k-\omega$ near the wall and transitions to a $k-\epsilon$ model away from the wall. It employs blending functions to take advantage of the superior performance of the $k-\omega$ model in the near wall regions and the freestream independence of the $k-\epsilon$ model in the far-field. Wall function boundary conditions are also implemented for the SST model. Several studies have shown that it gives more accurate predictions for transonic and turbomachinery flows. Menter and Rumsey [64] performed a comparison study of different turbulence models for different two dimensional transonic flows and concluded that the SST model gave better prediction of shock locations and separation locations. Araya [65] performed a comparison study of the different turbulence models for different three dimensional transonic flows and concluded that the SST model provided the most overall accurate prediction of the flow. It was also observed to be more numerically stable compared to the other models. This was attributed to the Shear Stress Transport (SST) formulation. This model was deemed to be more appropriate in realistically capturing the complex turbulent structures governed by shock-boundary layer interactions and highly separated flows as evidenced in transonic flows. Balasubramanian et al. [66] performed a comparison study of the turbulence models using transonic NASA Rotor 35 and found that $k-\omega$ SST model yielded more accurate predictions of the flow compared to other models.

Specific details about each set of simulations will be described in the respective chapters. Rotationally periodic boundaries were used in order to reduce the domain size. In both Chapters 3 and 4, a domain containing 4 rotor blades was chosen. In this dissertation, the performance implications were analyzed at this common allocation ratio and damage severity, to maximize elucidation of the differences

that geometry had on flow physics and performance. The parameter space available for exploration is vast in terms of number of blades, operating points, damage morphologies. This choice was made such that a one-to-one exact comparison between the performance implications of the different damages could be made.

At the inlet, radial profiles of the stagnation pressure and stagnation temperature were specified based on information provided by GE. Inlet turbulence intensity and length scale were specified to accommodate expected test conditions, also provided by GE. At the outlet, hub static pressure was specified, and a simplified radial equilibrium pressure distribution imposed. The blade and end-wall surfaces were defined as adiabatic non-slip walls.

Averaging techniques used for the computation of stagnation temperature and stagnation pressure are described in Appendix A.

2.1.5 Grid Independence Studies

2.1.5.1 Rotor 37

Since the method validation was performed using the data of NASA Rotor 37, a grid independence study was performed on a single undamaged rotor blade passage to determine an appropriate mesh for its CFD analysis. Four different meshes namely, Coarse, Fine, Finer and Finest, in increasing order of density were run with the same prism layer configuration at the blade surface and endwalls. All the meshes were sub-layer resolved with a $y^+ = 1$. The meshes were compared based on the parameters of interest. Predicted stagnation pressure ratio, stagnation temperature ratio, and adiabatic efficiency varied by less than 0.1% between the

Finer and Finest. Accordingly, the meshing parameters of the Finer cell mesh were used for the method validation study using Rotor 37 as a compromise between accuracy and computational expense. The results of the grid independence study are presented in Table 2.1.

Table 2.1. Results - Grid Independence Study - Rotor 37

| Case | Coarse | Fine | Finer | Finest |
|---------------------------|--------|-------|-------|--------|
| Cell Count | 0.5x | 1.0x | 2.0x | 4x |
| y^+ | 1 | 1 | 1 | 1 |
| SPR/SPR_{finer} | 1.003 | 1.002 | 1.000 | 1.000 |
| STR/STR_{finer} | 1.001 | 1.000 | 1.000 | 1.000 |
| \dot{m}/\dot{m}_{finer} | 1.003 | 1.005 | 1.000 | 1.000 |
| η/η_{finer} | 1.002 | 1.004 | 1.000 | 1.000 |

2.1.5.2 T700

Similar to Section 2.1.5.1, a grid independence study was performed on a single undamaged T700 rotor blade passage to determine an appropriate mesh for its CFD analyses. Predicted stagnation pressure ratio, stagnation temperature ratio, and adiabatic efficiency varied by less than 0.1% between the Finer and Finest meshes. Accordingly, the meshing parameters of the Finer cell mesh for all damaged and undamaged rotors blade and stator passages were used for this study. The results of the grid independence study are presented in Table 2.2.

2.1.6 Target Operating Conditions

Damaged blading implies off-design compressor operation. In order to accommodate real-world off-design operational conditions (i.e., pilot control), several consider-

Table 2.2. Results - Grid Independence Study - T700

| Case | Coarse | Fine | Finer | Finest |
|---------------------------|--------|-------|-------|--------|
| Cell Count | 0.5x | 1.0x | 2.0x | 4.0x |
| y^+ | 1 | 1 | 1 | 1 |
| SPR/SPR_{finer} | 0.994 | 0.993 | 1.000 | 1.000 |
| STR/STR_{finer} | 0.998 | 0.998 | 1.000 | 1.000 |
| \dot{m}/\dot{m}_{finer} | 0.996 | 1.000 | 1.000 | 1.000 |
| η/η_{finer} | 0.995 | 0.996 | 1.000 | 1.001 |

ations were made regarding the target conditions for the simulations with the damaged rotor blades. The propulsion plant output power needed to be maintained for adequate aircraft performance. So, in the T700 turboshaft application, the mass flow rate to, and the shaft speed of, the power turbine were maintained. Hence, for the stage with damaged blades, the target mass flow rate needed to match that with the undamaged rotor operating on-design. Therefore, compressor shaft speed had to be increased. In addition, the stagnation enthalpy rise across the entire six-stage compressor ($\Delta h_{0,1-6}$) was also matched to that of the undamaged compressor.

It was also noted that the percentage of overall compressor stagnation enthalpy rise supplied by the damaged first stage rotor was lower than the undamaged rotor. Accordingly, since the mass flow rate and stagnation enthalpy change across the entire compressor was assumed unchanged, the increment in rotation speed meant that the subsequent undamaged stages of the compressor performed more work. Hence, downstream of the damaged first stage, application of the Euler turbomachinery equation yielded for each rotor

$$\Delta h_{0,f} = \Delta h_{0,i} \frac{\Omega_f}{\Omega_i} \frac{\Delta v_{\theta,f}}{\Delta v_{\theta,i}}, \quad (2.1)$$

where subscripts \cdot_i , and \cdot_f denote the initial/on-design and final/off-design conditions respectively.

Additionally, as per meanline velocity triangles for these rotors, increasing the compressor shaft speed Ω led to a change in the tangential component of the absolute velocity (v_θ) at constant mass flow rate (v_z remained the same) as shown in Figure 2.10.

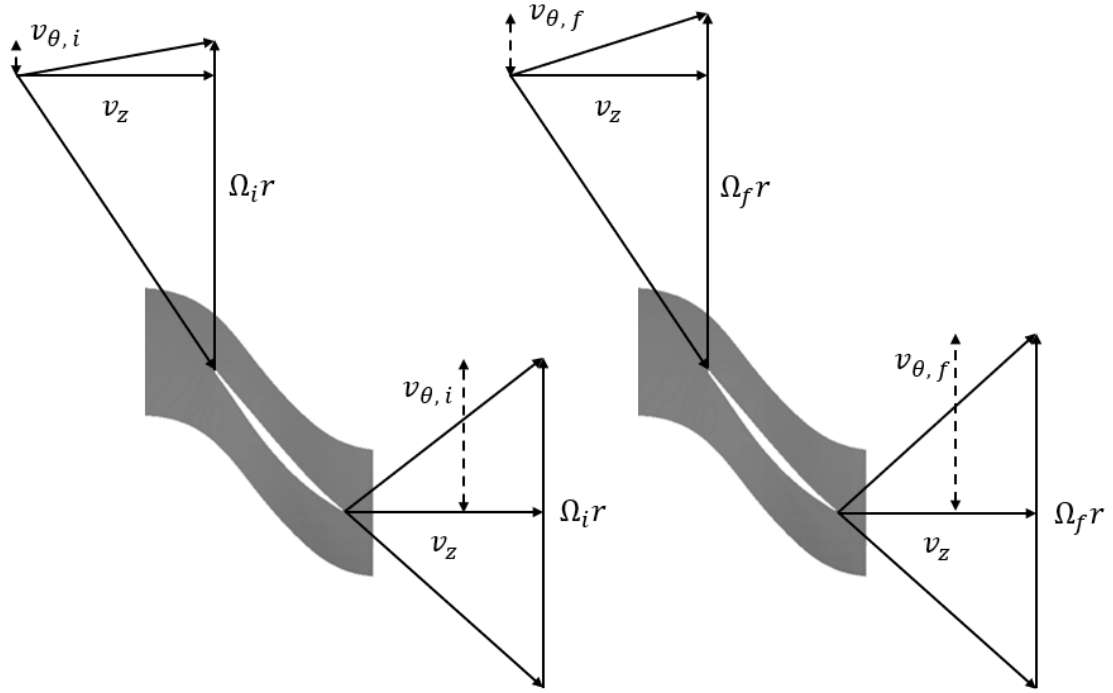


Figure 2.10. Velocity triangles at design point (left), off-design point (at increased Ω) (right)

A linear relationship between flow turning ratio ($\Delta v_{\theta,f}/\Delta v_{\theta,i}$) and compressor shaft speed ratio (Ω_f/Ω_i) for the rotors was determined through a study of a single undamaged stage 1 rotor blade within the operational range of compressor shaft

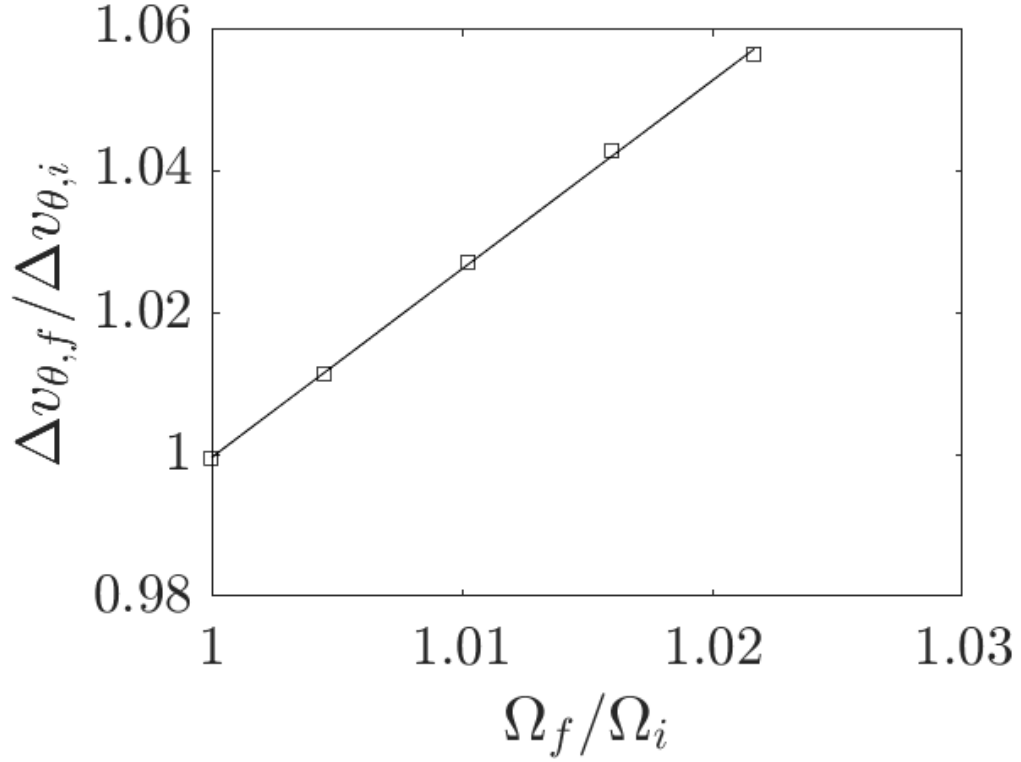


Figure 2.11. $\frac{\Delta v_{\theta,f}}{\Delta v_{\theta,i}}$ vs. $\frac{\Omega_f}{\Omega_i}$ for five selected compressor shaft speeds in range of interest and linear fit

speed Ω . This is illustrated in Figure 2.11 which plots the flow turning ratio vs. compressor shaft speed ratio for five shaft speeds in the range of interest. Linear regression yielded

$$\frac{\Delta v_{\theta,f}}{\Delta v_{\theta,i}} = -1.55 + 2.55 \frac{\Omega_f}{\Omega_i} \quad (2.2)$$

Considering the undamaged compressor, the stagnation enthalpy change across the 5 axial and 1 centrifugal stages is given by $\Delta h_{0,1-6,und}$ and the stagnation enthalpy change for the damaged compressor can be expressed as

$$\Delta h_{0,1-6} = \Delta h_{0,1,tgt} + \Delta h_{0,2-6} = \Delta h_{0,1-6,und} \quad (2.3)$$

Hence, the target stagnation enthalpy change for the damaged first stage rotor was computed using Eqs. 2.1, 2.2 and 2.3 as

$$\Delta h_{0,1,tgt} = \Delta h_{0,1-6,und} - \frac{\Omega_f}{\Omega_i} \frac{\Delta v_{\theta,f}}{\Delta v_{\theta,i}} \Delta h_{0,2-6,und} \quad (2.4)$$

where in Eq. 2.4 the design intent stagnation enthalpy rise for each stage was known/supplied from the engine manufacturer (i.e., $\Delta h_{0,1-6,und}$, $\Delta h_{0,2-6,und}$) and subscripts \cdot_i , and \cdot_f denote the initial/undamaged and final/damaged conditions respectively.

In summary, for the damaged stage simulations, the rotation speed and the outlet hub static pressure were adjusted, during iteration, such that the converged mass flow rate matched that of the on-design mass flow rate, and the stagnation enthalpy rise for the damaged stage satisfied Eq. 2.4.

2.2 Method Validation - NASA Rotor 37

Experimental data from T700 field tests are forthcoming, therefore the CFD approach was validated against the well-studied NASA Rotor 37 transonic axial compressor. Rotor 37 is a low aspect ratio inlet rotor for a core compressor. It has 36 multiple circular-arc (MCA) blades and a design pressure ratio of 2.106 at a mass flow of 20.19 kg/sec. Rotor 37 was designed and tested by Reid and Moore [67] as an effort to create a well-documented and highly detailed data-set for bench-marking of CFD codes for transonic compressor applications. Subsequent testing of Rotor 37 was pursued by Suder [68].

The same meshing and simulation approaches presented in Section 2.1.2 were

used to analyze the rotor (here, single blade row, steady-state, relative frame of reference simulation) at a given experimental operating point near peak efficiency, i.e., at 98% of the experimental choked mass flow rate. Here, results are compared to the experimental measurements of Suder [68] and the CFD results of Ameri [69] and Bruna and Turner [70]. Table 2.3 shows a comparison of the overall performance parameters. Stagnation pressure ratio (SPR), stagnation temperature ratio (STR) and adiabatic efficiency (η_{tt}) predictions were observed to be in very close agreement with the experimental data and other CFD results.

Table 2.3. Rotor 37 overall performance parameters

| | Suder | Ameri | Bruna & Turner | Present |
|---------------------|-------|-------|----------------|---------|
| \dot{m}/\dot{m}_c | 0.982 | 0.980 | 0.985 | 0.980 |
| <i>SPR</i> | 2.091 | 2.058 | 2.087 | 2.063 |
| <i>STR</i> | 1.267 | 1.267 | 1.270 | 1.270 |
| η_{tt} | 0.878 | 0.860 | 0.866 | 0.852 |

Figure 2.12 shows predicted contours of instantaneous relative Mach number at 70% span, illustrating the fairly complicated shock system, attendant boundary layer interaction and wake field in this flow. As expected, a three dimensional bow shock was observed at the leading edge which extends across the blade passage. This results in a lambda shock - boundary layer interaction at the suction surface of the adjacent blade. There was also some development of the wake downstream of the rotor.

Figure 2.13 show the spanwise distribution of mass weighted STR at the outlet. It was observed that there is good agreement between the present results and the experiment and previous CFD efforts. The over-prediction of the STR by the CFD

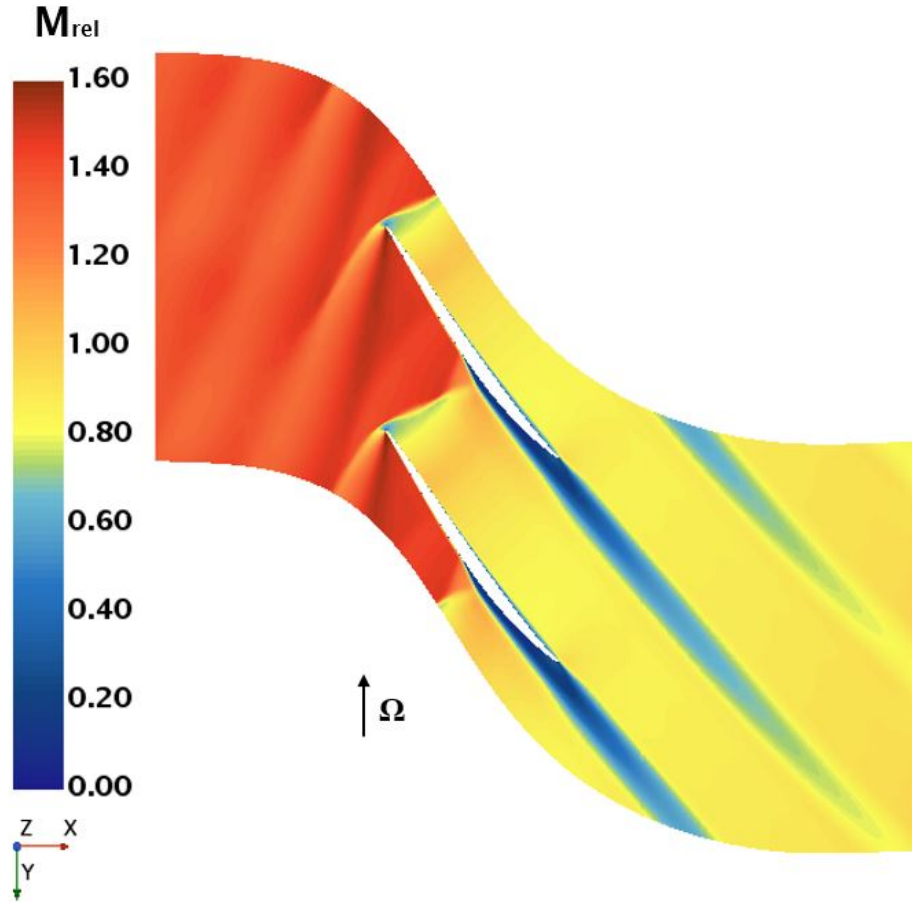


Figure 2.12. Rotor 37 instantaneous relative Mach number contours at 70% span

efforts was attributed to the outer wall thermal boundary condition. Bruna and Turner [70] performed a separate analysis with an isothermal boundary condition, where the shroud was set to the inlet stagnation temperature. This yielded better predictions of the STR and adiabatic efficiency profiles at the end-walls. However, they also stated that an isothermal boundary was not consistent with the physics of the problem as the casing is not isothermal in real-life conditions. They recommended the use of a conjugate heat transfer approach to model the thermal characteristics of this boundary, which is outside the scope of this dissertation.

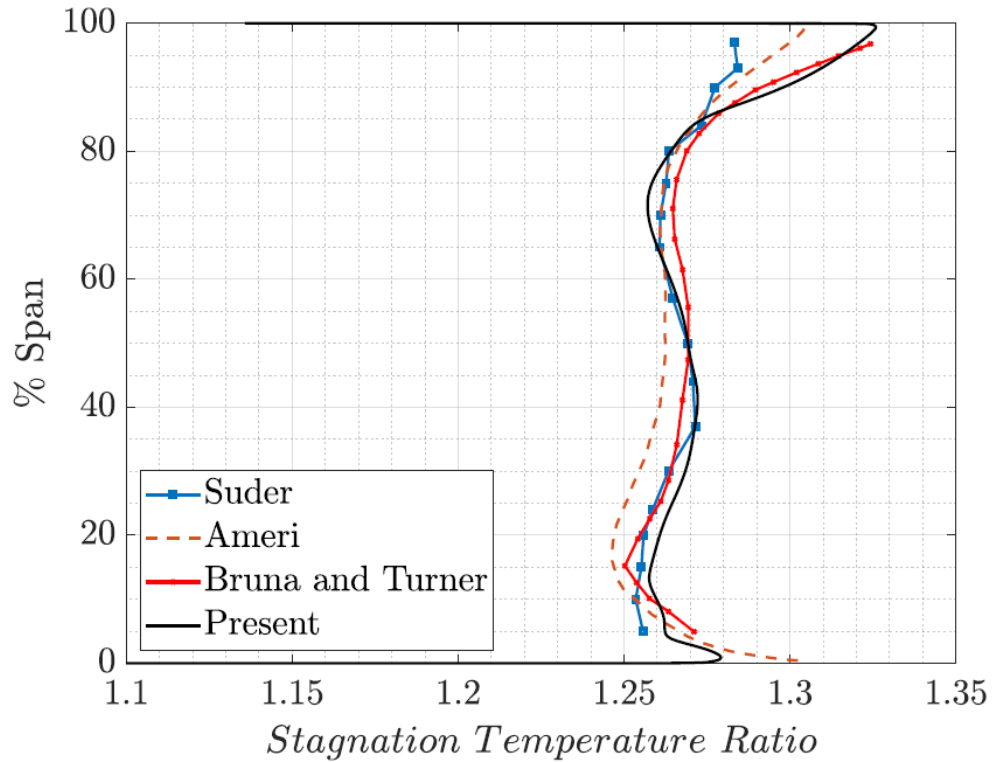


Figure 2.13. Rotor 37 spanwise distribution of stagnation temperature ratio at the outlet

Figure 2.14 show the spanwise distribution of enthalpy weighted SPR at the outlet. Again, good agreement was observed between the present results and the experiment and previous CFD analyses. There was an over-prediction of the SPR in the near hub region. Discrepancies between the CFD models and the experiment, specifically in the hub region, were attributed to hub leakage. Shabbir et al. [71] observed that hub leakage occurred through the hub clearances. The hub flow path of the NASA Rotor 37 features non-rotating bodies both upstream and downstream of the rotor with an axial clearance of about 0.75mm (1.8% of the rotor hub axial chord length). This hub leakage flow was attributed to lead to the deficit in the

stagnation pressure rise at the hub compared to the CFD analyses where the hub leakage flow was not explicitly modeled.

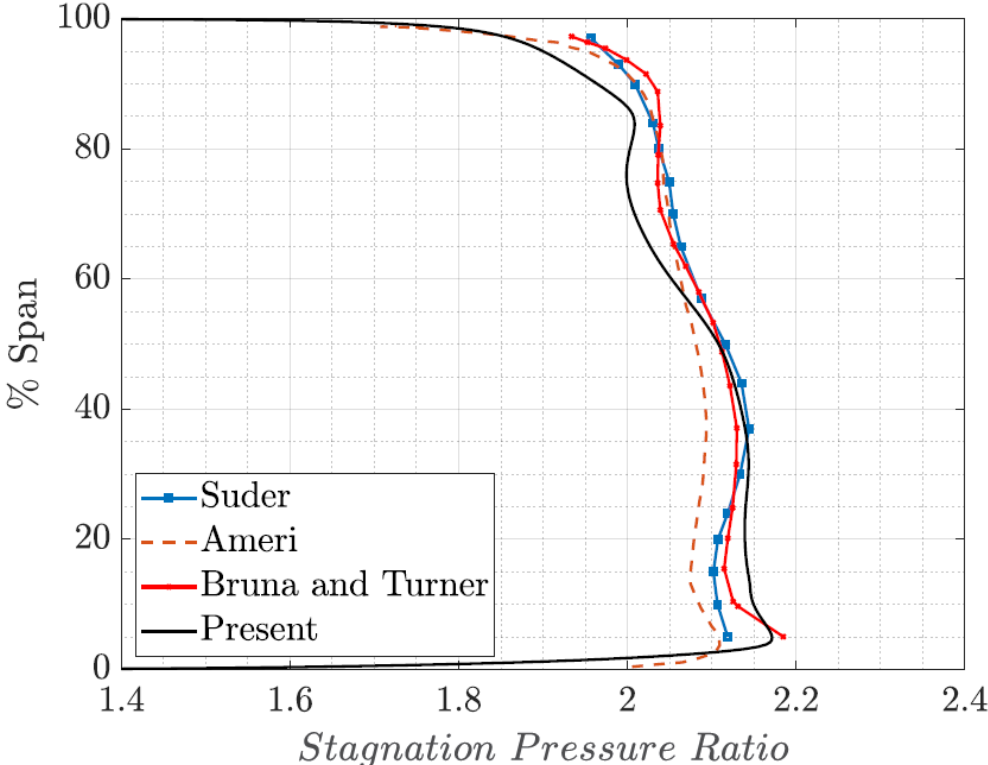


Figure 2.14. Rotor 37 spanwise distribution of stagnation pressure ratio at the outlet

Further discrepancies between the CFD models and experiments were associated with turbulence modeling [72]. Further discussion of the Rotor 37 analysis was beyond the scope of this dissertation.

2.2.1 Conclusion - Method Validation

The results of this method validation using Rotor 37 justified that the meshing and modeling methods used were suitable for the parametric study of the T700 stage conducted in Chapters 3 and 4.

Chapter 3 |

Steady-State Rotor only Simulations

This chapter presents the results for the steady-state simulations performed for the first stage rotor of the axial compressor of the T700 in the rotating frame of reference. A brief discussion of the computational domain and simulation parameters is done. Results of the baseline undamaged T700 first stage rotor are discussed followed by a comparison with the damaged rotor blade cases.

3.1 Computational Domain and Simulation Parameters

A computational domain with 4 rotor blades was considered for each case, and is shown in Figure 3.1. The mesh at 50% span is shown in Figure 3.2. In this work, three undamaged and one damaged blade were used for each four-blade annulus section. This configuration was been selected to reflect realistic damage scenarios where all the blades do not exhibit the same damage.

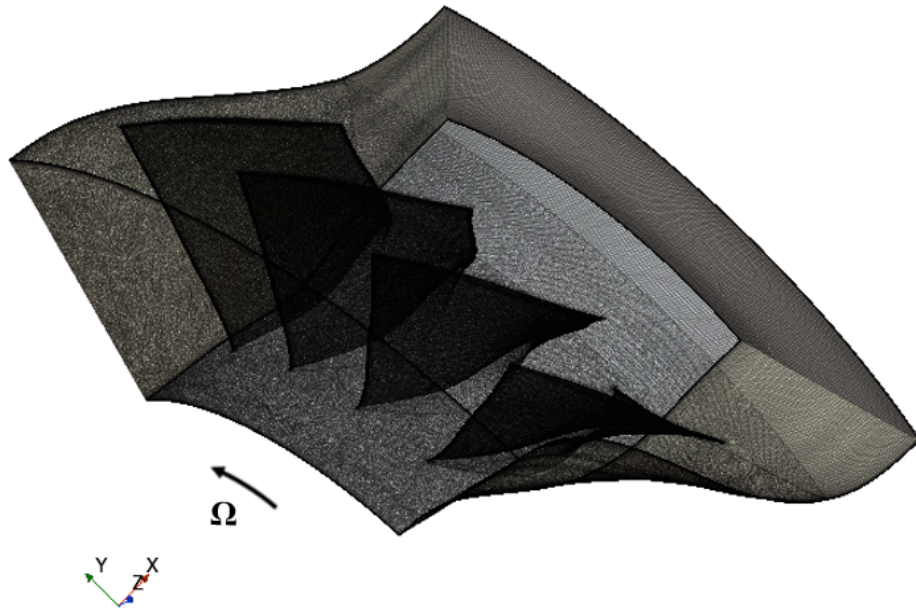


Figure 3.1. A view of the computational domain for the rotor only simulation

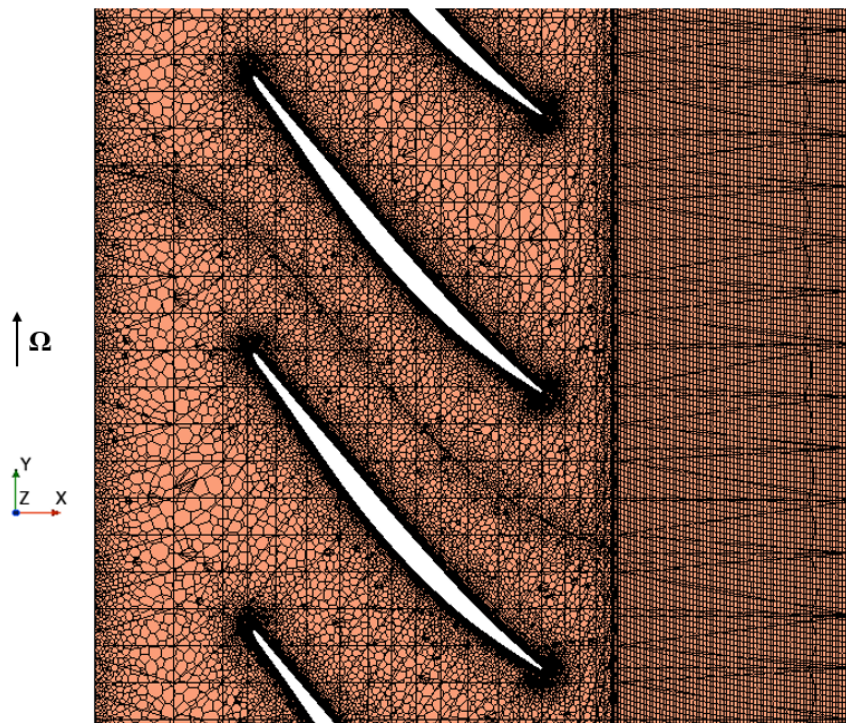


Figure 3.2. A view of the full stage computational domain at 50% span

The simulations were set up as discussed in Chapter 2 Section 2.1.4. In addition, all cases were run as steady-state simulations in the rotating frame of reference.

3.2 Results

3.2.1 Undamaged Rotor

Results for the baseline undamaged T700 first stage rotor are presented first. Like Rotor 37, this is a transonic rotor and a complicated compressible wave field arises, as illustrated by the relative Mach number contours at 90% span shown in Figure 3.3.

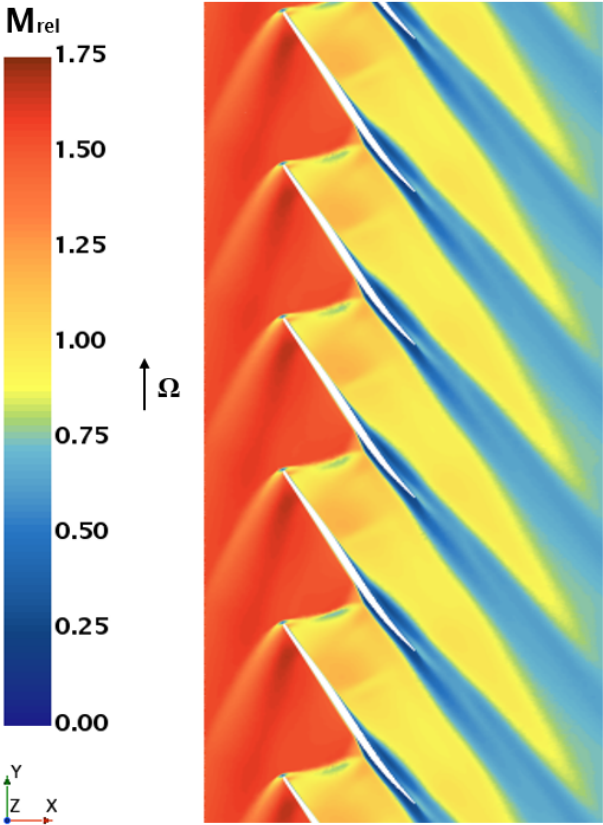


Figure 3.3. Relative Mach number contours at 90% span of the Undamaged case

The bow shock propagated upstream on the suction side and intersected the adjacent suction surface aft of midchord as a lambda shock which decelerated the boundary layer there. Expansion waves/acceleration were observed on the pressure side. Downstream of the shock-boundary-layer interaction, a weak normal shock appeared and at this near casing location separated the pressure side boundary layer. The shock system in the blade passage clearly gave rise to significant boundary layer and wake thickening.

Figure 3.4 shows a front view of relative Mach number contours at $x/c_{hub} = 0.27$ downstream of the hub leading edge. The spanwise variation of the shock location was evident. A low momentum region at the casing was induced by the impinging shock there.

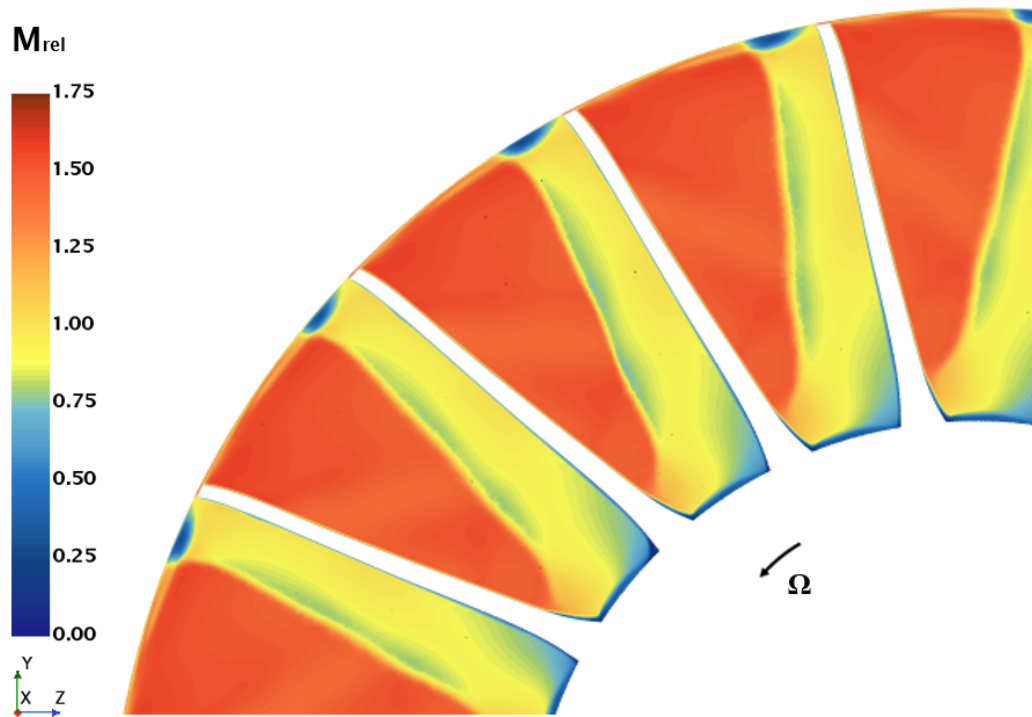


Figure 3.4. Relative Mach number contours at $(x/c)_{hub} = 0.27$; Undamaged

The undamaged rotor has a tip clearance of 0.4% of span, and the tip clearance flow was visualized in Figure 3.5 using relative frame streamlines seeded above the blade tip. Several stream-wise cuts are shown with contours of vorticity. The tip vortex remained confined to the near casing region as it migrated across the passage to the adjacent blade's pressure surface. Interactions of the vorticity associated with the tip vortex, relative endwall rotation and blade surface boundary layers were observed.

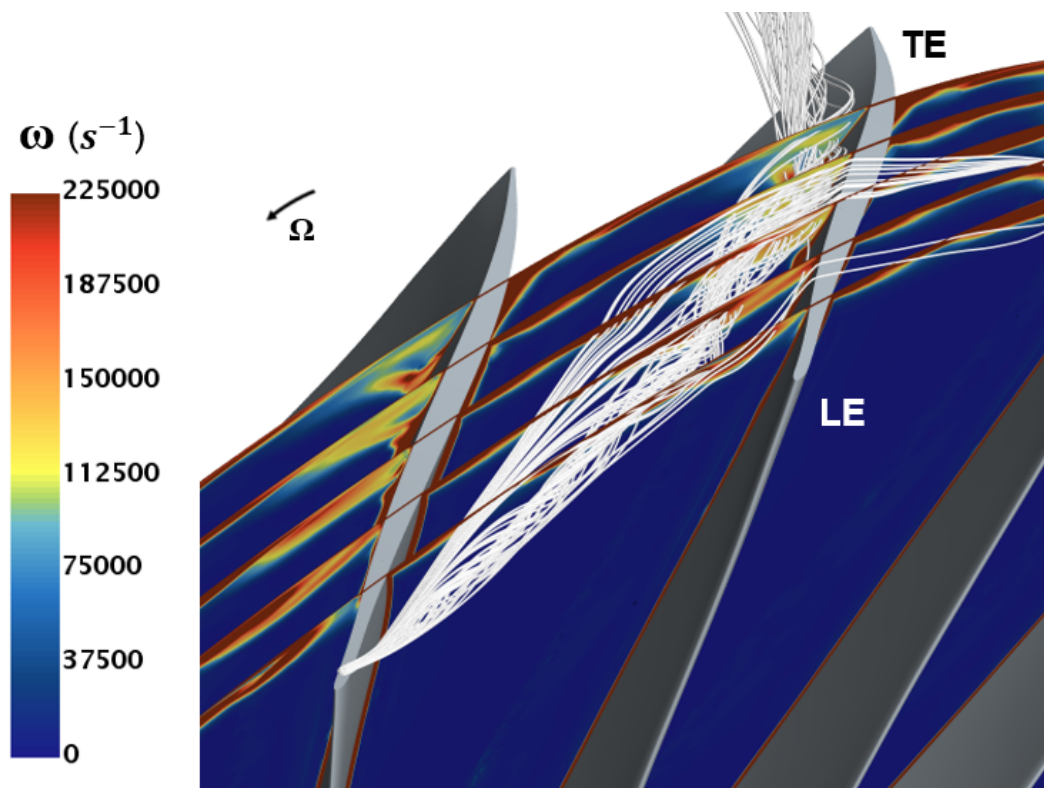


Figure 3.5. Tip clearance gap streamlines of Undamaged case with contours of vorticity at several planes downstream

Figure 3.6 shows a top view of the same streamlines, with a 0.98 span surface contoured by relative Mach number. In this view, the interaction of the tip vortex with the passage shock wave was observed, which is seen to redirect and decelerate

the vortex, observations that were consistent with the Rotor 37 studies of Yamada et al. [73].

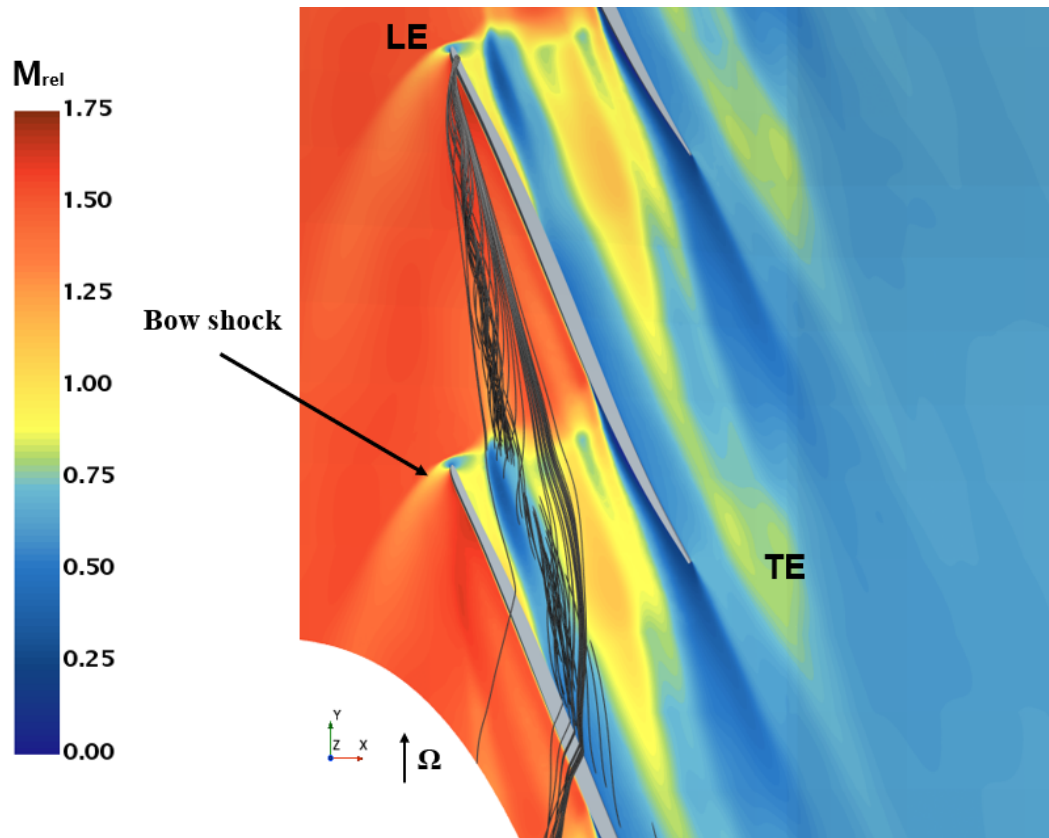


Figure 3.6. Streamlines in the tip clearance gap region with contours of relative Mach number at 98% span for the Undamaged case

3.2.2 Damaged Configurations

Here, qualitative and quantitative comparisons of the damaged configurations to the baseline undamaged case are presented. First, the Cragged configuration, Figure 2.5, is considered. Figure 3.7 shows relative Mach number contours at 90% span. In this figure, and all subsequent blade-to-blade representations, the bottom blade is damaged, the upper three undamaged. Comparing the two contour plots, some

differences were observed in the shock and boundary layer interactions, and this was somewhat expected since there was some damage to the rotor blade along the spanwise length of the leading edge. The slight shift downstream of the bow shock was apparent. There was an acceleration of the flow downstream of the bow shock. Some off-design physics was evidenced in all the four blade passages.

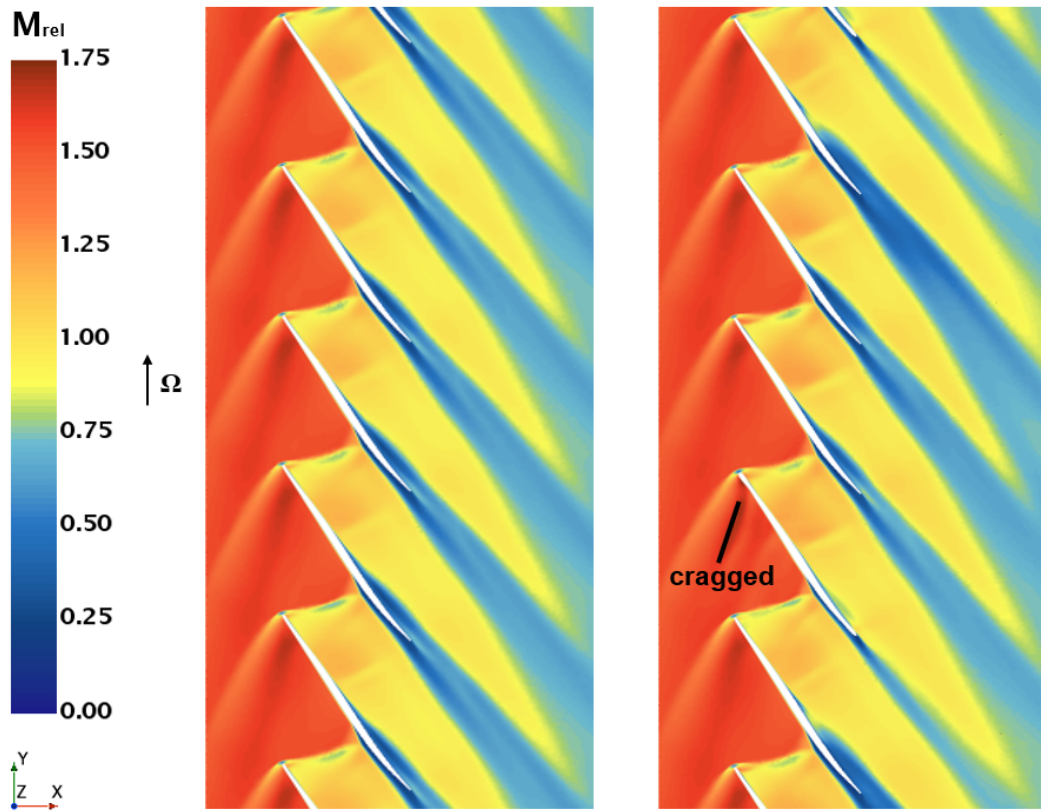


Figure 3.7. Relative Mach number contours at 90% span; undamaged (left), Cragged damage (right)

Figure 3.8 shows relative Mach number contours at 90% span for the Eroded damage case. Here, the impact of chord loss at the leading and trailing edges was clearly observed, and the resultant modifications to the flow field. The leading edge and its attendant bow shock were further downstream compared to the Undamaged case. A richer shock-expansion field arose with the second normal shock emanating

from the pressure surface, significantly stronger than in the Undamaged case, and impinged on the wake of the adjacent blade, farther downstream than in the Undamaged case. Although relative Mach numbers were supersonic, the axial Mach number did not exceed 1, so upstream influence of the Eroded passage flow arose, leading to significant off design physics in all four of the blade passages. The wake behind the eroded blade was small and was observed to quickly dissipate at this location.

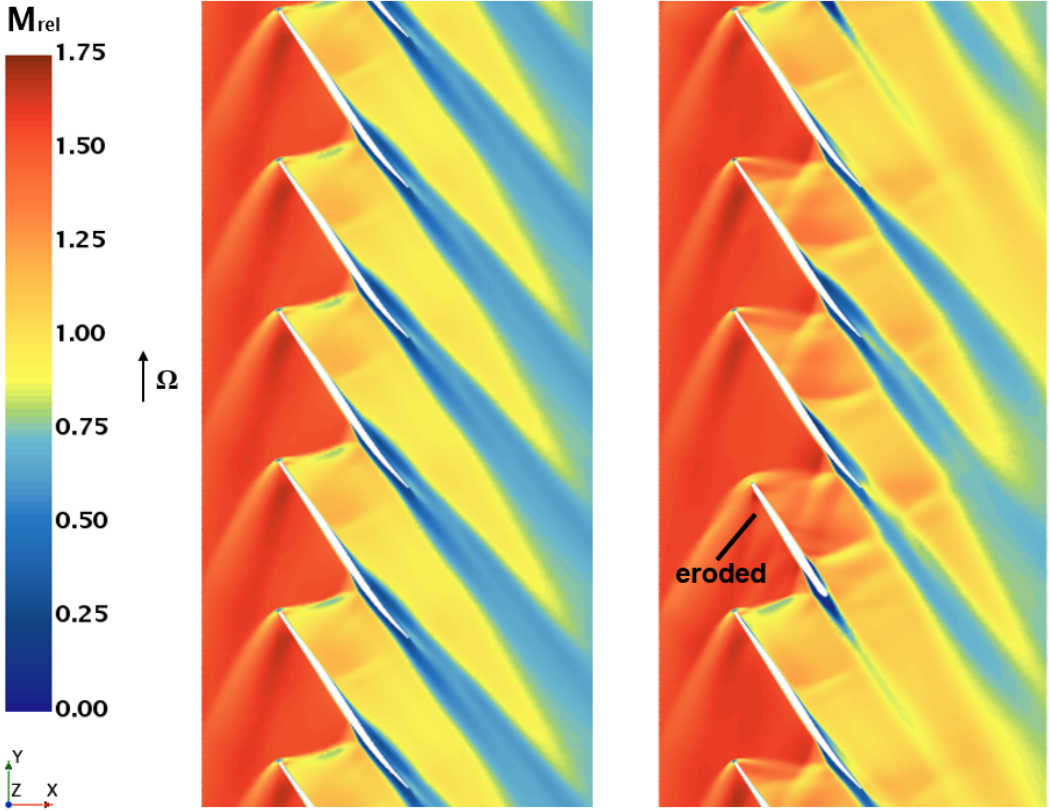


Figure 3.8. Relative Mach number contours at 90% span; undamaged (left), Eroded damage (right)

Figure 3.9 shows relative Mach number contours at 90% span for the Curled damage case. The bow shock was much stronger since the leading edge curl acted as a much larger leading edge. A reverse flow region arose immediately downstream

of the curl feature. The flow field within the blade passage blades was observed to be quite complex with five distinct shocks-expansion pairs appearing. The wakes of all four blade passages were significantly impacted.

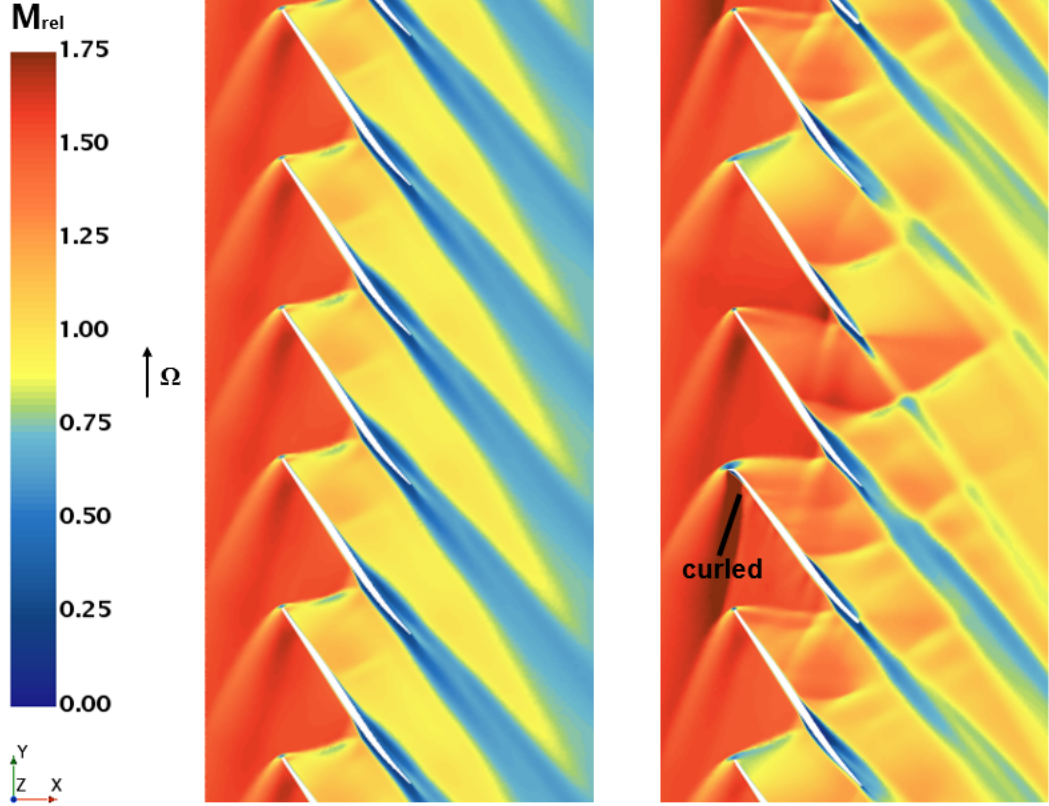


Figure 3.9. Relative Mach number contours at 90% span; undamaged (left), Curled damage (right)

In Figure 3.10, relative stagnation pressure contours were plotted at $(x/c)_{hub} = .66$ downstream of the hub leading edge for the damaged and undamaged cases. In the undamaged blade passages, a high loss region was observed at the casing-suction surface corner associated with the shock-tip clearance vortex physics discussed above (Figure 3.5). A number of additional observations applied. Firstly, a low $p_{0,rel}$ region arose on the suction surface near midspan for all passages/cases. This high loss region was due to boundary layer interaction with the adjacent blade's

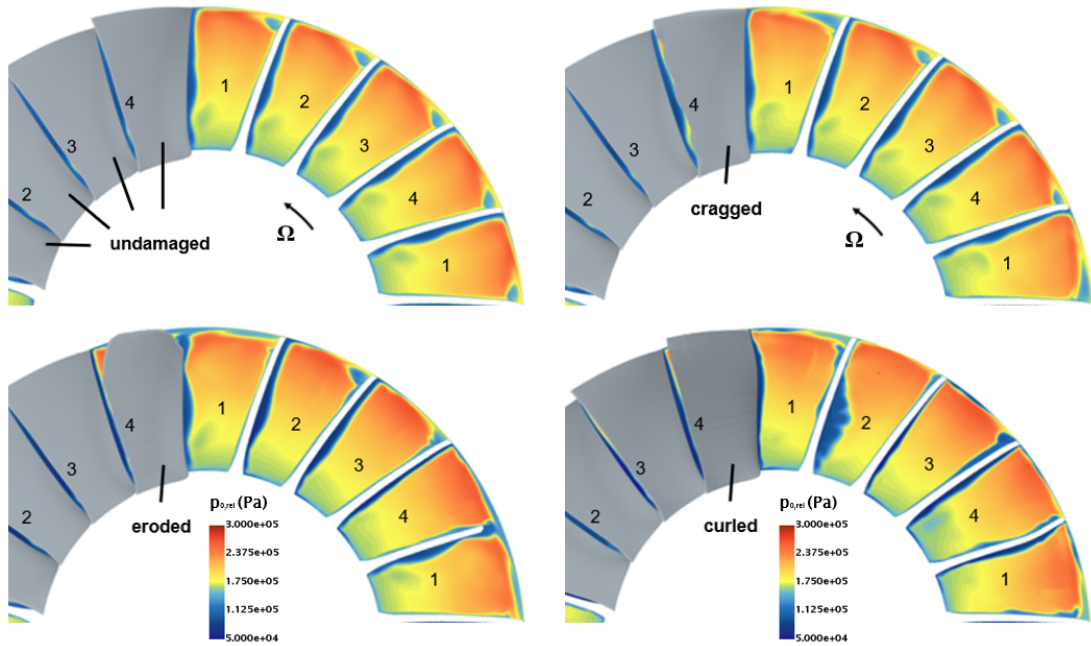


Figure 3.10. Instantaneous relative stagnation pressure contours at $(x/c)_{hub} = 0.66$; Undamaged (top-left), Eroded (bottom-left), Cragged (top-right), Curled (bottom-right)

bow shock. The size and shape of this loss region was significantly impacted by the three damaged blade geometries. The Curled tip blade in particular gave rise to significantly larger regions of high loss adjacent to the blade surfaces in passages on either side of the damage.

Rotor performance parameters are summarized in Table 3.1. These were defined based on computational domain outlet and inlet boundary values. These parameters were normalized with the results for the Undamaged case. The averaging techniques outlined in Appendix A were employed. Specifically, enthalpy averaged stagnation pressure ratio (SPR), mass weighted stagnation temperature ratio (STR), and adiabatic efficiency (based on mass weighted enthalpies) are tabulated. All three damaged rotors exhibited significant reductions in the stagnation pressure ratio, stagnation temperatures ratio and adiabatic efficiency. Consistent with the

observations above, the Cragged rotor exhibited modest performance deterioration, followed by more significant reductions for the Eroded blade, and yet more severe impact for the Curled damage.

Table 3.1. Comparison of Overall Performance Parameters

| Case | Undamaged | Cragged | Eroded | Curled |
|-----------------------------------|-----------|---------|--------|--------|
| RPM/RPM_{und} | 1.000 | 1.001 | 1.006 | 1.007 |
| $\Delta h_{01}/\Delta h_{01,und}$ | 1.000 | 0.975 | 0.888 | 0.856 |
| SPR/SPR_{und} | 1.000 | 0.981 | 0.916 | 0.854 |
| STR/SPR_{und} | 1.000 | 0.995 | 0.977 | 0.967 |
| $\eta_{tt}/\eta_{tt,und}$ | 1.000 | 0.990 | 0.960 | 0.887 |

Figures 3.11 and 3.12 show the spanwise distributions of mass-weighted STR and enthalpy-averaged SPR. These were normalized using the mid-span values of the Undamaged case. A number of observations were forthcoming. The undamaged blading exhibited a near-linear reduction in stagnation temperature from 10% span to midspan, consistent with the roughly linear decrease in turning observed in the normalized absolute flow angle profile shown in Figure 3.13. The STR profile remained approximately flat from midspan to approximately 80% span and then increased markedly to the near tip region where endwall effects manifest. These outer span behaviors were again consistent with the absolute flow angle profile. The SPR variation was consistent with Rotor 37 (Figure 2.14). It was observed that the SPR decreases by about 15% from the near hub region to the near tip region. Near the endwall, the SPR decreased significantly. The normalized adiabatic efficiency also decreased across the span, as shown in Figure 3.14, from approximately 1.1 near the hub to 0.85 at 80% span, then dropping precipitously to near 0.4 at the casing, this arising due to increasing M_{rel} and shock strength with radius, tip

clearance flow, and relative casing rotation.

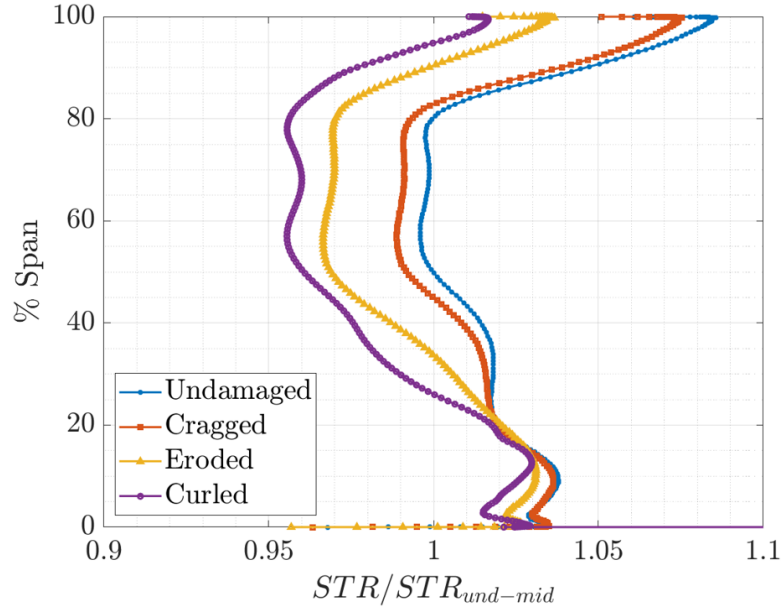


Figure 3.11. Spanwise distribution of normalized stagnation temperature ratio at the outlet

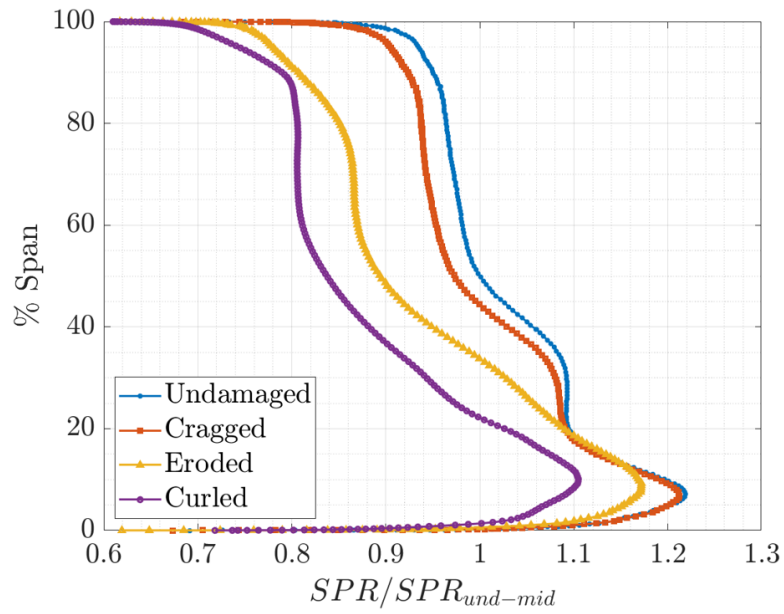


Figure 3.12. Spanwise distribution of normalized stagnation pressure ratio at the outlet

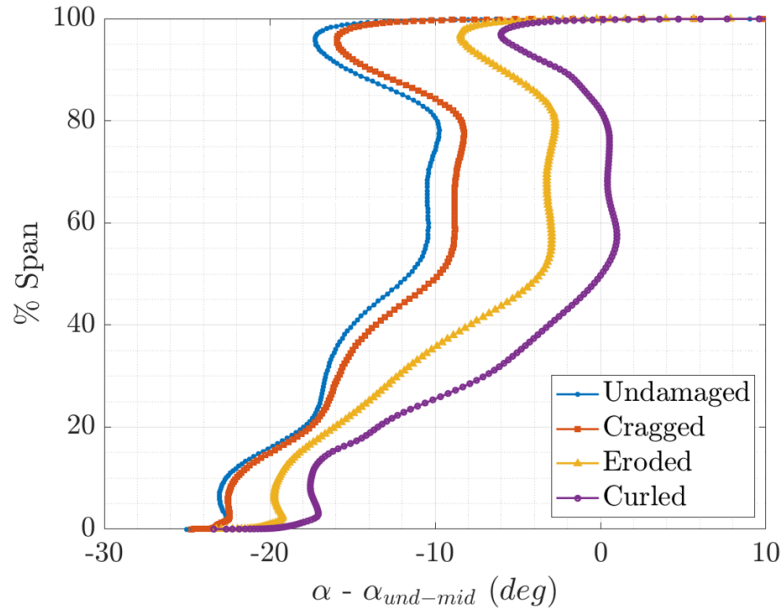


Figure 3.13. Spanwise distribution of absolute flow angle at the outlet

The damaged rotor performance profiles showed generally consistent spanwise trends with the undamaged rotor, since the physics of the damaged passage flow field remained largely the same (boundary/operating conditions, wave fields, secondary flows), and only one blade of every four is damaged. However, there was less work done (SPR, STR), and increased loss (SPR and η_{tt}), across the entire span for all three damage modes. Damage severity could again be rank ordered from Cragged, which showed only modest deterioration of the four parameters considered, across the span, followed by Eroded and Curled, which exhibited highly compromised performance deterioration. In general, the damaged blades performed less turning, thereby imparting lower stagnation enthalpy rise to the flow. Also, the shock, boundary layer and wake losses were successively higher in these blades, as illustrated above. Lastly, performance deterioration was observed to be most significant in the outer spans where most of the damage is present.

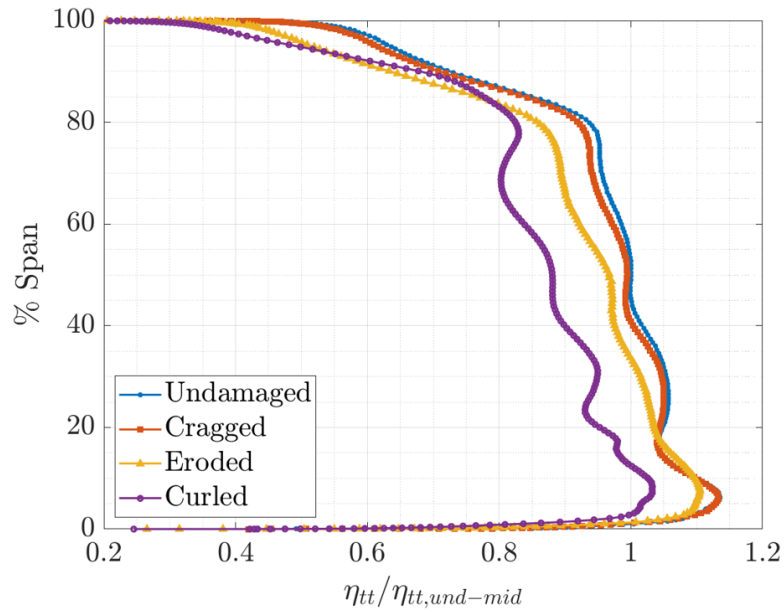


Figure 3.14. Spanwise distribution of normalized adiabatic efficiency at the outlet

3.2.3 Impact on SFC

In Section 2.4, a method was presented for setting appropriate operating and boundary conditions for a damaged compressor CFD analysis, i.e., as a pilot would operate the engine under these circumstances. Maintaining full power with significantly reduced stage 1 compressor efficiency detrimentally impacts overall engine SFC. Estimating this power-plant SFC reduction is of importance to aircraft operators in that it impacts mission duration, fuel costs and off-platform refurbishment planning.

In this case, the SFC was estimated for the complete T700 engine. In Figure 3.15, a side-view cutaway of the T700 compressor is shown.

A standard gas turbine cycle deck was written to estimate the impact of the stage 1 rotor damage modes studied here on expected turboshaft SFC. The goal was to have an easily adaptable/upgradable tool to assess compressor and overall

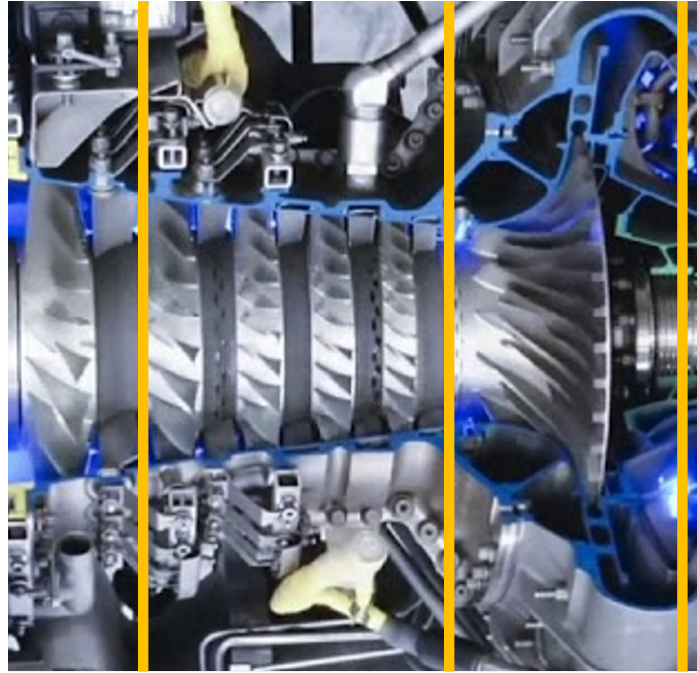


Figure 3.15. Side cut-away view of T700 compressor section [56]

engine performance using clean and damaged blade measurements (T700/NAVAIR) and present CFD.

For this machine, the compressor was "split" into stage 1, stages 2-5 and the centrifugal stage, per the numbering shown in the figure. This is consistent with stage stacking techniques used for multi-stage compressor analysis. One can easily derive performance stacking relations for incremental stagnation pressures and temperatures within the compressor Eqs. 3.1-3.3, leading to overall compressor stagnation pressure and temperature ratios Eq. 3.4.

$$p_{0,2a} = p_{0,2} CPR_{S1}, \quad T_{0,2a} = T_{0,2} \left[1 + \frac{1}{\eta_{S1}} (CPR_{S1}^{(\gamma-1)/\gamma} - 1) \right] \quad (3.1)$$

$$p_{0,2b} = p_{0,2a} CPR_{S2-5}, T_{0,2b} = T_{0,2a} \left[1 + \frac{1}{\eta_{S2-5}} (CPR_{S2-5}^{(\gamma-1)/\gamma} - 1)\right] \quad (3.2)$$

$$p_{0,3} = p_{0,2b} CPR_{SC}, T_{0,3} = T_{0,2b} \left[1 + \frac{1}{\eta_{SC}} (CPR_{SC}^{(\gamma-1)/\gamma} - 1)\right] \quad (3.3)$$

$$p_{0,3} = p_{0,2} CPR, T_{0,3} = T_{0,2} \left[1 + \frac{1}{\eta_c} (CPR^{(\gamma-1)/\gamma} - 1)\right] \quad (3.4)$$

By invoking reasonable/known assumptions for the efficiencies of the inlet, turbine, burner, and exhaust engine sections, as well as assumptions for fuel type, bypass ratio and free-stream Mach number (both zero here), and turbine/exhaust specific heat ratio, one can derive an expression for SFC following [4] (for example). The inputs to the model were the predicted or measured stage 1 stagnation pressure ratio, CPR_{S1} , and adiabatic efficiency, η_{S1} , and the measured, computed (or design intent) values for the other compressor stages, CPR_{S2-5} , CPR_{S3} , η_{S2-5} , η_{S3} .

In Figure 3.16, predicted values of SFC, normalized by the undamaged model value, were plotted for the four configurations. As the nature of the damage became more severe, the normalized SFC increased as expected, to a maximum of just over 3% increase for the curled damage blade. This was accompanied by an overall reduction in CPR (also normalized) of 14.5% as plotted in Figure 3.17.

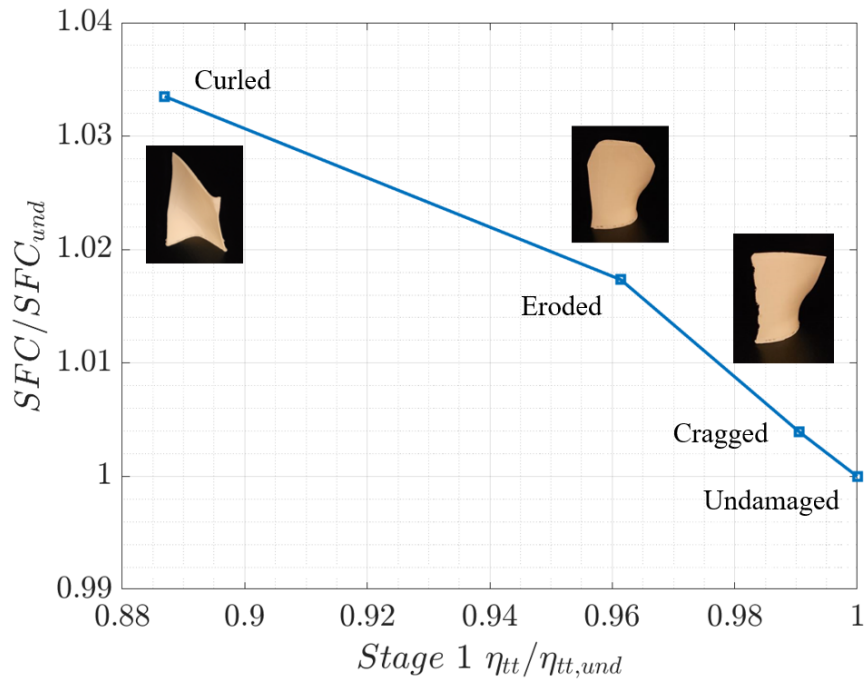


Figure 3.16. Normalized SFC vs Normalized Stage 1 Adiabatic Efficiency

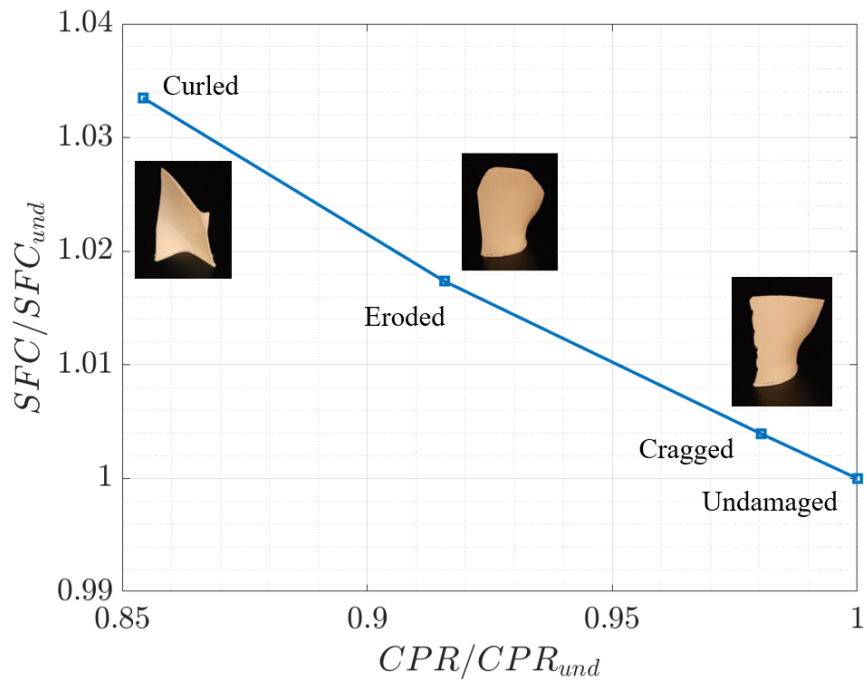


Figure 3.17. Normalized SFC vs Normalized Compressor Pressure Ratio

Chapter 4 |

Unsteady Full Stage Simulations

This chapter presents the results for the unsteady simulations performed for the first stage of the axial compressor of the T700. A brief discussion of the computational domain and simulation parameters is performed. Results of the baseline undamaged T700 first stage are discussed followed by a comparison with the damaged rotor blade cases. The differences between the steady state rotor only simulations and the unsteady full stage simulations are discussed.

4.1 Computational Domain and Simulation Parameters

A computational domain with 4 rotor blades and 6 stator blades was considered for each case, and is shown in Figure 4.1. The mesh at 50% span is shown in Figure 4.2. The ratio corresponds very closely to the integer blade-vane-count in the T700 first stage. The ratio of 4:6 was used rather than 2:3 to enable analysis of damage scenarios where all blades do not exhibit the same damage. In this work, three undamaged blades and 1 damaged blade were considered for each four-blade

annulus section.

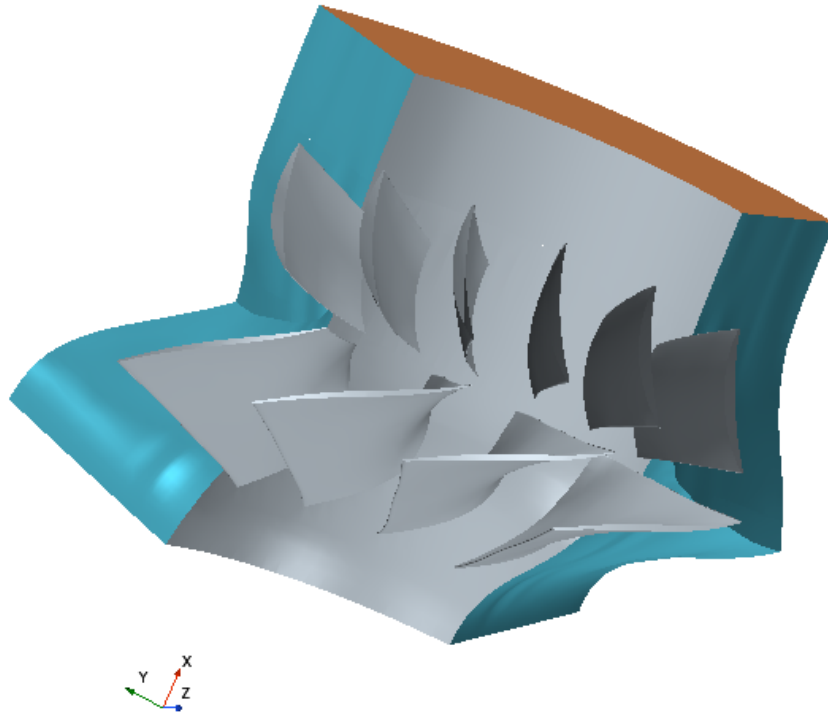


Figure 4.1. A view of the full stage computational domain

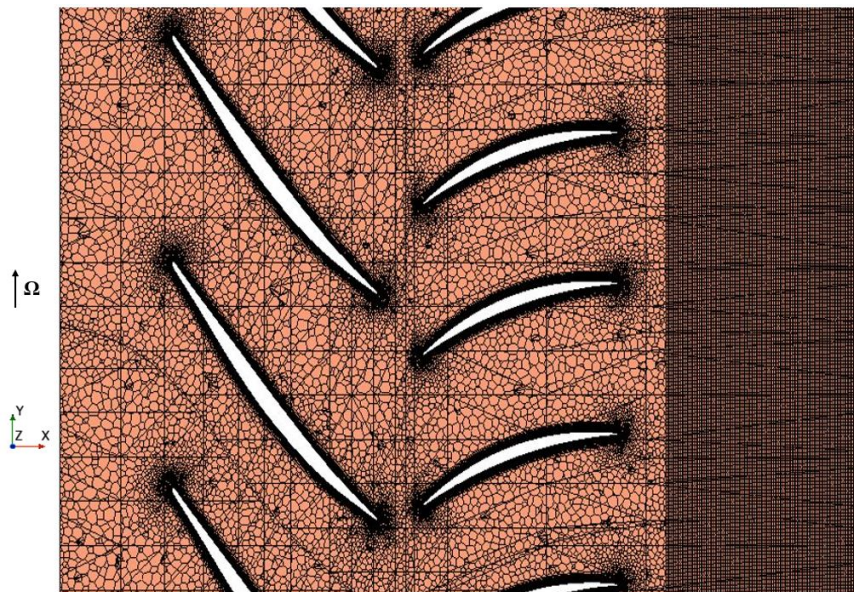


Figure 4.2. A view of the mesh for the Undamaged case at 50% span

The simulations were set up as in discussed in Chapter 2 Section 2.1.4. In addition, all cases were run time accurate, using the available coupled solver, with second order discretization in space and time. A physical timestep of 1.37×10^{-6} seconds was used, corresponding to 50 timesteps per rotor passing period. Each simulation was run for about 4000 rotor passing periods to achieve near statistical stationarity for the 4 rotor blade (1 damaged): 6 stator vane configurations studied. An exactly conservative sliding interface was defined between the rotor and stator meshes. The simulations were run in the absolute frame-of-reference, with rotor mesh motion.

4.2 Results

4.2.1 Undamaged Stage

Results for the baseline undamaged T700 first stage are presented in a fashion similar to Chapter 3 Section 3.2.1. Similar to the first stage rotor, a complicated compressible wave field arose, as illustrated by the instantaneous relative Mach number contours at 90% span shown in Figure 4.3. This and all subsequent instantaneous visualizations were obtained at the same physical timestep (i.e., relative rotor-stator positions). The bow shock propagated upstream on the suction side and intersected the adjacent suction surface aft of midchord as a lambda shock which decelerated the boundary layer there. Expansion waves/acceleration were observed on the pressure side. Downstream of the shock-boundary-layer interaction, a weak normal shock appeared and at this near casing location separated the

pressure side boundary layer. The shock system in the blade passage clearly gave rise to significant boundary layer and wake thickening. Referring to Figure 3.3, it was observed that the wake downstream of the rotor dissipated faster as a result of interaction with the stator half stage. The significant wake thickening observed in the rotor only case was not witnessed here.

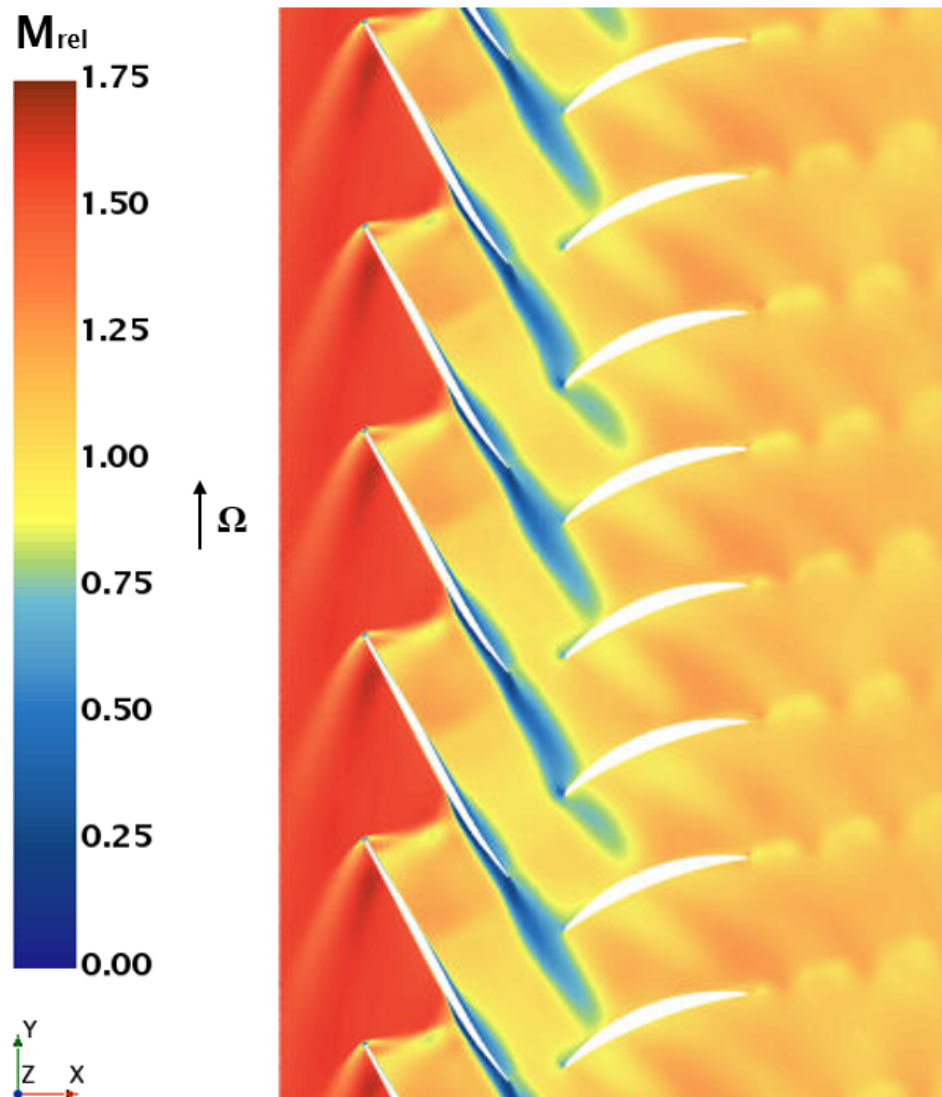


Figure 4.3. Instantaneous relative Mach number contours at 90% span of the Undamaged case

Figure 4.4 shows a front view of instantaneous relative Mach number contours at $(x/c)_{hub} = 0.27$ downstream of the hub leading edge. The spanwise variation of the shock location was evident. A low momentum region at the casing was induced by the impinging shock there.

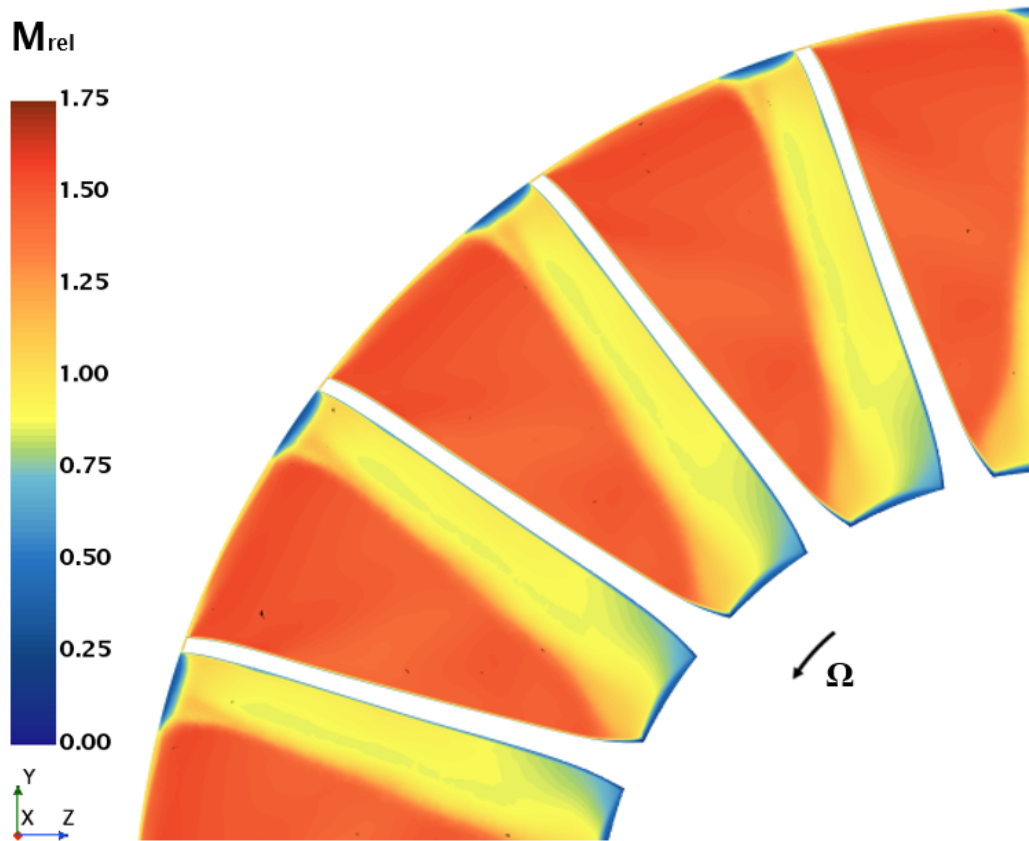


Figure 4.4. Instantaneous relative Mach number contours at $(x/c)_{hub} = 0.27$: Undamaged

The undamaged rotor has a tip clearance of 0.4% of span, and the tip clearance flow was visualized in Figure 4.5, using relative frame streamlines integrated through the time-averaged flow field. Double leakage above the adjacent blade was observed as the tip clearance streamlines migrate across the blade passage.

Figure 4.6 shows a top view of the same streamlines, with a 0.98 span surface contoured by time-averaged relative velocity. In both views, the interaction of the

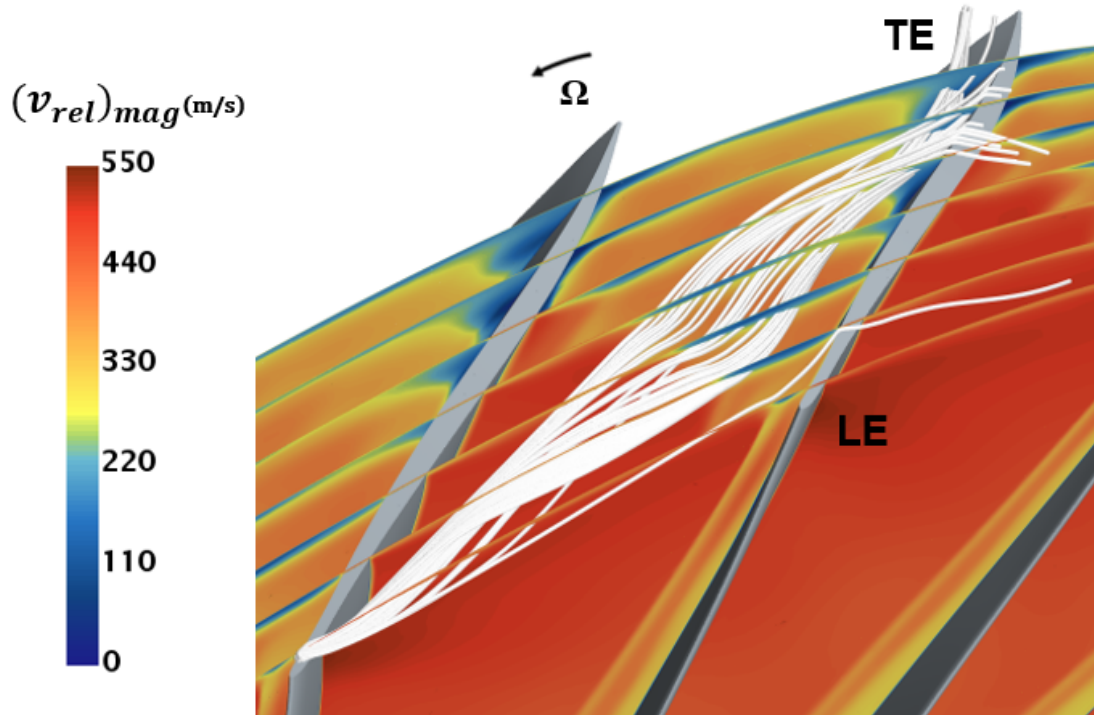


Figure 4.5. Tip clearance gap streamlines of Undamaged case with contours of relative velocity at several axial planes in the passage

tip vortex with the passage shock was observed, which was seen to redirect and decelerate the vortex. The redirected vortex structure developed as it migrated across the blade passage and impinged at the pressure side of the adjacent blade aft of midchord. These observations were consistent with the Rotor 37 studies of Yamada et al. [73].

The unsteady nature in the different quantities was observed in Figure 4.7. The spanwise distributions of the minimum and maximum value of the STR and SPR (normalized by the mid-span value of the Undamaged case) were plotted along with the time-averaged values. The STR profiles showed a linear decrease from the hub to about 80% span followed by an increase towards the shroud. This was consistent with STR profiles observed in CFD efforts for Rotor 37. The variation

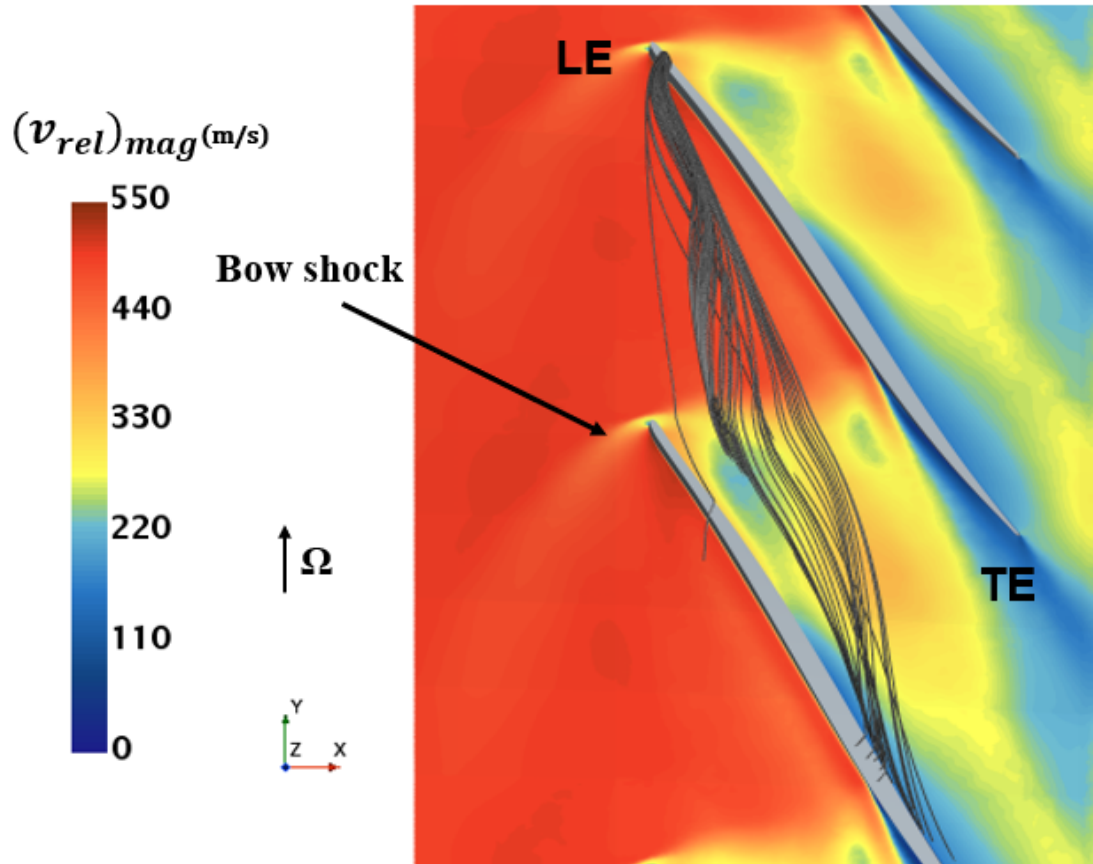


Figure 4.6. Streamlines in the tip clearance gap region with contours of relative velocity at 98% span

in the min-max values of the STR profile was observed to increase from near hub region (about 8%) to the tip region (about 14%). The SPR profiles showed a linear variation between 10% span and 90% span, before it precipitously fell to a much lower value at the shroud and tip clearance region. The variation in the min-max values of the SPR profile remained almost consistent from 10% span to the tip region (about 20%) with a maximum variation in the near hub region (about 30%).

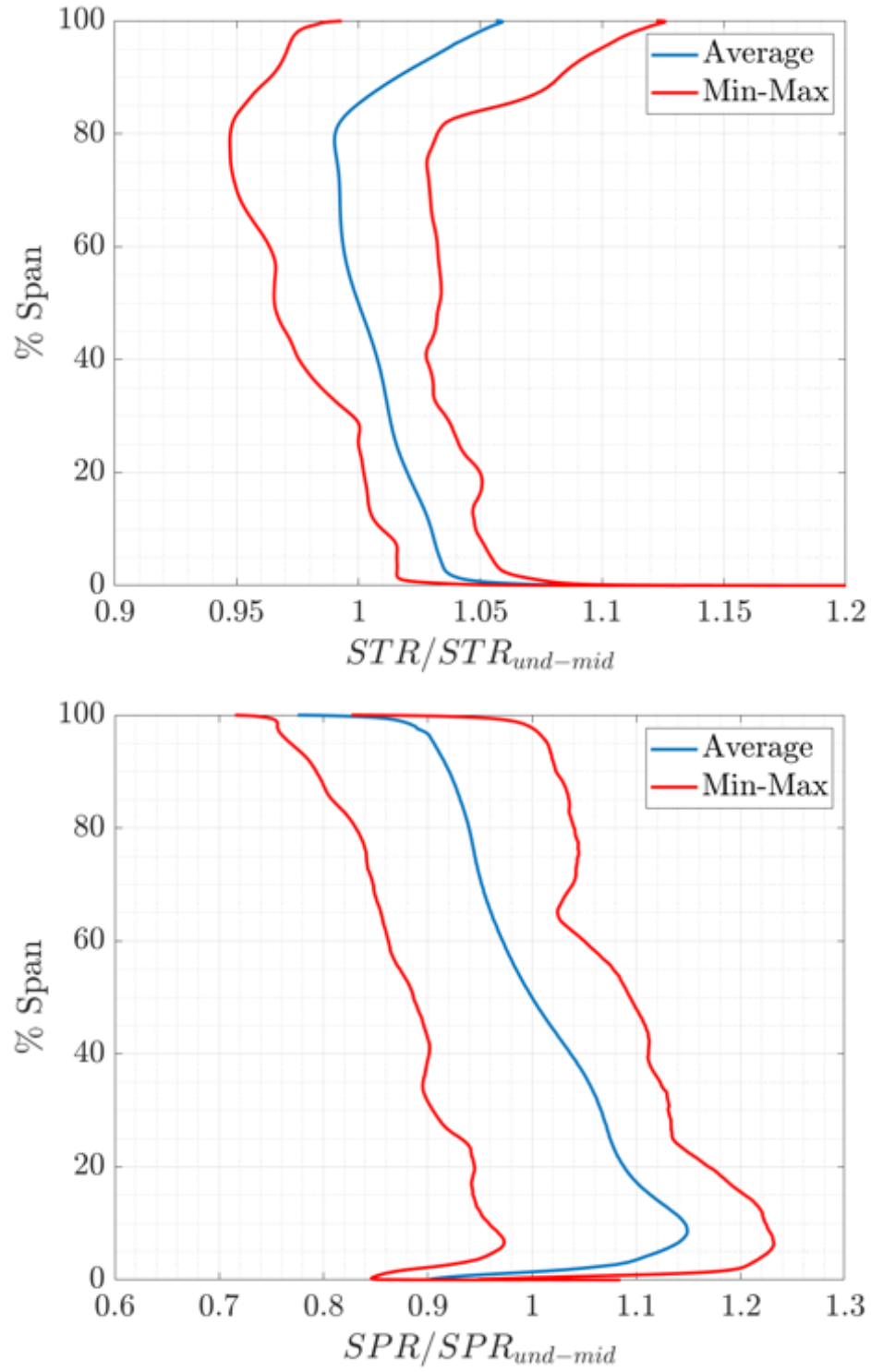


Figure 4.7. Spanwise distributions of time-averaged normalized STR (left) and normalized SPR (right) with min-max values for the Undamaged case

4.2.2 Damaged Configurations

A qualitative and quantitative comparison of the damaged configurations with the baseline Undamaged case is now presented. A narrative as seen in Chapter 3 Section 3.2.2 is pursued here. The Cragged configuration shown in Figure 2.5, is considered first. Figure 4.8 shows instantaneous relative Mach number contours at 90% span.

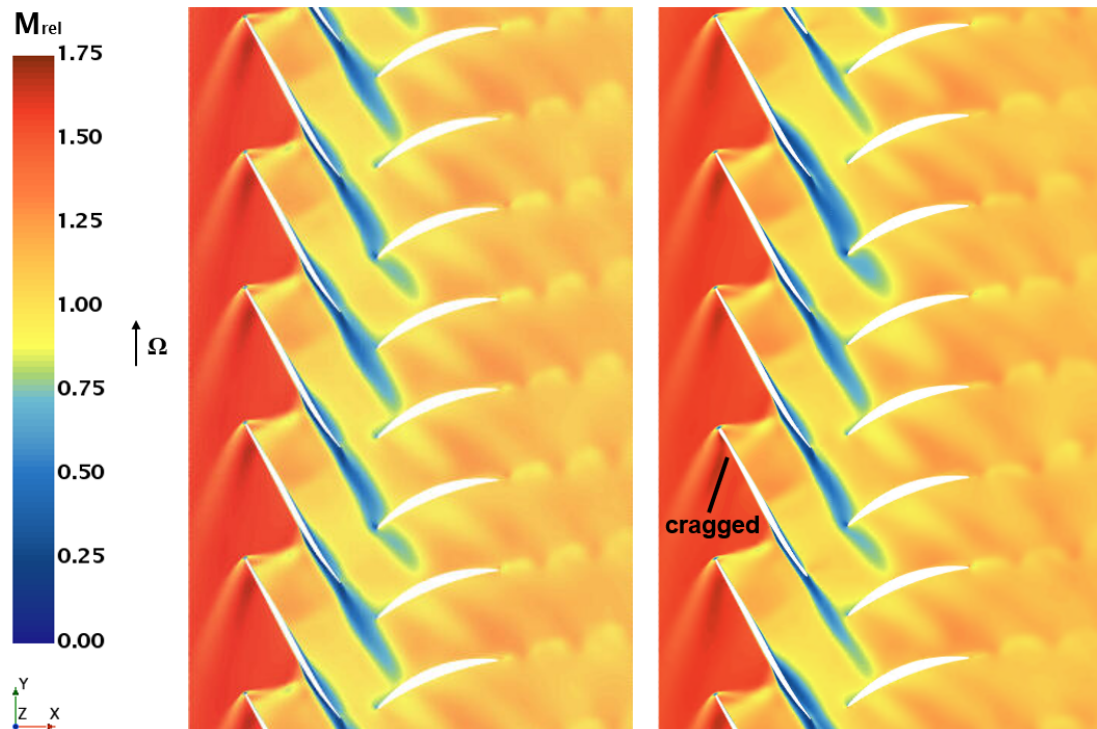


Figure 4.8. Instantaneous relative Mach number contours at 90% span; Undamaged (left), Cragged damage (right)

In this figure, and all subsequent blade-to-blade representations, the damaged blade is labeled. Comparing the two contour plots, modest differences were observed, and this was somewhat expected since damage to the rotor blade was confined to the leading edge along the span. Slight differences in shock and boundary layer

fields were observed, particularly in the passages on either side of the damaged blade. Downstream of the bow shock on the suction side, an increased acceleration of the flow was observed compared to the Undamaged case. Although relative Mach numbers were supersonic, the axial Mach number did not exceed 1, so upstream influence of the Cragged passage flow arose, leading to off-design physics in all four of the blade passages. The wake downstream of the Cragged blade was thinner and dissipated more quickly at this location.

Figure 4.9 shows instantaneous relative Mach number contours at 90% span for the Eroded damage case.

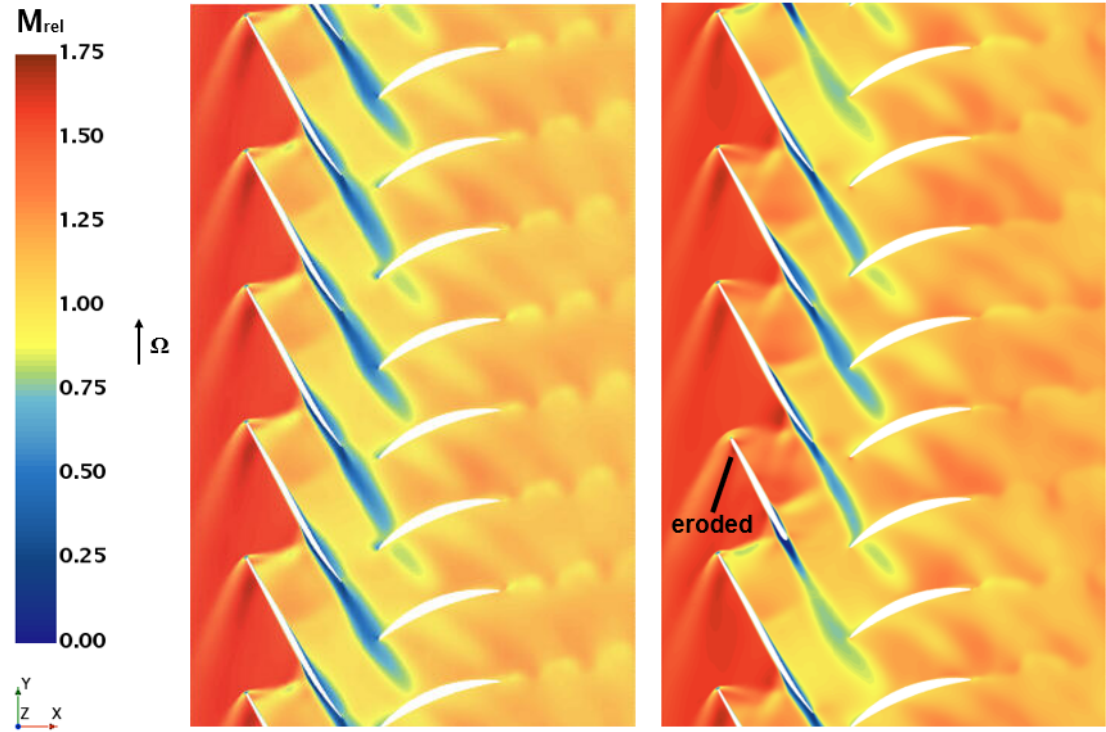


Figure 4.9. Instantaneous relative Mach number contours at 90% span; Undamaged (left), Eroded damage (right)

Here again, the impact of chord loss at the leading and trailing edges was clearly observed, and the resultant modifications to the flow field. The leading edge and its

attendant bow shock were further downstream, and a richer shock-expansion field arose. A stronger near-normal shock in the suction side passage adjacent to the damaged blade was evident. Also, the shock emanating from the blade's pressure surface was significantly stronger than in the Undamaged case, and impinged on the wake of the adjacent blade, further downstream than in the Undamaged case. Again, off-design physics was observed in all four of the blade passages. The wake behind the eroded blade was small and quickly dissipated at this outer span location. Referring to Figure 3.8, it was also observed that the wakes downstream of the rotor dissipated as a result of interaction with the stator half stage. This, in turn led to a less complex shock field downstream of the rotor compared to the rotor only case. A throttling effect due to wake thickening in the rotor only case where more downstream shocks were formed was observed to be less prominent or absent in this case.

Figure 4.10 shows instantaneous relative Mach number contours at 90% span for the Curled damage case. Similar to the rotor only case, the bow shock was much stronger since the leading edge curl acted as a much larger leading edge. A reverse flow region arose immediately downstream of the curl feature. There was also evidence of flow acceleration downstream of the bow shock, which was interpreted as a Prandtl-Meyer expansion fan. The flow field within the damaged blade pressure side passage was more complex, with multiple shock expansion interaction features arising. On the suction side, much more expansion was observed. The wakes of all four blade passages were significantly impacted.

In Figure 4.11, instantaneous relative stagnation pressure contours were plotted at $(x/c)_{hub} = .66$ downstream of the hub leading edge for the damaged and

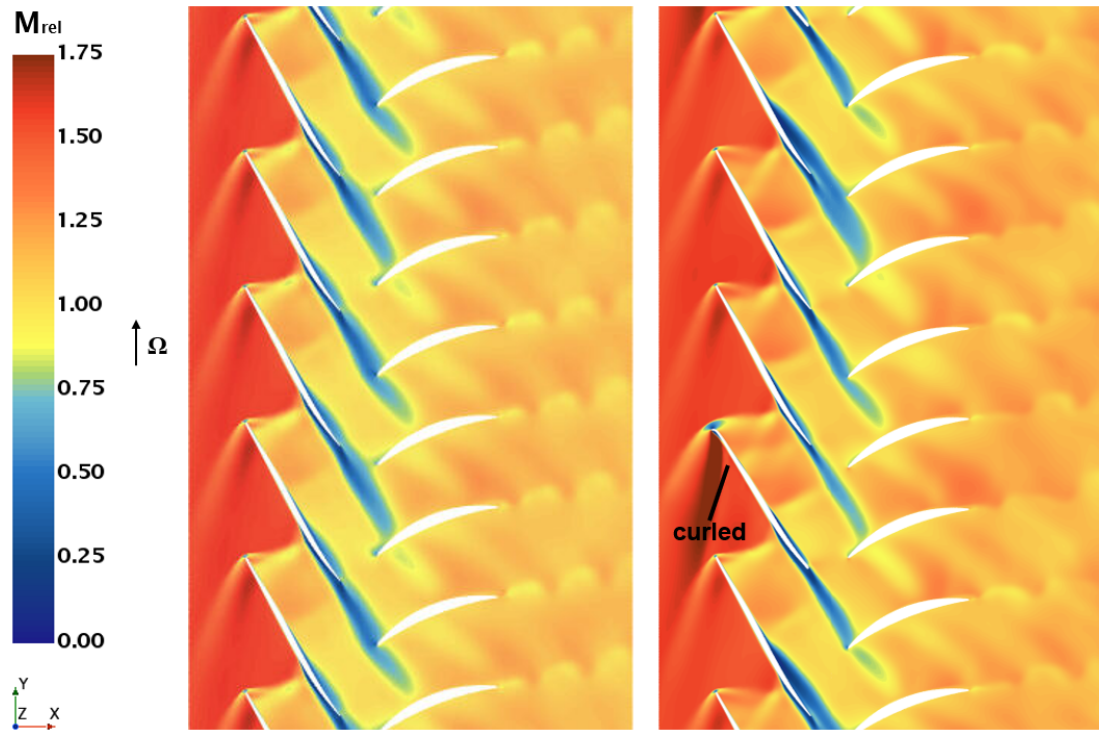


Figure 4.10. Instantaneous relative Mach number contours at 90% span; Undamaged (left), Curled damage (right)

undamaged cases. Observations similar to the rotor only case were made. In the undamaged blade passages, a high loss region was observed at the casing-suction surface corner associated with the shock-tip clearance vortex physics discussed above (Figure 4.5). A number of additional observations applied. Firstly, a low $p_{0,rel}$ region arose on the suction surface near midspan for all passages/cases. This high loss region was due to boundary layer interaction with the adjacent blade's bow shock. The size and shape of this loss region was significantly impacted by all three of the damaged blade geometries. The Curled tip and Eroded blades in particular gave rise to significantly larger regions of high loss adjacent to the blade surfaces in passages on either side of the damage.

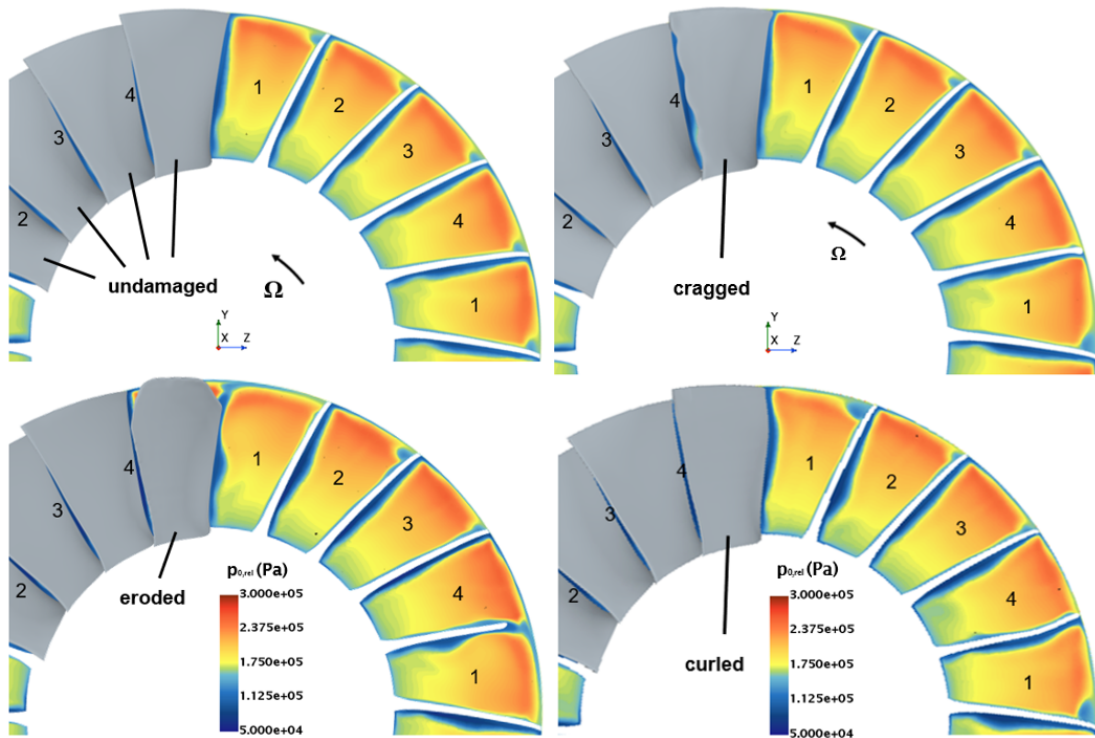


Figure 4.11. Instantaneous relative stagnation pressure contours at $(x/c)_{hub} = 0.66$; Undamaged (top-left), Eroded (bottom-left), Cragged (top-right), Curled (bottom-right)

Figure 4.12 shows the tip clearance flow for the Eroded and Curled cases visualized with the same viewing angle and seeding locations as Figure 4.5. Comparing the three streamline plots, they were generally similar, however some differences could be observed. In the Eroded case, the tip vortex remained more closely confined to the blade, not extending all the way to the pressure side of the adjacent blade. Unlike the Undamaged case, double leakage over the adjacent blade was not observed. In conjunction with Figure 4.11, there was evidence of the tip vortex developing along the shroud creating a broad region of low momentum fluid. In the Curled case, a significantly larger tip vortex was observed, with migration across the blade passage. Again, in conjunction with Figure 4.11, the attendant regions of

low momentum fluid near the shroud, closer to the pressure side of the adjacent blade were observed. There was minimal double leakage over the adjacent blade. The streamlines for the Cragged case were not included here, since the near-tip geometry was similar to the undamaged blade, and the streamlines were thereby quite similar.

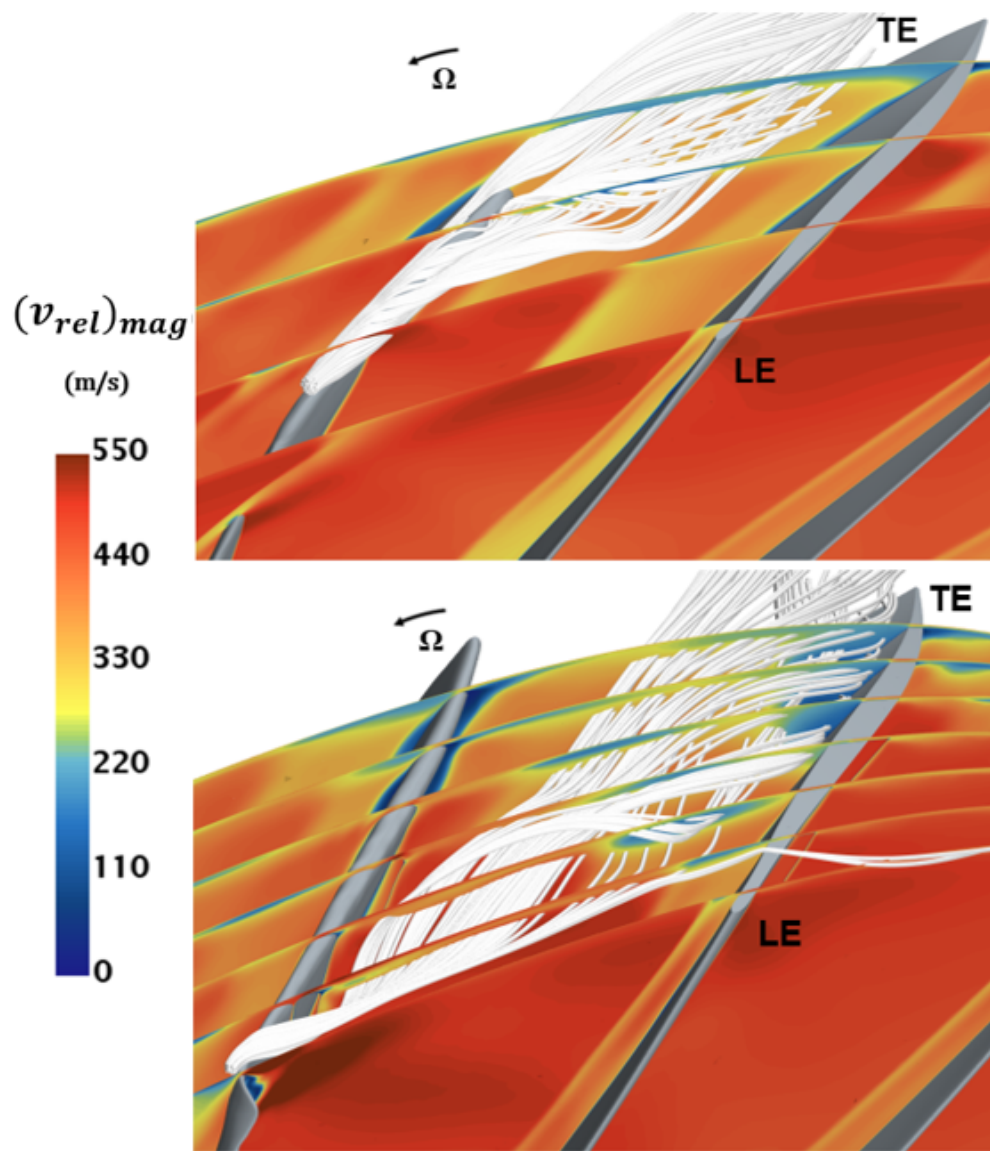


Figure 4.12. Tip clearance gap streamlines with contours of relative velocity at several axial planes in the passage: Eroded (top), Curled (bottom)

Stage performance parameters are summarized in Table 4.1. These were defined based on computational domain outlet and inlet boundary values. These parameters were normalized with the results for the Undamaged case. Specifically, enthalpy averaged stagnation pressure ratio (SPR), mass weighted stagnation temperature ratio (STR), and adiabatic efficiency (based on mass weighted enthalpies) are tabulated. As discussed in Section 2.4, specifying appropriate operating conditions for the damaged runs involved specifying a higher shaft speed and lower rotor 1 stagnation enthalpy rise, $\Delta h_{0,1}$, and these are listed as well. All three damaged rotors exhibited significant reductions in the stagnation pressure and temperatures ratios, and adiabatic efficiency. Consistent with the observations above, the Cragged rotor exhibited modest performance deterioration, followed by more significant reductions for the Curled blade, and yet more severe impact for the Eroded damage. This differed from the rotor only simulations as the Curled case performed better than Eroded case for the full stage simulations.

Table 4.1. Comparison of Overall Performance Parameters

| Case | Und. | Crag. | Curl. | Erod. |
|-----------------------------------|-------|-------|-------|-------|
| RPM/RPM_{und} | 1.000 | 1.001 | 1.003 | 1.004 |
| $\Delta h_{01}/\Delta h_{01,und}$ | 1.000 | 0.975 | 0.932 | 0.912 |
| SPR/SPR_{und} | 1.000 | 0.981 | 0.949 | 0.932 |
| STR/STR_{und} | 1.000 | 0.995 | 0.987 | 0.983 |
| $\eta_{tt}/\eta_{tt,und}$ | 1.000 | 0.991 | 0.973 | 0.966 |

Figure 4.13 shows the spanwise distribution of normalized adiabatic efficiency at an axial plane 0.34 stator axial chord downstream of the stator trailing edge plane. All profile data were normalized using the mid-span values of the Undamaged case. For all cases, the normalized adiabatic efficiency decreased across the span, from

approximately 1.05 near the hub to 0.9 at 80% span, then dropped precipitously to near 0.6 at the casing, this decrease arising due to increasing M_{rel} and shock strength with radius, tip clearance flow, and relative casing rotation.

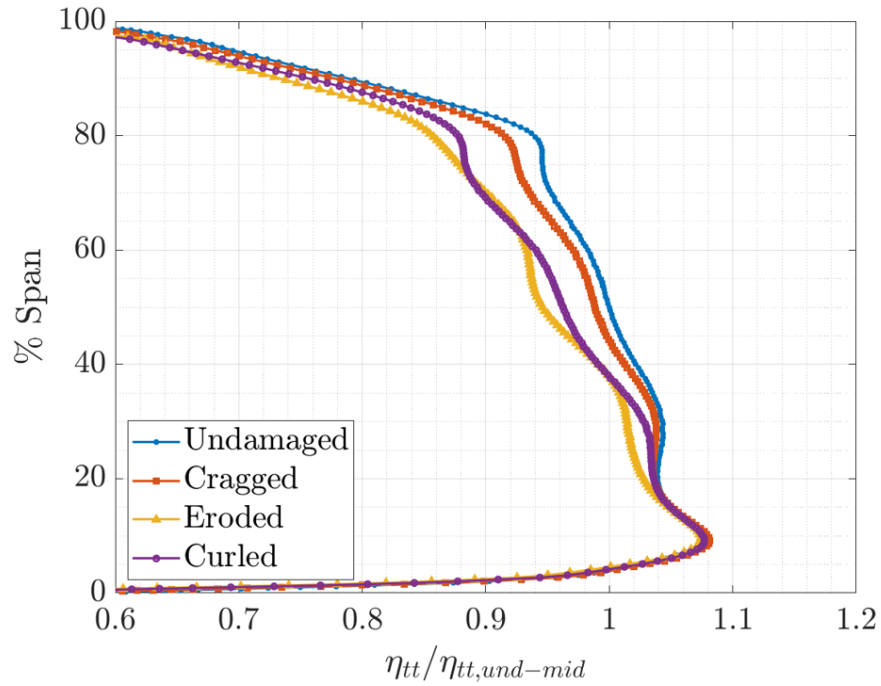


Figure 4.13. Spanwise distribution of normalized adiabatic efficiency at the stator outlet

Figures 4.14 and 4.15 show the spanwise distributions of mass-weighted STR and enthalpy-weighted SPR, also at an axial plane 0.34 stator axial chord downstream of the stator trailing edge plane. Figure 4.16 shows the spanwise profile of absolute flow angle at the rotor-stator interface. Flow angles were also referenced to the mid-span Undamaged case. A number of observations were forthcoming. As seen in Figure 4.14, all four cases exhibited decreased stage work and rotor turning with span across the inner 80% span, a general characteristic of the stage design. All three of the damaged blades gave rise to significant reductions in STR and attendant rotor under-turning across most of the span. This re-distributive unloading was

observed for all stages despite the damage itself being restricted to outer spans for the Curled and Eroded blades. As seen in Figure 4.15, the stagnation pressure rise decreased correspondingly with the increasing severity of the damage morphology.

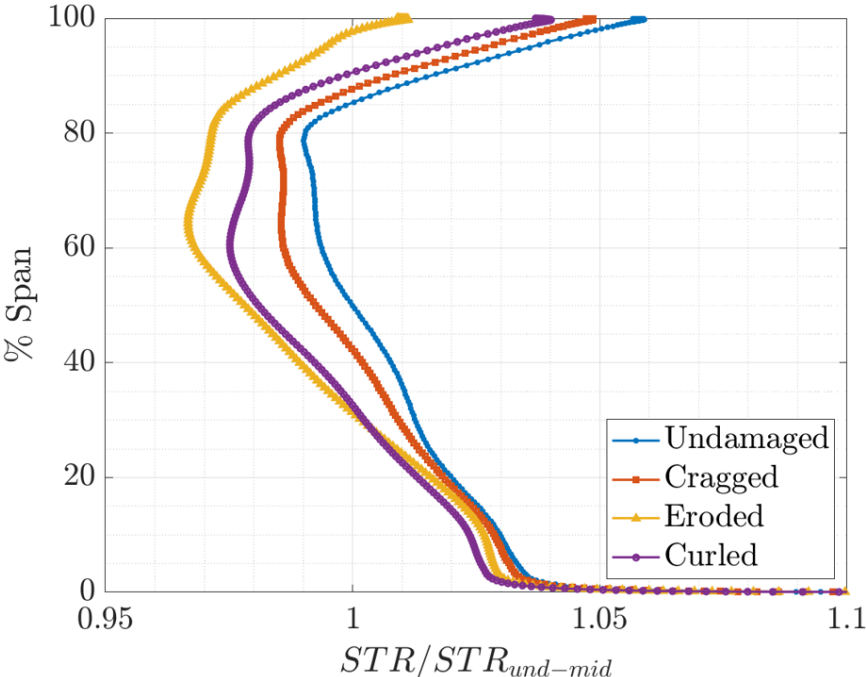


Figure 4.14. Spanwise distribution of normalized stagnation temperature ratio at the stator outlet

The damaged stage performance profiles showed generally consistent spanwise trends with the undamaged stage, since the qualitative physics of the damaged passage flow field remain largely the same (boundary/operating conditions, wave fields, secondary flows), and only one blade of every four was damaged in this study. However, there was less work done and increased losses across the entire span for all three damage modes. Damage severity was again rank ordered from Cragged, which showed only modest deterioration of the four parameters considered, across the span, followed by Curled and Eroded, which exhibited highly compromised performance deterioration.

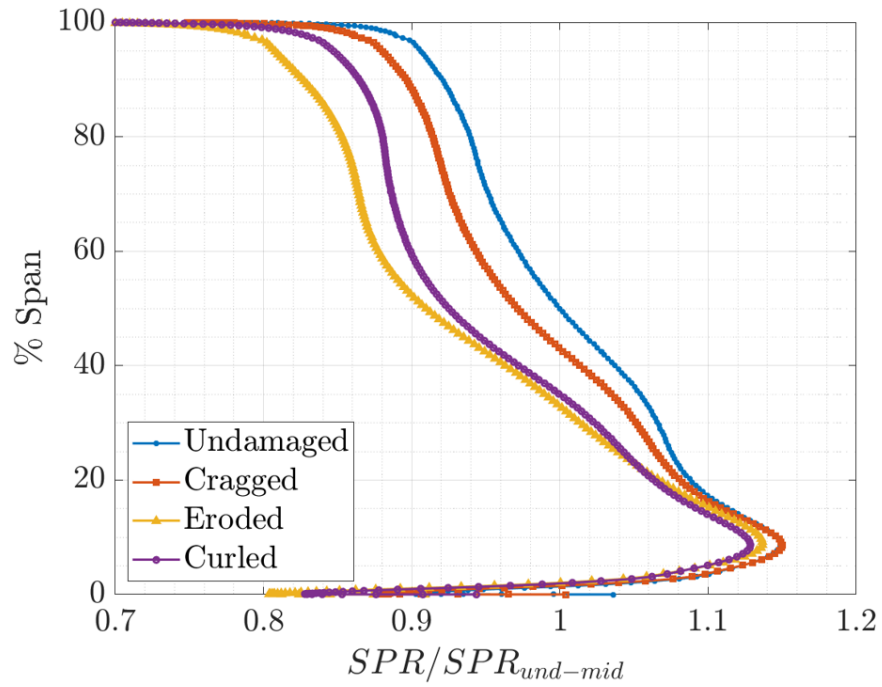


Figure 4.15. Spanwise distribution of normalized stagnation pressure ratio at the stator outlet

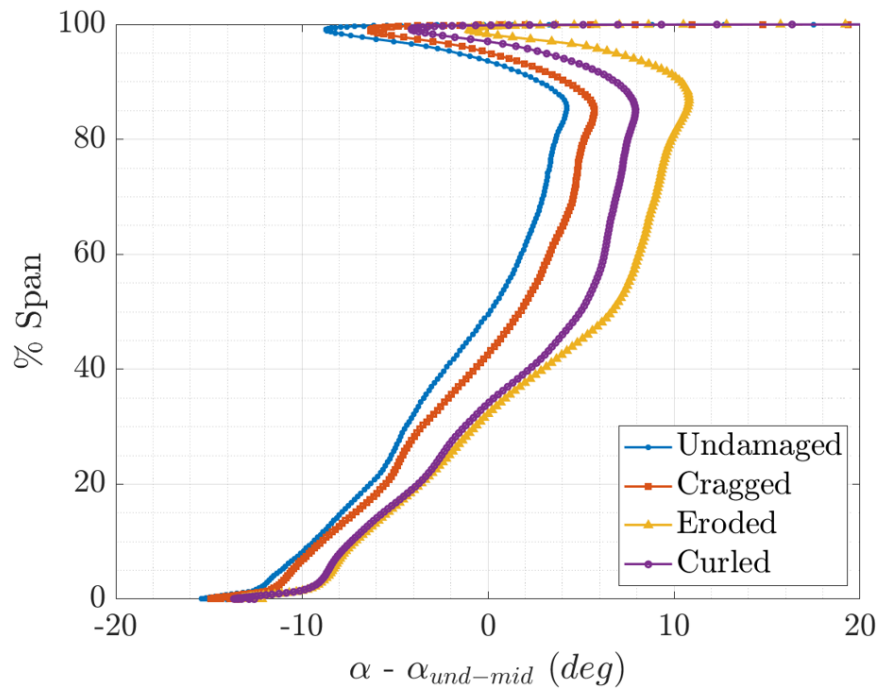


Figure 4.16. Spanwise distribution of normalized absolute flow angle at the rotor-stator interface

4.2.3 Impact on SFC

The methodology to assess the impact on SFC discussed in Chapter 3, Section 3.2.3 is invoked here. Since the stator half stage does not perform any work, it was completely appropriate to do so.

In Figure 4.17, predicted values of SFC, normalized by the undamaged model value, were plotted for the four configurations. As the nature of the damage became more severe, the normalized SFC increased as expected, to a maximum of just over a 1.4% increase for the Eroded damaged stage. This was accompanied by an overall reduction in CPR (also normalized) of 6.8% as plotted in Figure 4.18.

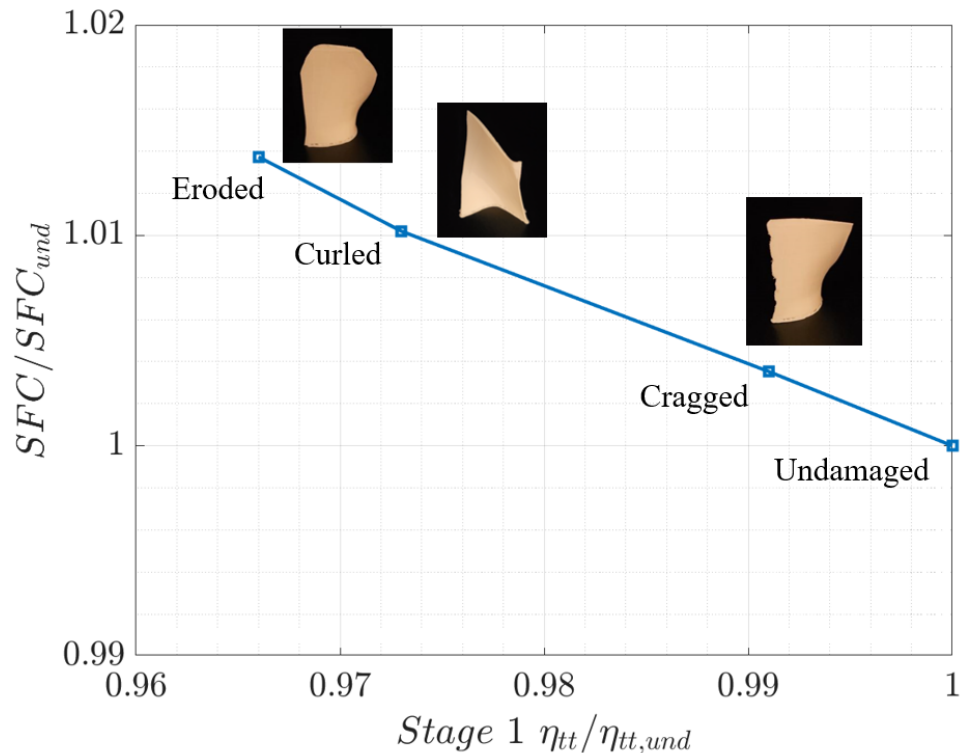


Figure 4.17. Normalized SFC vs Normalized Stage 1 Adiabatic Efficiency

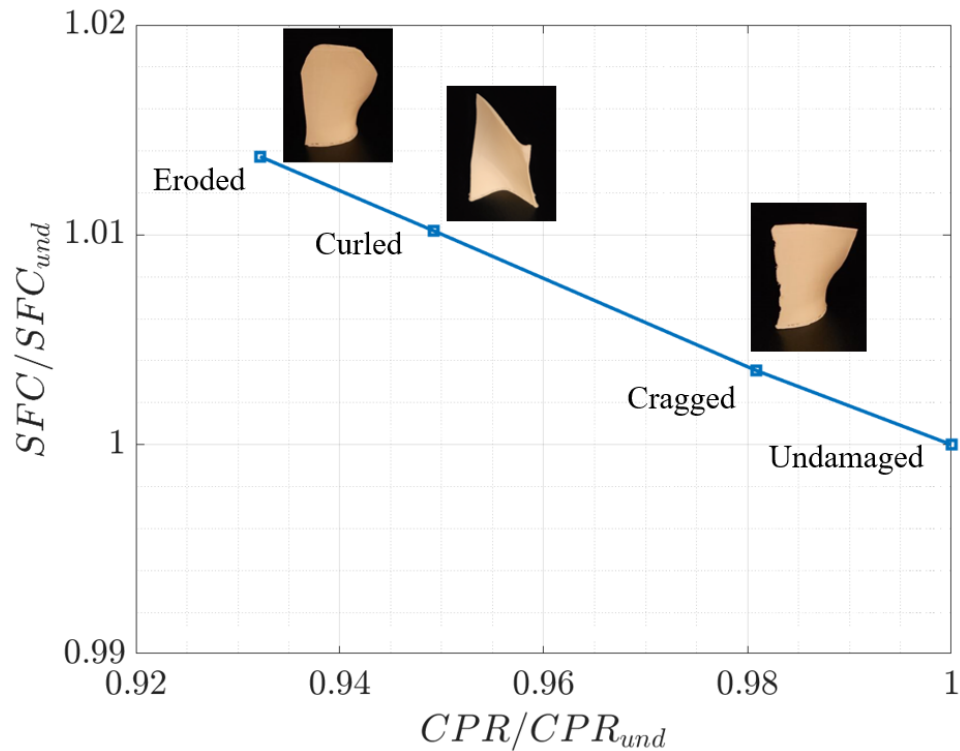


Figure 4.18. Normalized SFC vs Normalized Compressor Pressure Ratio

4.3 Results Comparison - Full Stage and Half Stage calculations

A comparison was made between the unsteady full stage simulations [74] and the steady state rotor only simulations [75]. First, a side-by-side comparison of the flow fields (in terms of relative Mach number contours) was made. Figure 4.19 shows the comparison between the contours at 90% span for the Eroded case. At the same axial location, significant differences between the shock and wake field were observed. In the steady case, the wake behind the blade kept growing, causing the flow between the blade passages to choke. This resulted in the formation of

stronger normal shocks downstream of the main passage shock. In the unsteady case, due to the rotor-stator interaction, the wake growth was limited and the shock strength in the passage flow was diminished.

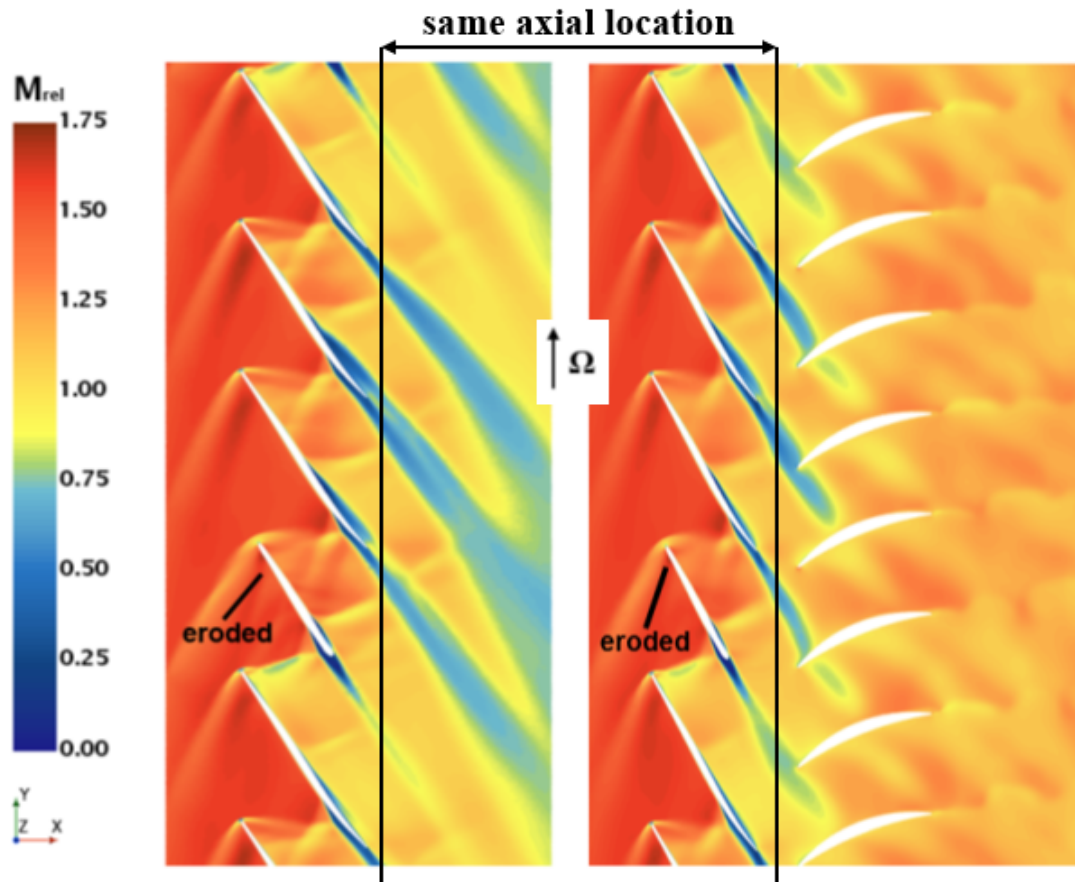


Figure 4.19. Comparison of relative Mach number contours at 90% span for the Eroded case: steady rotor only (left), unsteady full stage (right)

Figure 4.20 shows the comparison between the contours at 90% span for the Curled case. Similar observations comparable to the Eroded case were made. In the steady case, there were multiple downstream shocks as a result of the choking of the passage flow due to wake thickening. The differences in the wave field were observed to be markedly starker in the Curled case, where the complexity of the

flow field was markedly lower for the unsteady simulation.

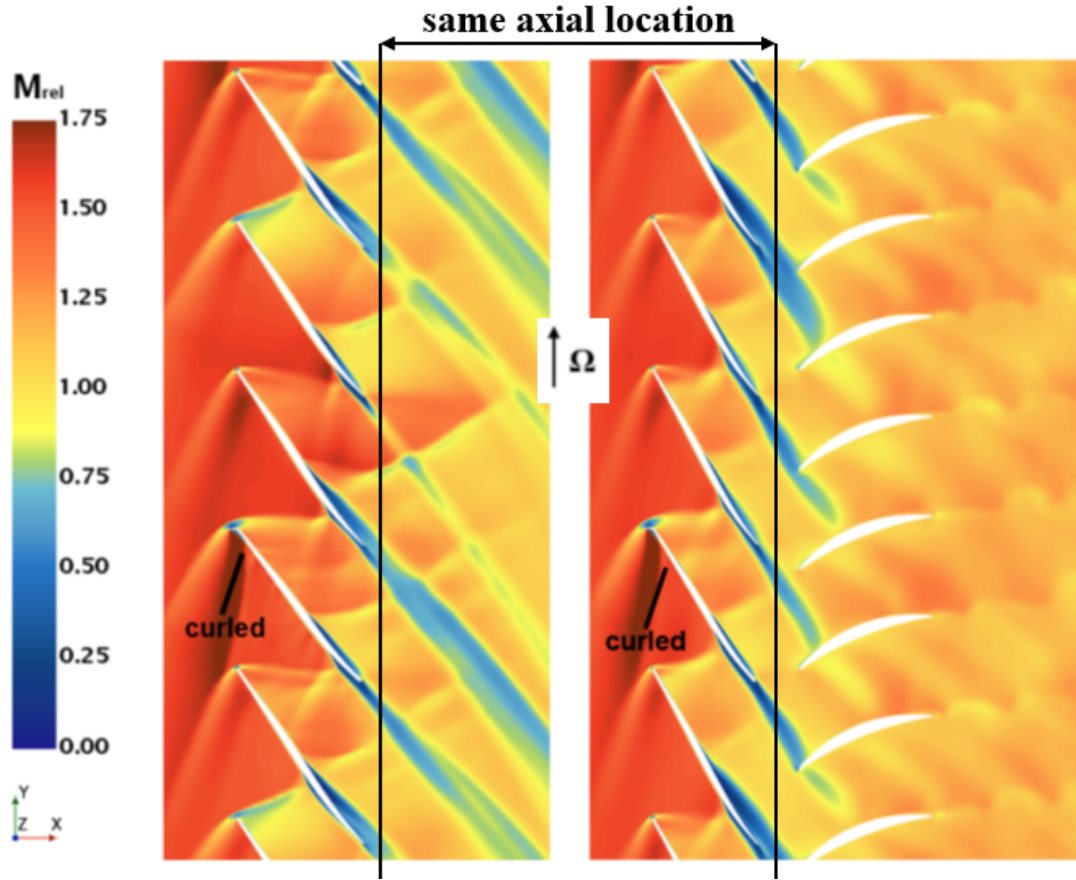


Figure 4.20. Comparison of relative Mach number contours at 90% span for the Curled case: steady rotor only (left), unsteady full stage (right)

Denton [76] qualitatively described some of the loss mechanisms in turbomachinery and related losses to mechanism of entropy generation. Entropy creation within shocks is due to heat conduction and high viscous normal stresses within the shock wave. Wakes generate additional entropy due to mixing. Koch and Smith [77] also investigated loss mechanisms in axial compressors and concluded that shocks were one of the four major sources of efficiency loss. The presence of additional (or even stronger) shocks and larger wakes were a significant source of entropy and hence performance loss as evidenced in the rotor only simulations.

To enable a direct comparison, performance parameters extracted at the location of the rotor-stator interface were used. The same plane was imported into the rotor only simulations and the extracted parameters are summarized. Figures 4.21 and 4.22 show the variation of normalized STR and normalized SPR respectively for the different cases. As expected, there was no significant difference between steady and unsteady runs for the Undamaged and Cragged cases. There was no significant difference in the wave field at this axial location for these two cases.

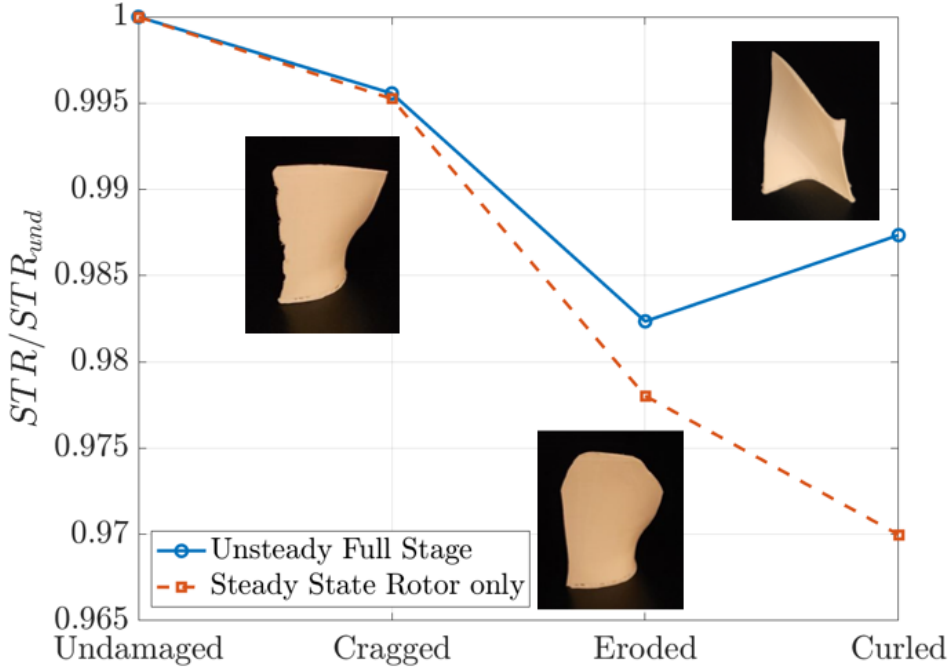


Figure 4.21. Normalized STR at the rotor-stator interface for each case

For the Eroded case, the unsteady calculation predicted the normalized STR and normalized SPR to be 0.46% and 1.62% higher respectively than the steady calculation. This was attributed to the reduced shock strength and less complex wave field in the blade passage, resulting in lower entropy generation and hence leading to better performance. Similarly, for the Curled case, the unsteady calculation

predicted the normalized STR and normalized SPR to be 1.75% and 9.51% higher respectively than the steady calculation. This was again, attributed to the lower entropy losses as a result of the much improved wave field in the blade passage. The improvement in the wave field and hence the performance parameters for the Curled case was observed to be very significant. This resulted in the unsteady simulations predicting that the Eroded case was the worst performing damage configuration.

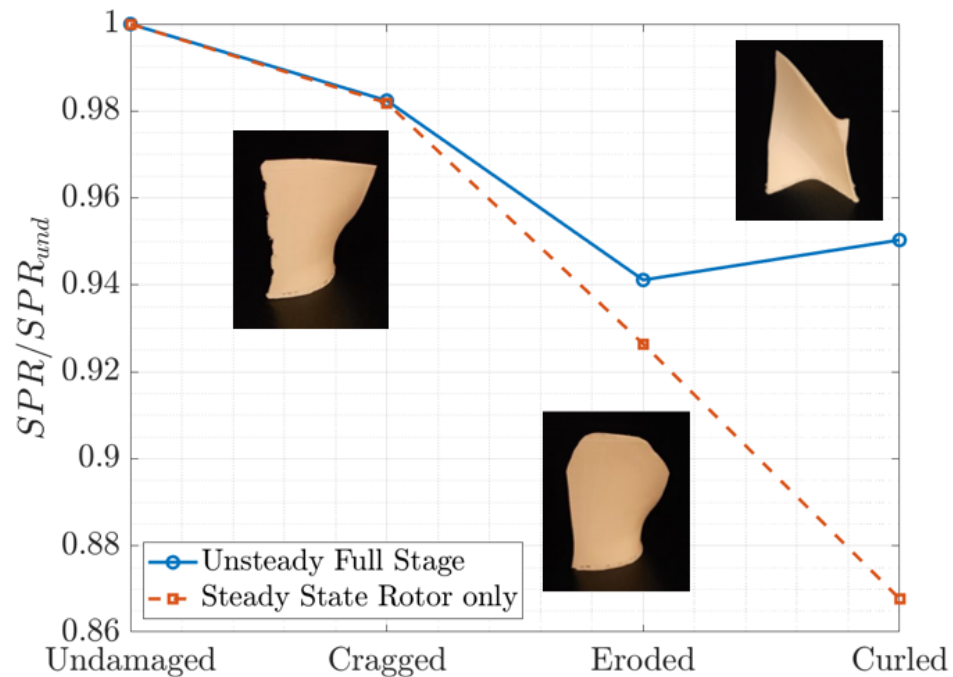


Figure 4.22. Normalized SPR at the rotor-stator interface for each case

Belamri et al. [78] performed CFD analyses of a 15-stage axial compressor prototype and concluded that transient simulations predicted performance parameters more accurately than steady-state simulations, especially for off-design conditions. Burberi et al. [79] performed a comparison between steady and transient simulations for an 11-stage axial compressor. They observed that the transient simulations

predicted the design point parameters and the onset of stall more accurately than the steady simulations. Yang and Boulanger [41] performed an unsteady analysis of a full annulus axial fan and verified the validity and need for unsteady CFD models compared to steady models for turbomachinery applications. The findings in this dissertation further confirmed that unsteady full stage simulations were necessary for better predictions of performance degradation as the inherent averaging in steady simulations could inaccurately evaluate the role of flow interactions at the rotor-stator interface and hence impact the overall performance parameters.

Chapter 5 |

Erosion Modeling Due to Particle Ingestion

The simulations in Chapters 3 and 4 presented results of pre-test predictions for blades that were already damaged. This chapter aims to directly assess the impact of particle ingestion using Lagrangian multiphase simulations. Specifically, this chapter discusses the study of erosion modeling performed in STAR-CCM+ [59]. The methodology employed in this erosion prediction research is described. A well-documented data set for erosion by an air-jet containing sand impinging on a stainless steel sample was selected as a method validation case. This is due to the lack of data sets containing quantitative erosion measurements for turbomachinery applications. The results of the validation case are presented and conclusions are discussed. Qualitative estimates of erosion of NASA Rotor 37 blade surface due to sand ingestion are then presented and discussed. This is followed by an illustration of the erosion coupled deformation methodology with a blade section of Rotor 37 spanning from 40% span to 60% span.

5.1 Lagrangian Multiphase Simulation

The Lagrangian multiphase solver in STAR-CCM+ [59] incorporates particle-boundary interaction and erosion models in a time accurate context [59]. In this chapter, this combined Eulerian-Lagrangian approach was used to make qualitative estimates of erosion at the rotor blade surface of NASA Rotor 37. A method validation based on the results of Nguyen et al. [48] was performed to lend credibility to these results. First, a discussion of the physics model and numerical methodology used for erosion is presented, followed by the method validation study. Next, qualitative predictions of erosion patterns of the NASA Rotor 37 are presented, followed finally by an illustration of the erosion coupled surface deformation of Rotor 37 blade section.

5.2 Description of the Method Validation Case

The method validation is described first to lend better clarity to the methodology employed in this chapter. As there are no published data-sets available for erosion studies in turbomachinery beyond the qualitative estimates of erosion patterns and regions of maximum erosion, a validation case was chosen in which the data are well documented and provides quantitative estimates for various erosion characteristics. Nguyen et al. [48] constructed an erosion testing rig for sand-air erosion with incident velocities up to Mach 3. They performed a study on an SUS304 stainless steel sample in terms of the impact angle and testing time. They obtained results in terms of erosion rate, surface profile evolution and surface micro-structure characteristics.

For each sample tested, at a range of incident velocities, maximum erosion was observed at an incidence angle of 40°. This was attributed to the fact that stainless steel has a face centered cubic structure with a slip plane at an angle of 40° to 45° increasing the likelihood of erosion. All the erosion testing was performed with an air-jet whose inlet velocity was 200m/s. The fluid Reynolds number based on the nozzle diameter and air velocity was 110,000 and was in the same order of magnitude as the Rotor 37 case. This data-set had the closest air velocity compared to the inlet of NASA Rotor 37. The sample material was SUS304 stainless steel which has similar strength and hardness to 12 chrome steel in the AISI 400 series (the most common material used for axial compressor blading [80]). SUS304 has a density of 7929kg/m³ and Vicker Hardness Number of 196. The erodent particle is sand that contains mainly aluminum oxide (Al_2O_3) and silica (SiO_2) with an average size of 90 mesh. A 90 mesh size corresponds to the particle size distribution shown in Table 5.1. The sand has a density of 2400kg/m³ and a hardness of 9Moh. Sand flow rate of 1g/s was used for this study.

Table 5.1. Particle size distribution for 90 mesh sand

| | | | | | | |
|-------------------|-------|-------|-------|-------|-------|-------|
| Radius (mm) | 0.074 | 0.088 | 0.105 | 0.125 | 0.149 | 0.177 |
| Mass Fraction (%) | 1.25 | 2.95 | 9.25 | 23.35 | 59 | 4.2 |

The 90° impact angle case was chosen for this study as the surface profile measurements and the time evolution history of the surface were only available for this data point. Figure 5.1 shows the surface profile measurement for the case of the 90° impact angle after 120s of erosion.

The measured time evolution history of the surface profile for 90° impact angle

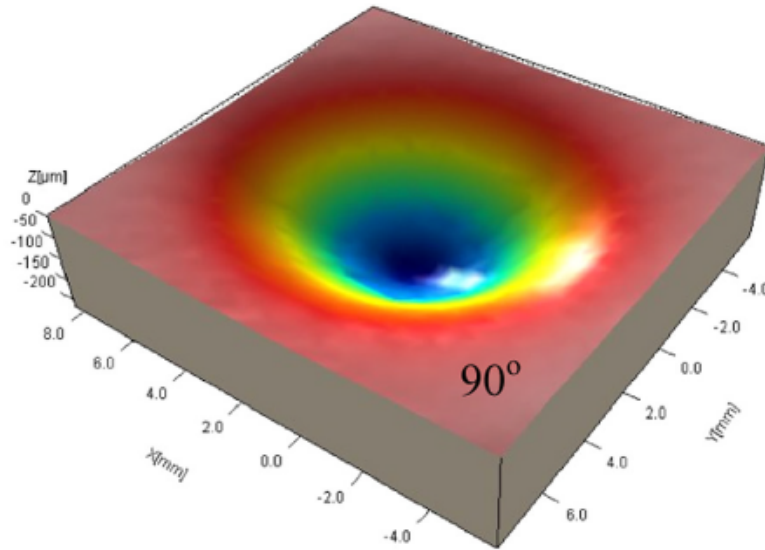


Figure 5.1. 3D surface profilometer measurement of the sample for 90° impact angle [48]

case is shown in Figure 5.2. It was noted that the erosion rate peaked at 120s and then decreased. This authors attributed this to strain hardening effects of the sample material after a certain period of impaction by the erodent material. Table 5.2 provides the time history of the maximum depth for this case along with the confidence intervals of the surface measurements involved.

Table 5.2. Maximum depth of cut for sample at 90° impact angle [48]

| Time (s) | 30 | 60 | 120 | 180 | 240 | 300 |
|--------------------------------|-----------|-----------|------------|------------|------------|------------|
| Depth of cut (μm) | 34 ± 5 | 76 ± 3 | 221 ± 4 | 238 ± 5 | 276 ± 6 | 352 ± 5 |

The technical approach to implement the erosion prediction of this validation case is discussed next. The details of the geometry and computational domain are discussed in Section 5.3.1.

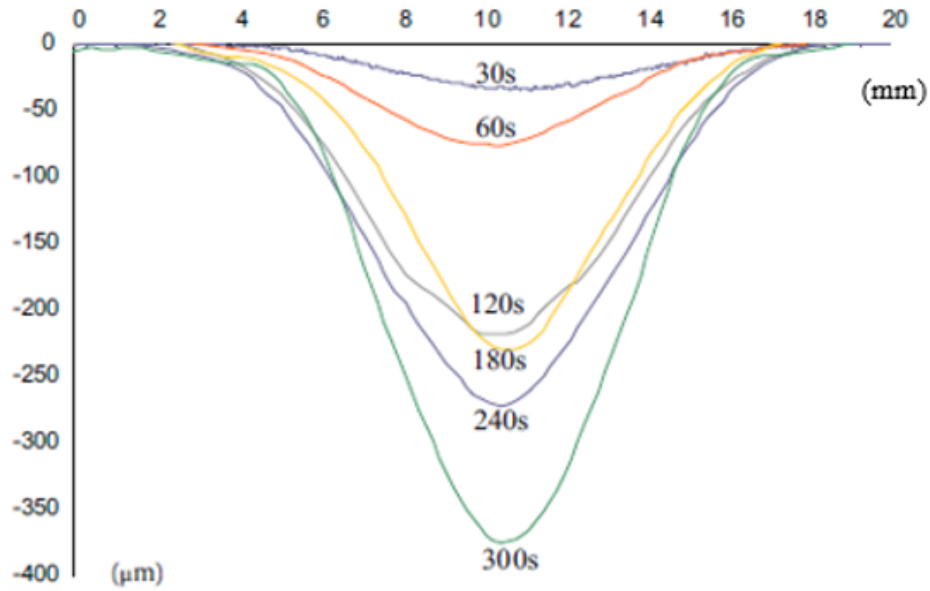


Figure 5.2. Surface profile evolution history of the sample for 90° impact angle [48]

5.3 Technical Approach

A combined Eulerian-Lagrangian approach was used for these studies. Specifically, the fluid phase was solved using the Eulerian approach and the particle (solid) phase was solved using the Lagrangian approach in STAR-CCM+ [59].

This work aimed to improve upon the methodology pursued by Lopez et al. [50], Duarte and de Souza [53] and Agrawal et al. [52]. In these three works, they pursued different versions of a combined Eulerian-Lagrangian simulation of particle ingestion into the fluid flow, followed by a time-averaged erosion calculation. The computed erosion field was coupled with a moving mesh deformation algorithm in the respective studies to produce deformed geometries after pre-set time intervals. This was done to take into account the multiple time scale nature of the erosion process.

In this study, firstly, the fluid flow (continuous phase) was solved using an unsteady RANS approach, while keeping the Lagrangian solver inactive. Once the fluid flow had achieved statistical stationarity, the particles (dispersed phase) were injected into the domain via the inlet after turning on the Lagrangian solver. The time-scales involved in erosion phenomena vary greatly in terms of order of magnitude. In this unsteady phenomenon, the continuous phase achieves statistical stationarity orders of magnitude sooner than the dispersed phase and its impact on the boundaries. The fluid phase may become statistically stationary in a matter of milli-seconds while the deformation due to erosion will only be significant at a much later time. This required special treatment where multiple scales of time were considered. Hence, the erosion field was calculated, and a time-scaling factor was utilized in order to save computational time and expense. In order to take into account, the stochastic effect due to Lagrangian nature of the particle paths, several realizations of the simulation were run. An ensemble average of the time-averaged erosion deformation was computed and was used to create the deformed geometry at different erosion steps after considering the time-scaling factor for erosion. This averaged surface profile was smoothed using a smoothing algorithm in MATLAB and was used to create a new deformed geometry in SolidWorks [57], followed by its re-integration in STAR-CCM+ [59]. Using this deformed geometry, the methodology was repeated until the desired time of erosion was achieved. The algorithm employed is illustrated in the flow-chart shown in Figure 5.3. Δt was the time-step used to solve the fluid phase and the dispersed phase until statistical stationarity was achieved in both the fluid flow and the time-averaged erosion flux. The computed erosion displacement was then multiplied by a time scale factor τ to

obtain the erosion deformation. The steps were repeated until the end-time T_{end} of the erosion study. For the validation case, Δt was 0.00001s. The time scale factor τ was either 30 or 60 since the erosion is accelerated to times of 30s, 60s and subsequently 120s in this study. The end time T_{end} was 120s for the erosion study.

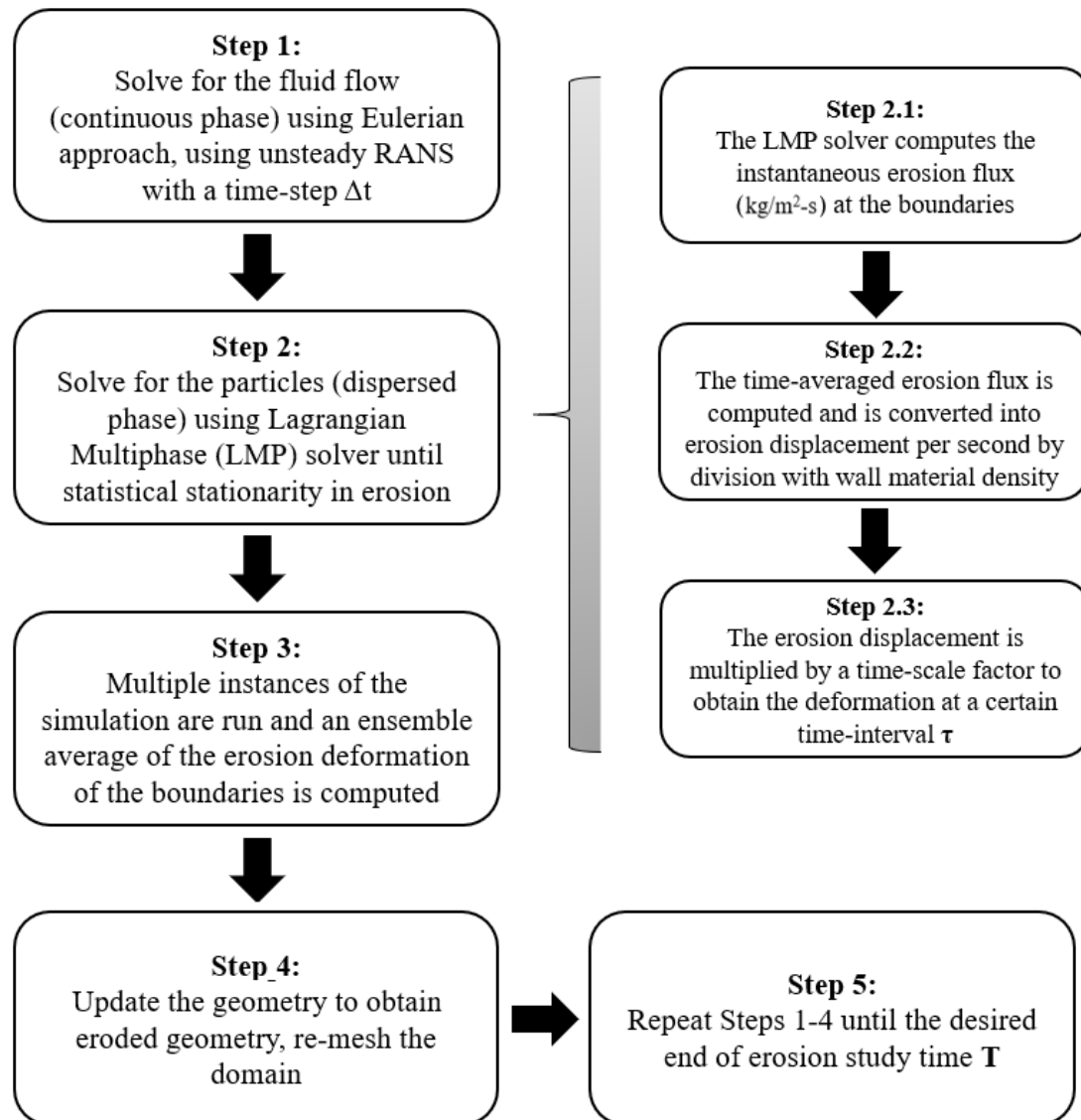


Figure 5.3. Flowchart of the methodology employed for the erosion studies

5.3.1 Computational Domain and Boundary Conditions

The CFD domain for simulating the experiment by Nguyen et al. [48] is shown in Figure 5.4. The nozzle had a diameter of 8mm and extended for a length of 43.50mm. The nozzle exit had a stand-off distance of 12.40mm from the sample surface. The sample had the dimensions of 25mm x 25mm x 5mm. The nozzle inlet was set as a velocity inlet with a uniform velocity of 200m/s. The nozzle bore was considered to be an adiabatic smooth wall. The sample surface was also set as an adiabatic smooth wall with the impact erosion model activated. The rest of the surfaces were set as an outlet boundary.

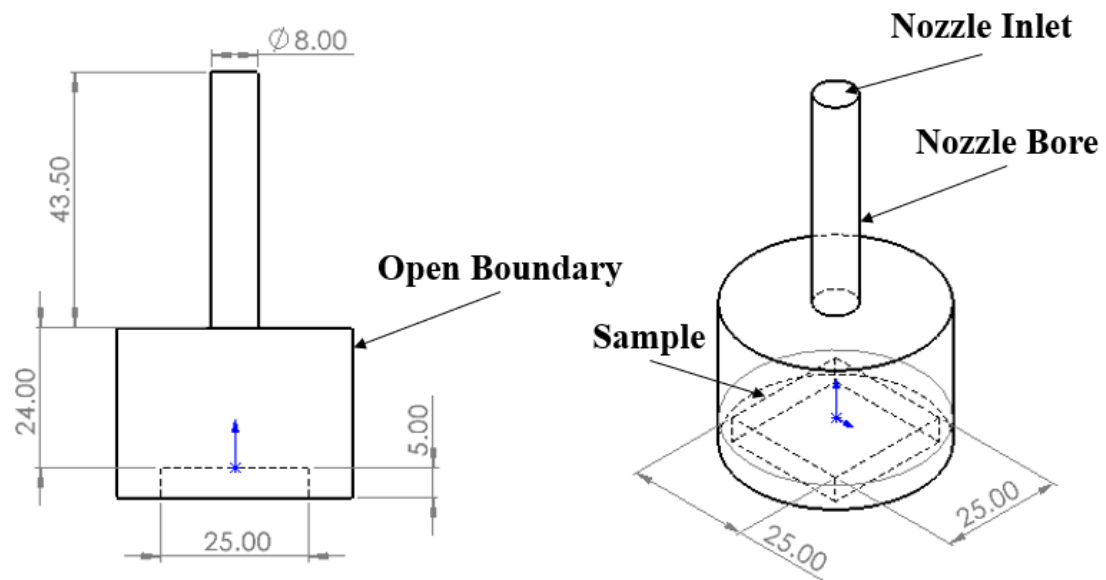


Figure 5.4. CFD domain for the method validation case

5.3.2 Meshing Strategy

The automated mesher in STAR-CCM+ [59] was used to create an unstructured polyhedral mesh with prism layers along the nozzle bore and the sample surface. Further refinement of the mesh was performed along the region of the turbulent air-jet. The mesh was also refined along the surface of the sample. The refinements in the region of interest enabled the optimization of the mesh size, which in turn reduced the computational cost. In the regions far from the turbulent jet or the sample, the mesh was set to be coarse as there were no sharp gradients in the flow. Views of the mesh used for the method validation case are shown in Figure 5.5.

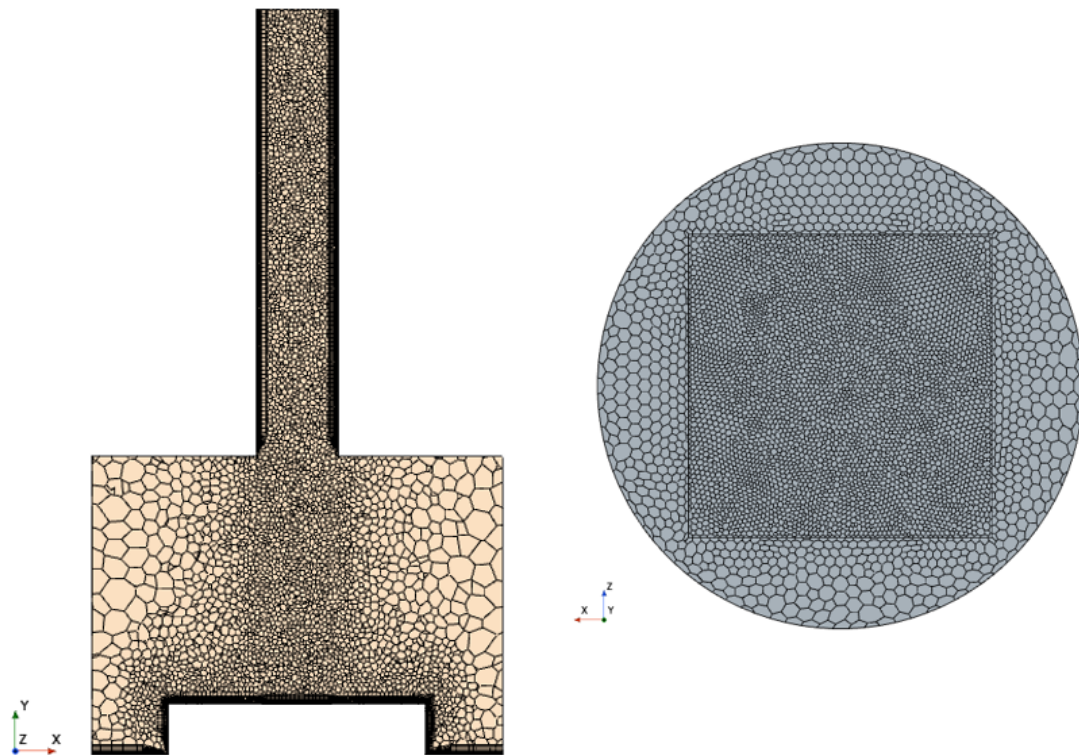


Figure 5.5. CFD domain for the method validation case

5.3.3 Eulerian Modeling of Fluid Phase

The fluid phase was modeled using an Eulerian approach. The RANS solver of STAR-CCM+ [59] was used. All the simulation runs were performed with the coupled solver with second order discretization in space and time. They were run as using the implicit unsteady solver with a time-step of 0.00001s. The choice of time-step is explained in the next section. Perfect gas air was used as the continuous phase. The Menter- $k-\omega$ SST turbulence model [63] was used.

5.3.4 Lagrangian Modeling of Particle Phase

The dispersed phase was modeled using a Lagrangian approach. In STAR-CCM+ [59], this approach involves the description of particles in terms of elements known as parcels. A parcel refers to a collection of particles being tracked by the solver. A parcel is a discretization of the population of the dispersed phase in the same way as cells are a discretization of the continuous phase. The distribution of particles within the parcel are not provided by the solver. The state of each parcel after injection is tracked in terms of parcel centroid location and parcel velocity using a first order tracking integration scheme with respect to time. The maximum particle velocity was about 200m/s and will be discussed in Section 5.4.1. The time-step of 0.00001s was chosen such that the particle traversed a maximum of 2mm at every time-step enabling a compromise between accurate tracking of its particle path and making the computation very expensive. At every time-step of an unsteady simulation, the solver recorded the centroid location and the velocity of the parcel. Figure 5.6 illustrates an example of a parcel in STAR-CCM+ [59] as well as its

interaction with the wall.

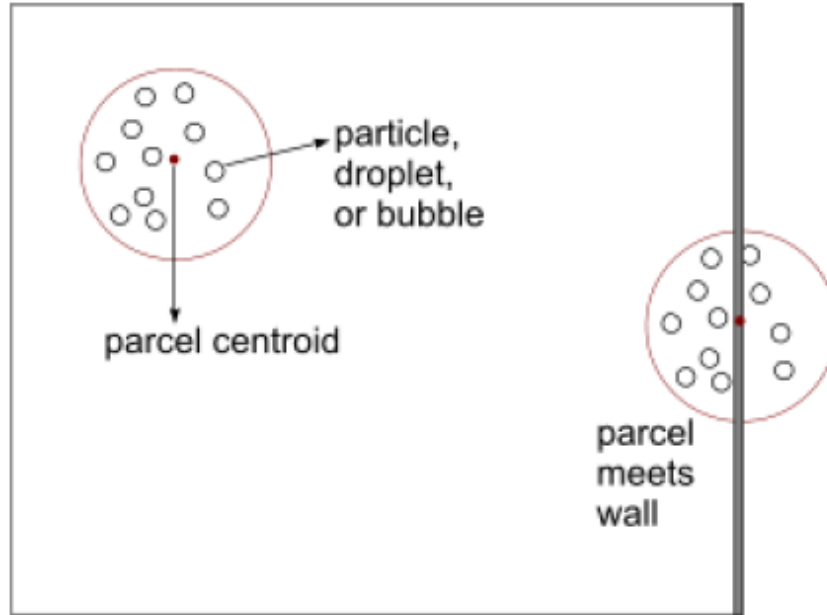


Figure 5.6. Definition of a parcel and its interaction with the wall [59]

Once the particles were injected into the domain, the behavior of the dispersed phase was governed by a series of sub-models associated with this approach. The particles were considered to be of constant density and inert, i.e., they do not react with the flow. Since the continuous phase was turbulent, a turbulent dispersion model was activated to account for the randomness due to the interaction of the particles with the velocity field, resulting in statistically meaningful results. The continuous and dispersed phases were two-way coupled in the mass and momentum equations. Coupling of the energy equations was not required as the particles were considered to be non-reactive and did not have any heat transfer characteristics associated with them. In addition, drag force as well as erosion models were incorporated into these studies and explained further in the coming sub-sections. The Discrete Element Model (DEM), described below, was used to model the

interaction between the particles in the flow.

5.3.5 Force Models

The conservation equation of momentum for a particle in the Lagrangian framework as per the STAR-CCM+ user manual are presented here [59]. The rate of change in momentum is balanced by the body and surface forces acting on the particle. The momentum conservation equation for a particle of mass m_p is given by Equation 5.2

$$m_p \frac{dv_p}{dt} = F_S + F_B \quad (5.1)$$

where v_p denotes the instantaneous particle velocity, F_S is the resultant of the forces that act on the surface of the particle, and F_B is the resultant of the body forces. The Froude number based on the fluid velocity and characteristic length scales was very large for the cases discussed in this chapter. The effect of gravity and thereby buoyancy were therefore negligible. Also, there were no electrostatic or electromagnetic forces involved. The surface forces are further decomposed into:

$$F_S = F_D + F_p + F_{vm} \quad (5.2)$$

where F_D is the drag force, F_p is the pressure gradient force and F_{vm} is the virtual mass force.

The drag force is the greatest force acting per unit mass of the particle. The definition of the drag force F_D is given by Equation 5.3:

$$F_D = \frac{1}{2} C_D \rho A_p |v_s| v_s \quad (5.3)$$

where C_D is the drag coefficient of the particle, ρ is the density of the continuous phase, v_s is the particle slip velocity (i.e. the difference between the instantaneous velocities of the particle and the continuous phase $v - v_p$) and A_p is the projected area of the particle.

The drag coefficient is dependent on the small-scale flow features around the individual particles and was not explicitly resolved and was modeled. The Schiller-Neumann correlation [81] was selected as it is suitable for small, non-reactive particles in viscous flow. The formulation for C_D in terms of the particle Reynolds number Re_p is given by Equations 5.4 and 5.5:

$$C_D = \begin{cases} \frac{24}{Re_p} (1 + 0.15 Re_p^{0.687}) & Re_p \leq 10^3 \\ 0.44 & Re_p > 10^3 \end{cases} \quad (5.4)$$

$$Re_p = \frac{\rho |v_s| d_p}{\mu} \quad (5.5)$$

where d_p is the particle diameter, μ is the dynamic viscosity.

The virtual mass force F_{vm} is a reaction force exerted on a moving particle by the surrounding fluid, as fluid accelerates to occupy the empty space the particle leaves behind [82]. This is an optional model and is negligible for particle-gas flows. This force affects the particle motion and determines the particle track and is given by the Equation 5.6:

$$F_{vm} = C_{vm}\rho v_p\left(\frac{Dv}{Dt} - \frac{dv_p}{dt}\right) \quad (5.6)$$

where C_{vm} is the virtual mass coefficient. The default value of 0.5 is used for this study.

The pressure gradient force F_p is the force due to pressure gradients in the flow and is given Equation 5.7:

$$F_p = -V_p\nabla p_{static} \quad (5.7)$$

where V_p is the volume of the particle and ∇p_{static} is the gradient of pressure in the continuous phase.

Discrete Element Model (DEM) is an extension of the Lagrangian model. The DEM solver was activated to model the inter-particle forces as a result of particle to particle collision that is encountered in these flows. This is done by including a contact force F_C term in the momentum conservation equation of the particles. The contact force between the parcels is dependent on the area of the contact plane between them.

5.3.6 Particle Injection

The surface injector option was utilized for this study. The surface injector enabled the uniform injection of particles at the inlet. The surface injector allowed the specification of number of injection points at the surface using an injection point density parameter defined in terms of injection points per unit area. It also allowed for the randomization of injection sites as well as time-randomization which further

enhanced the random, i.e., realistic, nature of particle injection in addition to the turbulence. Mass flow rate of the particle phase was specified along with these injector options and ensured that the required mass flow rate of particles is injected into the flow.

5.3.7 Erosion Models

Several erosion models are available in literature for the modeling of impact wear due to particle incidence on different materials. These are empirical models devised as per the conditions studied in each set of experiments leading to the corresponding model. The general correlation of erosion rate which has been established empirically [83] [84] is given by Equation 5.8 shown below:

$$E = M_p K F(\theta) v_p^n \quad (5.8)$$

where, E is the weight loss of the target material, M_p is the total mass of particles hitting the target material, v_p is the particle impact velocity, θ is the particle impact angle, K and n are constants that depend upon the physical characteristics of the combinations of materials used for the empirical study and $F(\theta)$ is an angle function describing the dependence of erosion on the particle incidence angle.

The variables M_p , v_p and θ are computed by the Lagrangian solver, while the constants K and n are dependent on the impact wear model selected. There are several models available in literature for the combinations of gaseous continuous phase and solid dispersed phase, namely, Oka [85], [86] and [87], DNV [88], Zhang [89] and Mansouri [49]. All the models are empirical in nature based on fitting the data-

sets produced in the respective studies. The models are based on the volumetric erosion rate (mm^3/kg) i.e. the volume of the eroded material removed mm^3 per the amount of erodent material (kg) incident upon the sample studied. It might be noted, in erosion literature, the "rate" is not a time rate of change as normally defined in fluid mechanics and CFD applications. The results are typically reported as the volume of the eroded material lost per mass of erodent particle incident over a given time duration.

A numerical study on erosion model selection was performed by Weng and Cao [90] in the case of a pipe bend with gas-solid flow. The DNV model was found to be most accurate for the erosion characterization in the study. They observed good agreement between the predictions and the experimental data. The other models either over-predicted or under-predicted the erosion. A study of the different models for the method validation effort in this dissertation showed that all the models besides the DNV model resulted in over-prediction to the tune of several orders of magnitude. The results are shown in Table 5.3. The exact values are not presented here since the study of suitability of the erosion models was performed on a single realization of the simulation run for each case.

Table 5.3. Erosion Model Comparison

| Model | Maximum Depth of Cut (μm) |
|------------|--|
| Experiment | 34 ± 5 |
| DNV | 32 |
| Oka | Over-prediction by $O(10^1)$ |
| Zhang | Over-prediction by $O(10^3)$ |
| Mansouri | Overprediction by $O(10^3)$ |

The DNV model was selected for this study. The model of impact erosion

was described in detail in [88]. Haugen et al. [88] performed an empirical study considering erosion in choke valves used in the oil and gas industry. A total of 28 different materials including standard steel grades, solid tungsten carbide materials, coatings and ceramics were tested under various impact angles and velocities of sand particles, and examined for erosion characteristics. The test results were used to determine an empirical model in terms of Equation 5.8. The impact angle (22.5° and 90°) and impact velocity (20m/s-200m/s) were varied to determine K and n for each material. $F(\theta)$ for all materials was determined through the study and is given by Equation 5.9 as shown below:

$$F(\theta) = \sum_{i=1}^8 (-1)^{(i+1)} A_i \left(\frac{\theta\pi}{180}\right)^i \quad (5.9)$$

where the constants A_i s are given in Table 5.4.

Table 5.4. Values of A_i in angle function $F(\theta)$ in DNV model [88]

| A_1 | A_2 | A_3 | A_4 | A_5 | A_6 | A_7 | A_8 |
|-------|--------|---------|---------|---------|--------|--------|-------|
| 9.370 | 42.295 | 110.864 | 175.804 | 170.137 | 98.298 | 31.211 | 4.170 |

The chosen parameters K and n for the sand and steel combination were 2.0×10^{-9} and 2.6 respectively.

5.3.8 Coefficients of Restitution

The coefficients of restitution (tangential (CoR_{tang}) and normal (CoR_{norm})) dictate the magnitude of the rebound velocity for the parcels. This is governed by the momentum transfer occurring as a result of the interaction of the parcels with solid boundaries, which in turn affects the erosion behavior. Appropriate modeling of

these coefficients is necessary for accurate prediction of the erosion of the boundary. Several efforts have been made to model these coefficients. Grant and Tabakoff [91] devised a formulation for the coefficients of restitution based on their computational study into the prediction of erosion patterns in turbomachinery due to sand ingestion. They were based on a polynomial fit of their data and are dependent on the particle incidence angle (θ) in degrees. The coefficients of restitution are given in Equations 5.10 and 5.11.

$$CoR_{norm} = 0.993 - 0.0307\theta + 0.000475\theta^2 - 0.00000261\theta^3 \quad (5.10)$$

$$CoR_{tang} = 0.988 - 0.0290\theta + 0.000643\theta^2 - 0.00000356\theta^3 \quad (5.11)$$

5.3.9 Grid Independence Study

Since the method validation was performed using the data from Nguyen et al. [48], a grid independence study was performed for the case of 30s of erosion at an impact angle of 90° . Three different meshes namely, Grid 1, Grid2 and Grid3 in increasing order of mesh density were run. For each of the meshes, the methodology described in the previous sections were employed where several realizations were run, and the ensemble average of the time-averaged erosion was computed. Grid 1 over-predicted the maximum depth of cut compared to Grids 2 and 3, but the surface profiles were generally same in terms of their shape. There were no significant differences between the predicted eroded surface profiles and the maximum depth of cut and profiles for Grid2 and Grid3 as shown in Figure 5.7. Accordingly, the meshing parameters

of Grid2 mesh were used for the method validation study as a compromise between computational expense and accuracy. The results of the grid independence study are presented in Table 5.5.

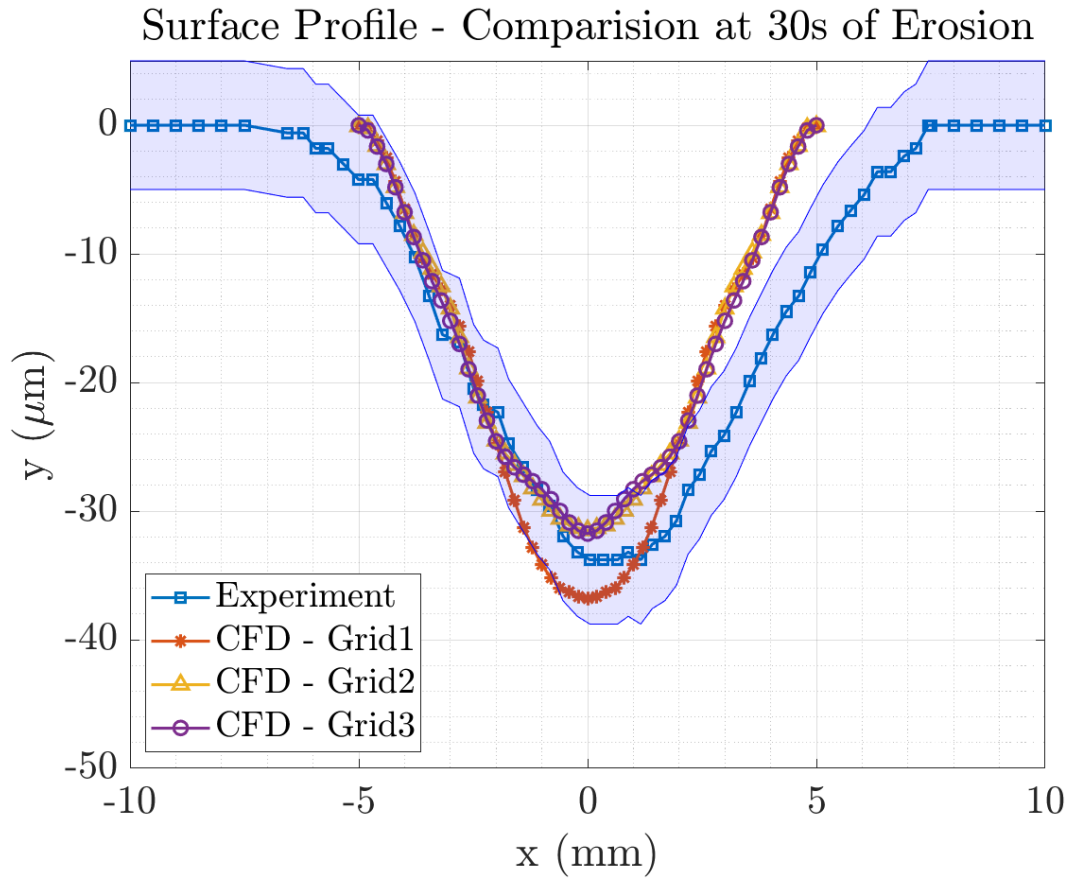


Figure 5.7. Surface profiles of the sample at 30s of erosion for the different grids

Table 5.5. Results - Grid Independence Study - Validation Case

| Case | Cells | Maximum depth of cut (μm) |
|------------|--------|--|
| Experiment | NA | 34 ± 5 |
| Grid1 | 131258 | 37 |
| Grid2 | 169496 | 32 |
| Grid3 | 270497 | 32 |

5.4 Results

The results of the method validation case are presented first and discussed. This is followed by the results of the erosion studies for the NASA Rotor 37.

5.4.1 Method Validation Case

The results of the CFD simulations for the erosion study for the validation case are discussed here. The technical approach was discussed in Section 5.3. The results of the validation case are presented in terms of flow field, surface profiles, surface contours and maximum depth of erosion cut at different time intervals defined in the experimental case by Nguyen et al. [48].

The velocity magnitude contours of the fluid phase are shown in Figure 5.8. There was acceleration of the flow as the boundary layer growth resulted in a convergent nozzle effect. As expected, the turbulent jet expanded and formed an entrainment region and impinged on the sample surface. A stagnation region was formed close to the center of the sample.

The velocity vectors for the different phases are shown in Figure 5.9. As expected, the particle vectors closely followed the streamlines of the air jet until impact at the sample surface. After the impact, the particles scattered outwards. The particles in the experiment were injected at 200m/s. The particles were observed to have a maximum velocity of about 203m/s at impact. Nguyen et al. [48] did not perform any particle velocity measurements at the exit of the nozzle or any other cross-section. Hence, the particle velocity could not be verified.

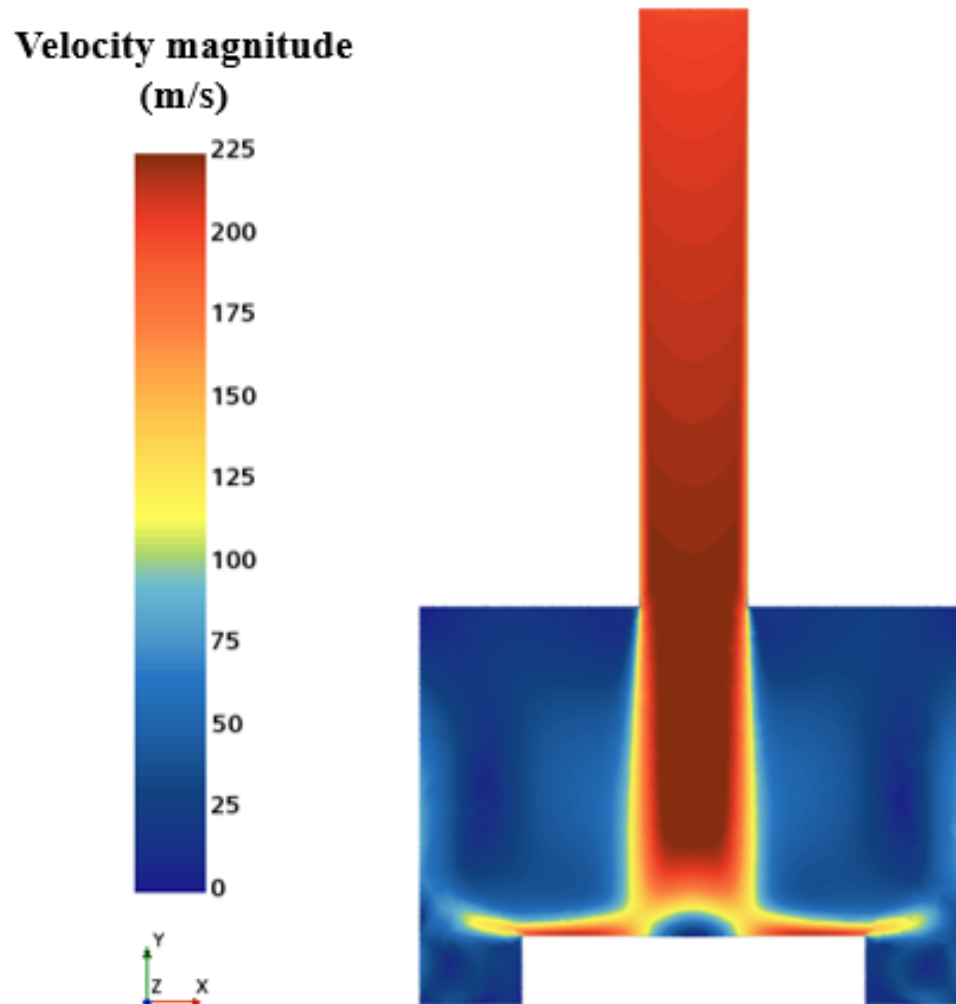


Figure 5.8. Mid-section view of velocity magnitude contours of the fluid phase

It must be noted that the surface profile data were discrete as the data were extracted from the unstructured surface mesh of the sample and hence a blending contour style was used. Figure 5.10 shows the time-averaged eroded surface depth contours of a single realization. The contours were observed to be not fully axisymmetric. The patchiness in the erosion was attributed to the stochastic nature of the model. The particle paths were observed to be affected by the randomness of the Lagrangian particle paths in the flow. The randomization options within

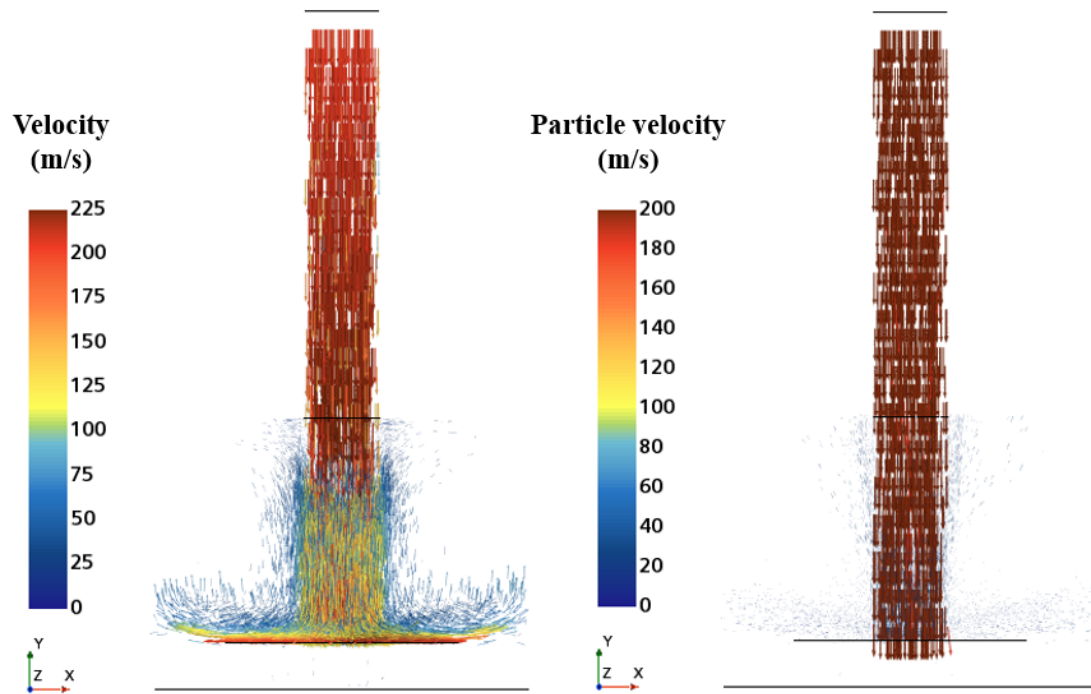


Figure 5.9. Mid-section view of the velocity vectors: fluid phase (left), particle phase (right)

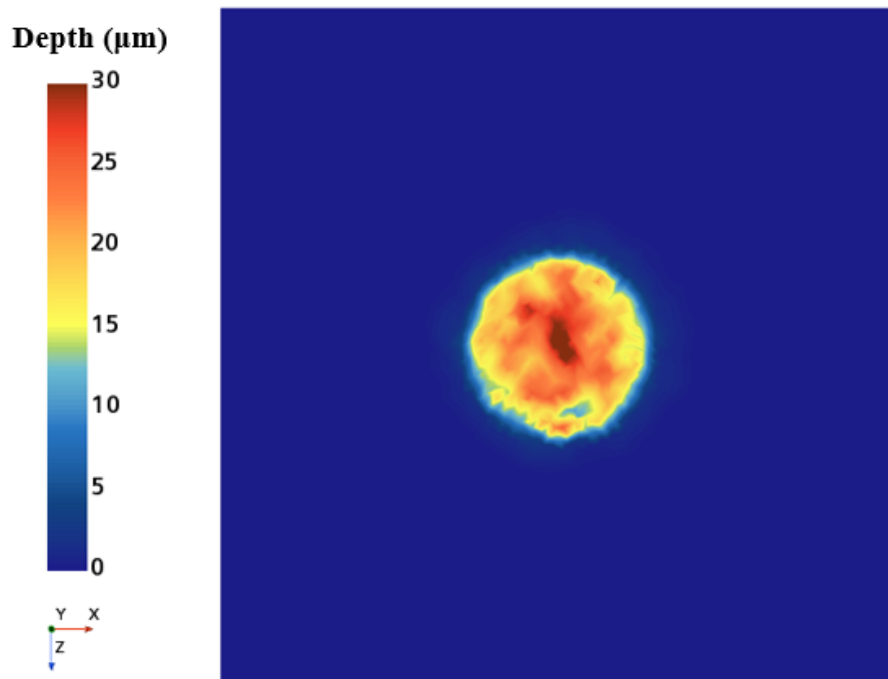


Figure 5.10. Sample surface contours of time-averaged eroded depth at 30s of erosion for a single realization

the surface injector also enabled this observation and reflected real world scenario where the particles are not uniformly distributed within the flow. This necessitated the need for ensemble averaging to produce statistically meaningful results.

In order to enable a direct comparison to the surface profile data in Figure 5.2, the cylindrical average at different radial locations from the sample mid-point was taken. Then, the ensemble average was computed from the data obtained from various realizations of the time-averaged results. Figures 5.11 and 5.12 illustrate the ensemble averaged surface profiles for different number of realizations.

Ensemble 1 consisted of 2 realizations, Ensemble 2 of 3 realizations and so on. 10 realizations were used for the ensemble averaging and was deemed to be sufficient for the averaging since there were no perceptible differences in the ensemble averaged surface profile after 6 realizations were used.

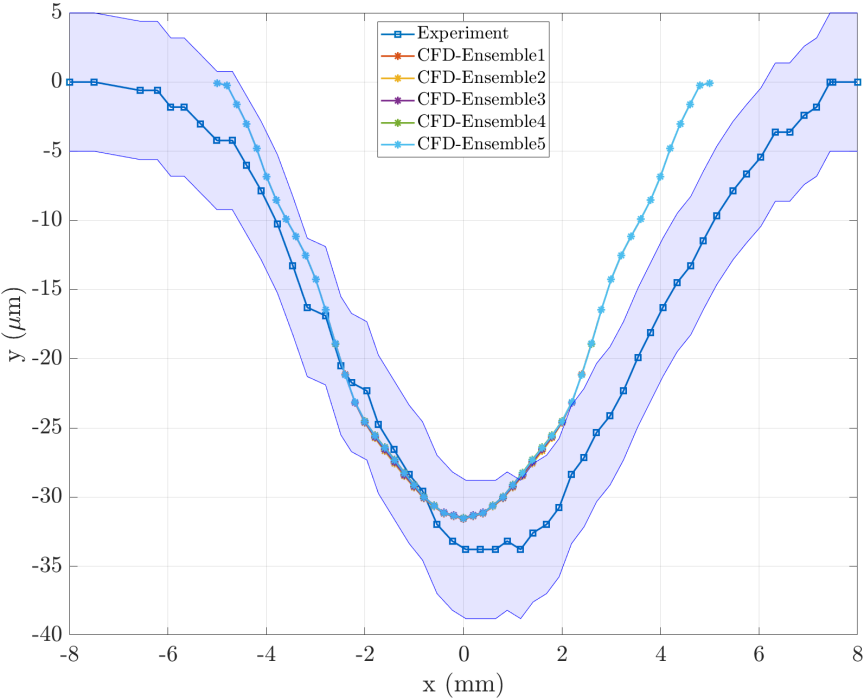


Figure 5.11. Comparison of ensemble averaged surface profiles using 2 to 6 realizations

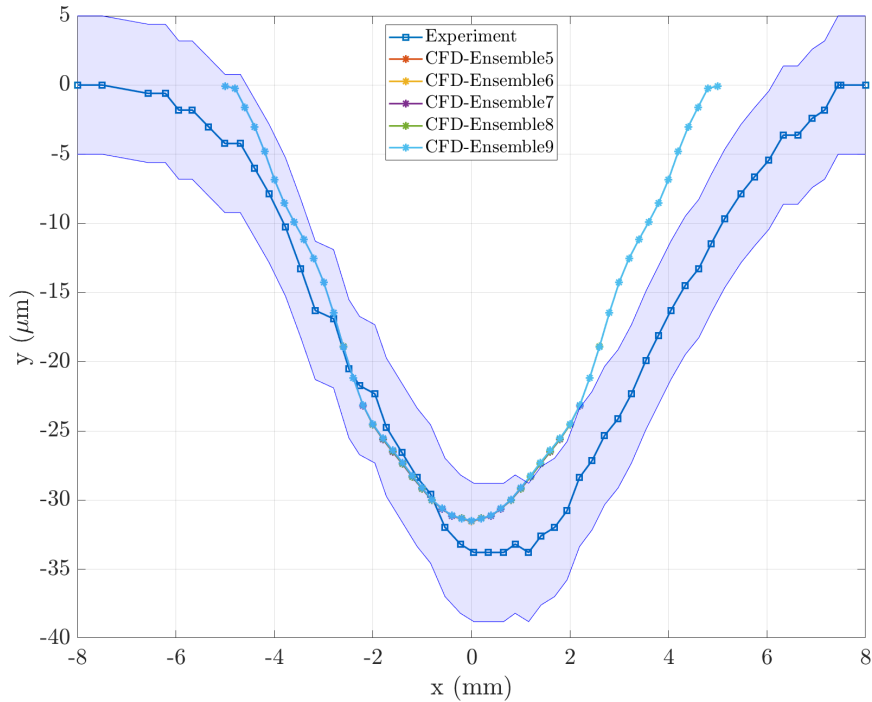


Figure 5.12. Comparison of ensemble averaged surface profiles using 6 to 10 realizations

Figure 5.13 shows the ensemble averaged surface profile of the sample surface after 30s of simulated erosion. It was seen that there was good agreement between the experimental and CFD results. The CFD results were observed to be within the measurement uncertainty of the experimental results.

As a result of the cylindrical averaging, the CFD results were enforced to be symmetric about the nozzle axis unlike the experimental results as shown in Figure 5.2. It must be noted the experimental results for other times at 60s, 120s, 240s and 300s were symmetric. The shift in the center point of the experimental surface profile measurements at times at 30s and 180s could be attributed to measurement uncertainties of the surface profilometry. The maximum depth of cut of the CFD results were within the uncertainty limits of the experimental results and was almost 94% of the experimental value. The CFD surface profile was almost Gaussian and

Surface Profile - Comparison at 30s of Erosion

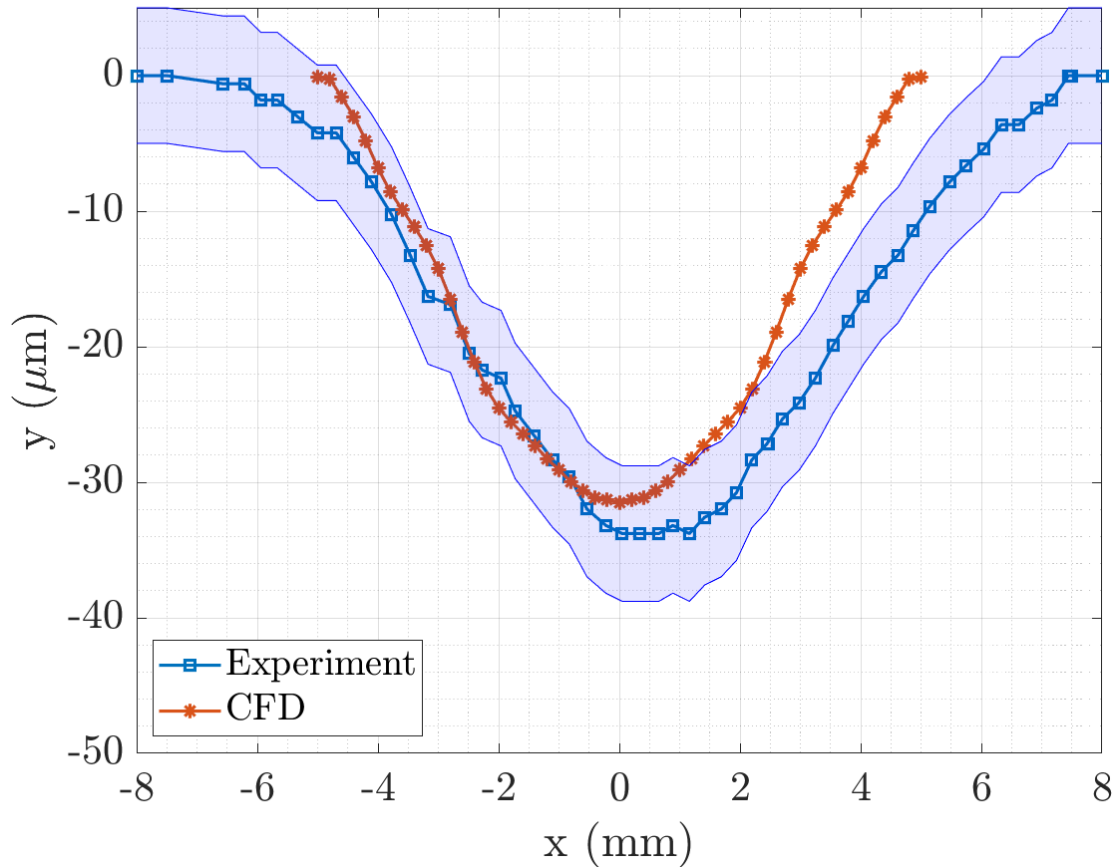


Figure 5.13. Comparison of ensemble averaged sample surface profile at 30s of erosion had a similar slope as the experimental results. Figure 5.14 shows the ensemble averaged surface contours of the eroded surface depth at 30s of erosion. The eroded surface depth profile was in good agreement with the contours shown in Figure 5.1.

Figures 5.15 and 5.16 show the surface profile of the sample surface after 60s and 120s of simulated erosion. Unlike the 30s case, there was severe under-prediction in the predicted erosion depth. In the 60s case, the maximum erosion depth was about 14% less than the experimental results. In the 120s case, the maximum erosion depth was about 55% less than the experimental results.

It was noted that there was no significant change in the flow field. The maxi-

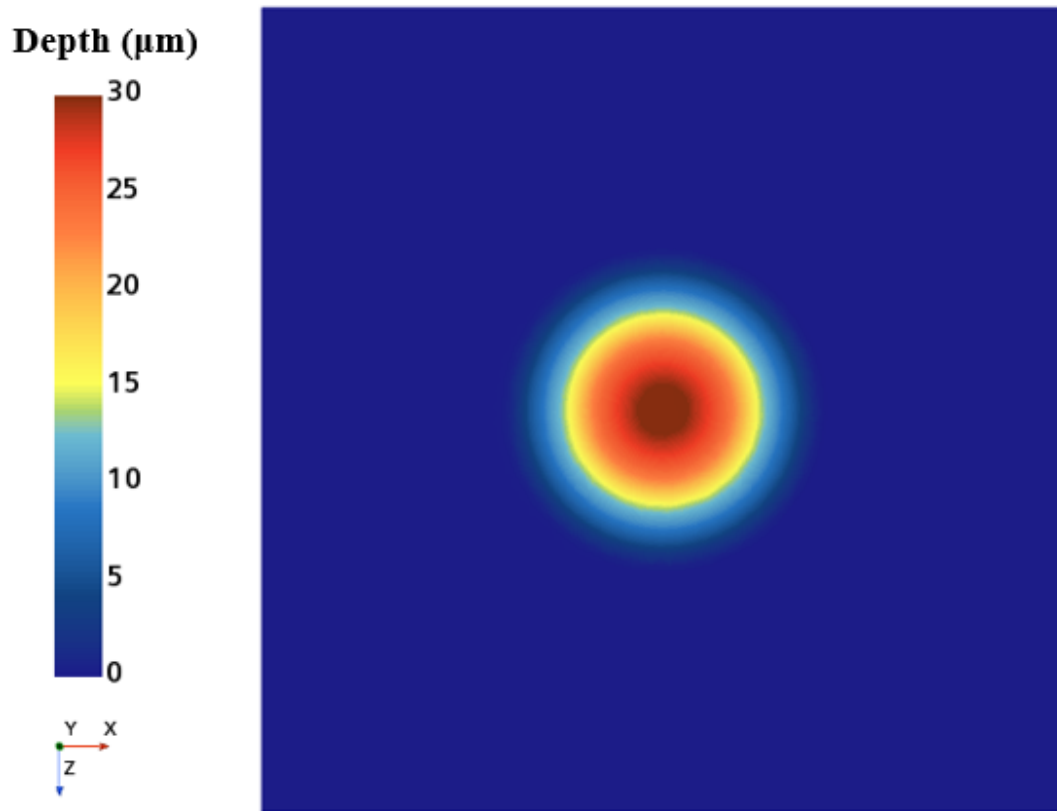


Figure 5.14. Ensemble averaged sample surface contours of eroded depth at 30s of erosion

imum depth of cut in the experimental case was $221\mu\text{m}$ i.e., 0.221mm , which was insufficient to cause any appreciable changes in the flow. This observation was a direct result of the formulation of the erosion models. A closer look at the main erosion model Equation 5.8 showed that the models do not have a time-varying variable which could have explained the time variation in the erosion rate seen in the experimental results.

Figure 5.17 shows comparison of the maximum depth of cut for the 90° impact angle case between the experimental and CFD results. The CFD results at 180s, 240s and 300s were obtained as a result of linear extrapolation.

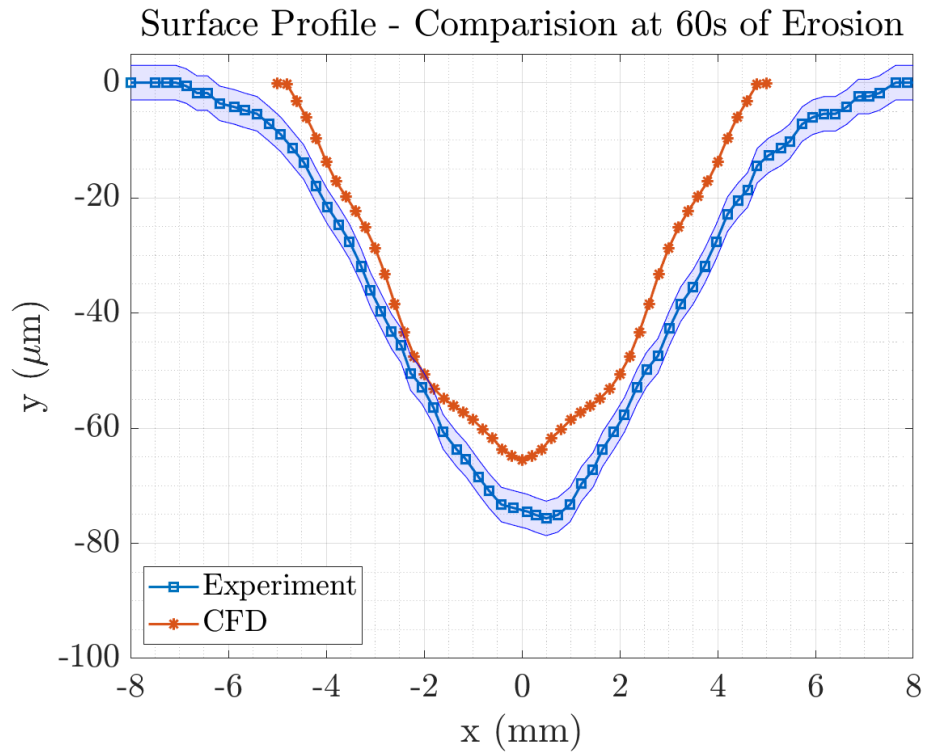


Figure 5.15. Comparison of ensemble averaged sample surface profile at 60s of erosion

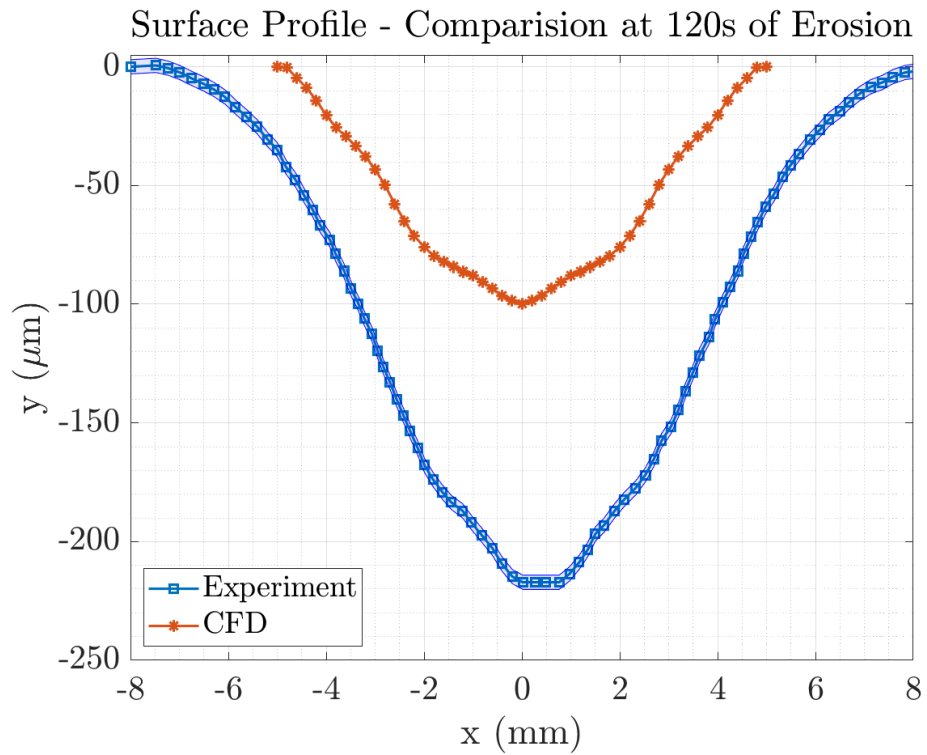


Figure 5.16. Comparison of ensemble averaged sample surface profile at 120s of erosion

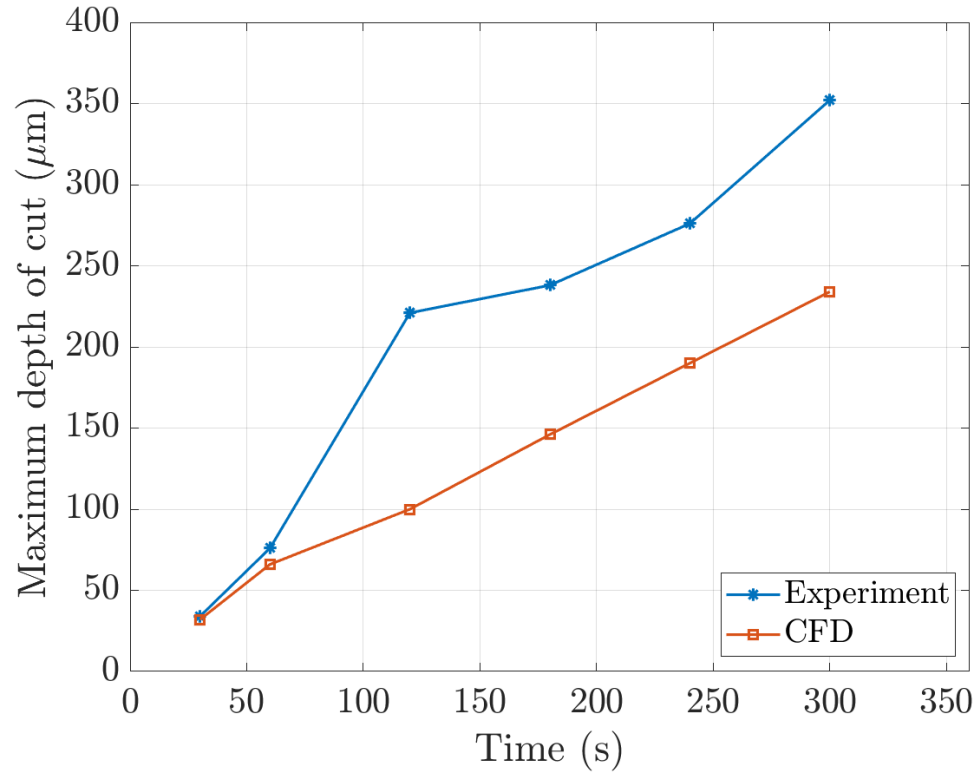


Figure 5.17. Comparison of time evolution history of maximum depth of cut of the sample surface

It was observed that the erosion rate initially increased between 30s and 120s and then decreased between 120s and 180s and then increased beyond 180s. This was attributed to the physical process of strain hardening of the sample material, which is a time-varying phenomenon. This time dependence of the erosion rate has not been taken into account by any existing erosion models available. This pointed to the need for an erosion model that could sufficiently capture the time varying nature of erosion while being rooted in the physics associated with erosion, particularly the mechanisms involved in material removal when particle impaction occurs.

5.4.2 Erosion Characterization of NASA Rotor 37 Blade Surface

The method validation case showed that STAR-CCM+ [59] could be a useful tool for qualitative estimates of erosion in terms of erosion patterns. Hence, a qualitative study of damage due to erosion was performed using the NASA Rotor 37 configuration. As discussed in Chapter 2, NASA Rotor 37 is a well-studied axial compressor transonic stage. In this section, the results for the qualitative estimates of blade surface erosion patterns are presented.

The technical approach discussed in Section 5.3 was utilized with some modifications. Firstly, since the aim was to perform a qualitative estimate, a steady-state analysis was performed. The algorithm in Section 5.3.1 was not utilized as the time evolution history of erosion was not computed. Secondly, the meshing strategy, computational domain and boundary conditions outlined in Chapter 2 were utilized. Finally, to simulate realistic particle ingestion for turbomachinery applications, the injected particles were considered as per the specifications found in the work by Ghenaiet et al. [16]. The particle distribution studied by Ghenaiet was representative of the typical particles ingested by aero-engines. The particles mainly consisted of silica sand (0 - 1000 μ m), which is commonly used for gas turbine erosion testing according to US Army specifications MIL-E-5007E [92]. The injected particles consisted of sand of density 2600kg/m³ and the cumulative distribution of the particle size is given in Figure 5.18. The mass flow rate of ingested particle was specified to be 0.2g/s, which corresponded to a medium particle concentration.

The flow field and other characteristics of NASA Rotor 37 were discussed in

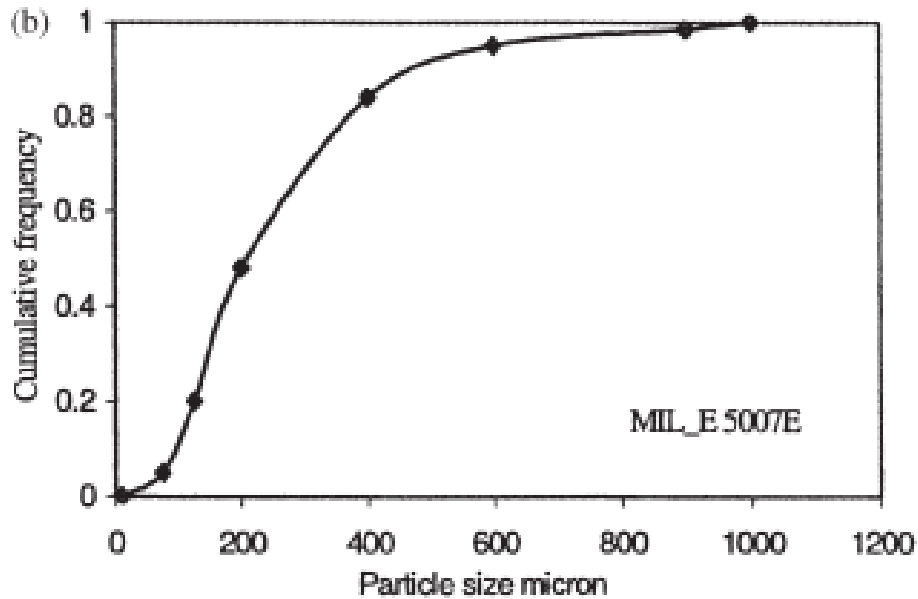


Figure 5.18. Cumulative distribution of sand particle size as per MIL-E-5007E [92]

detail in Section 2.2. The results of the erosion study are presented here. Figures 5.19 and 5.20 show the predicted erosion patterns on the pressure side and the suction side respectively of the Rotor 37 blade surface. The surfaces were contoured with the erosion flux for making a qualitative assessment of the erosion impact. The contours were graded on a logarithmic scale.

The patchiness of the erosion patterns was ascribed to the stochastic nature of the Lagrangian particle model. This was expected as a result of the large number of particles and the randomness of the particles paths. This was also observed in the results of the method validation case described in Section 5.4.1. Specifically, the erosion flux was computed at the surface where particle impact had taken place and the steady-state erosion pattern was obtained. As expected, the erosion was observed to be more significant on the pressure side than the suction side. On the pressure side, maximum erosion was observed at the hub and the tip clearance

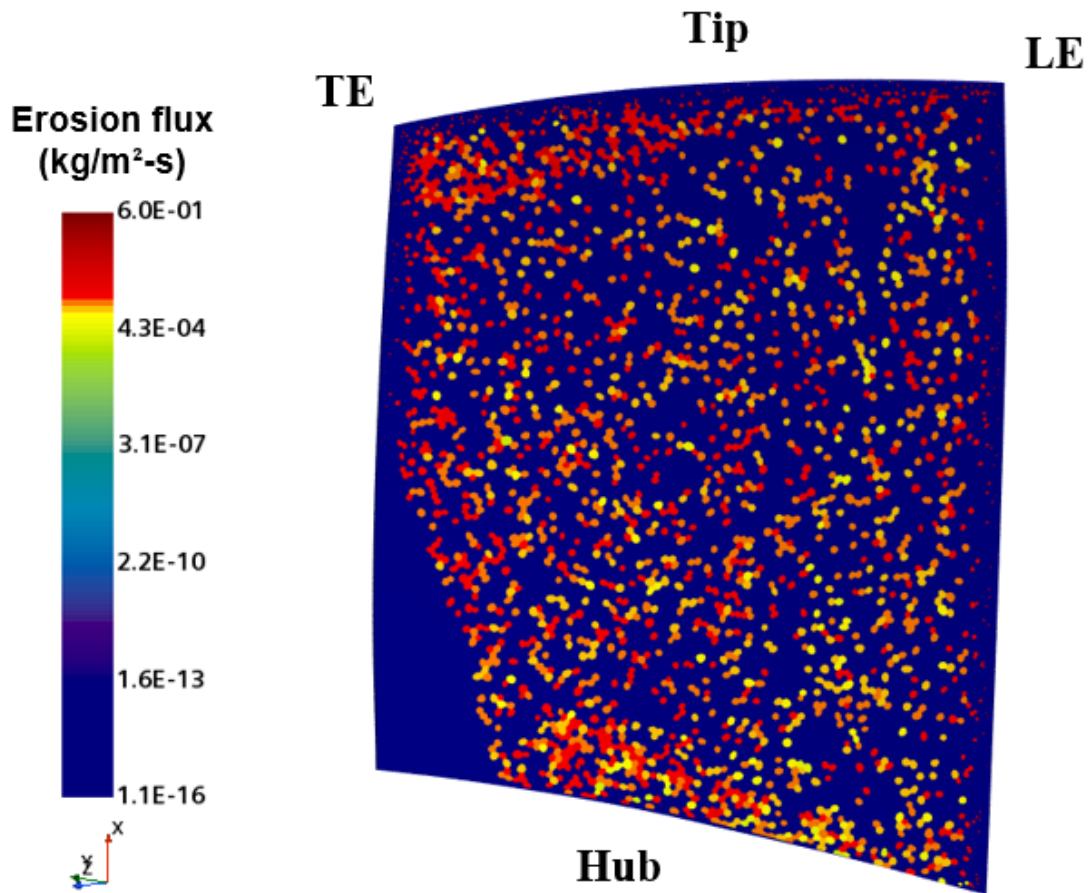


Figure 5.19. Surface erosion patterns on blade pressure side of NASA Rotor 37

region and differed from the rest of the surface by several orders of magnitude. Due to centrifugal forces, the particles move outward radially. The tip clearance flow from the pressure side to the suction side caused the increased erosion in the tip clearance region of the pressure side as it carried the particles with it. These observations were consistent with Yamada and Suzuki [73]. The difference in the erosion impact between the pressure side and the suction side was attributed to the high incidence angles of particles on the pressure side leading to more erosion there.

Figure 5.21 shows the leading edge and trailing edge regions of the NASA Rotor 37 blade surface. Again, as expected, the erosion damage was mostly observed

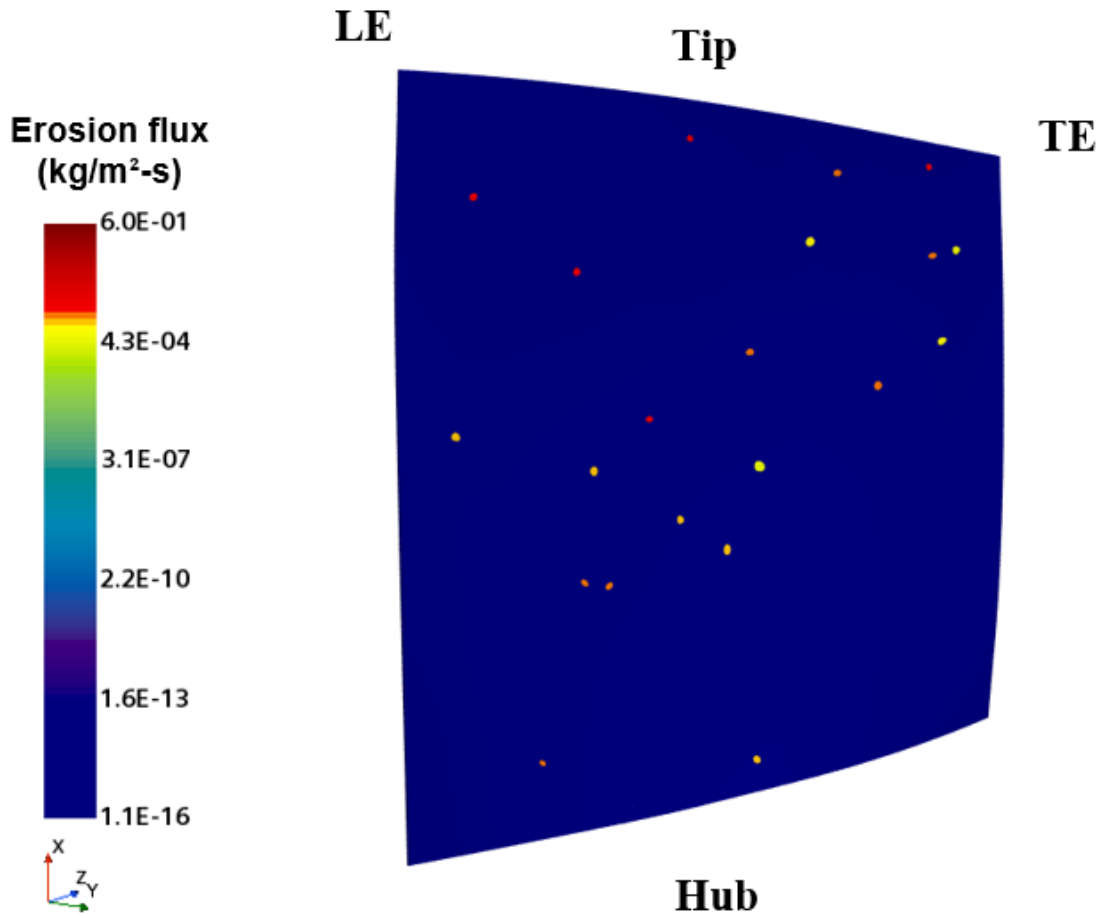


Figure 5.20. Surface erosion patterns on blade suction side of NASA Rotor 37

along the complete span (hub to shroud) of the leading edge region as it bore the brunt of the incoming particles. In the trailing edge region, the particle impaction was observed to be considerably lower, leading to reduced erosion.

Figure 5.22 shows the shroud and hub regions of the NASA Rotor 37. Again, as expected, the erosion damage was mostly observed on the shroud compared to the hub. This was due to the fact that the centrifugal forces acting on the particles forces them to move radially outwards resulting in increased impaction on the shroud surface.

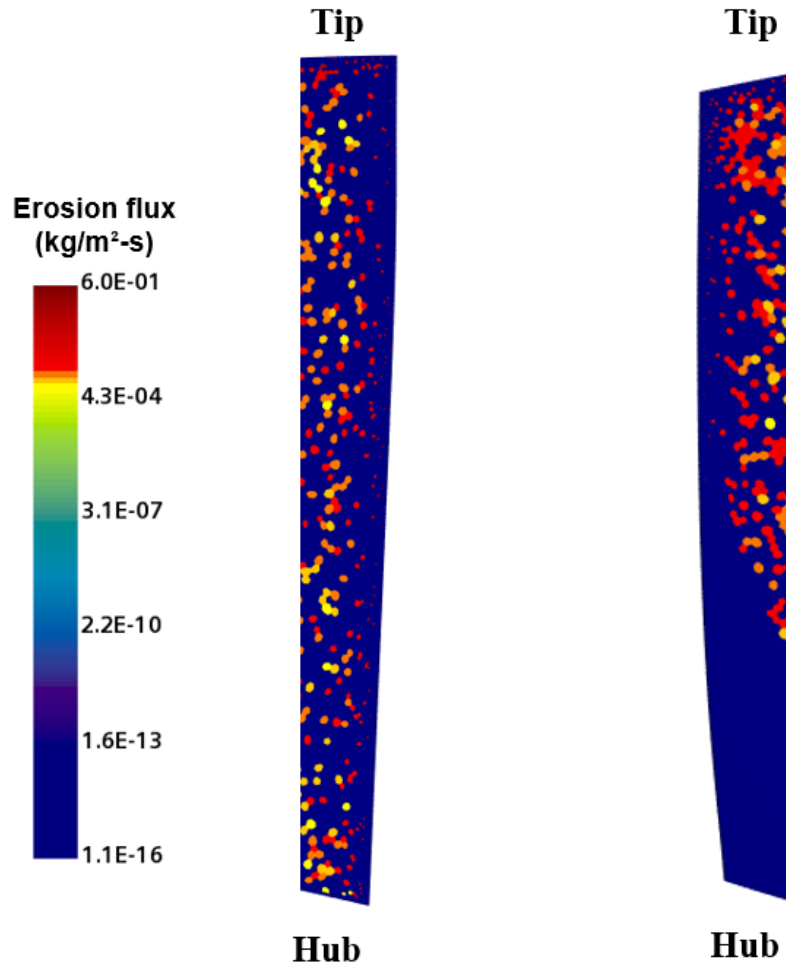


Figure 5.21. A close up view of surface erosion patterns on leading (left) and trailing (right) edges of NASA Rotor 37

The quantitative analysis of predicting erosion depth was not pursued for this case as validation data were not available and the method validation case illustrated that predictions might not be accurate due to lack of an adequately physics-rich erosion model. The qualitative estimates of erosion patterns were predicted and there was good agreement with previous studies. However, as evidenced by the method validation case as well, there is a need for a time dependent erosion model that can accurately and more importantly quantitatively predict erosion

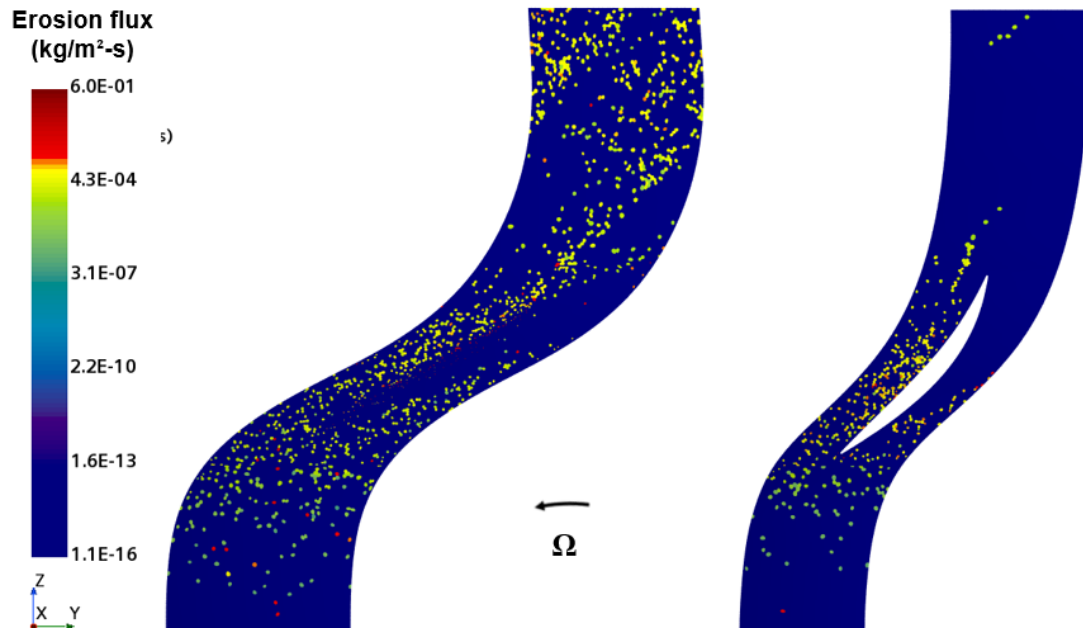


Figure 5.22. A close up view of surface erosion patterns on the shroud (left) and hub (right) of NASA Rotor 37

depth and hence the eroded surface. An improved erosion model in conjunction with the algorithm outlined earlier in this chapter would be required to make accurate quantitative predictions for erosion damage for axial compressors that ingest particles.

5.4.3 Erosion Coupled Deformation of NASA Rotor 37 Blade Surface

An illustration of the erosion coupled deformation of the NASA Rotor 37 blade surface is discussed in this section. For this illustrative study, the simulation parameters from Section 5.4.2 were used. The study was limited to the blade spans ranging from 40% span to 60% span. Figure 5.23 shows the erosion patterns on the pressure and suction sides of the blade and were consistent with the observations

in the previous section. Figure 5.24 shows the erosion patterns on the leading and trailing edge regions of the blade and were observed to be consistent with the findings in the previous section, where the leading edge region was more damaged than the trailing edge.

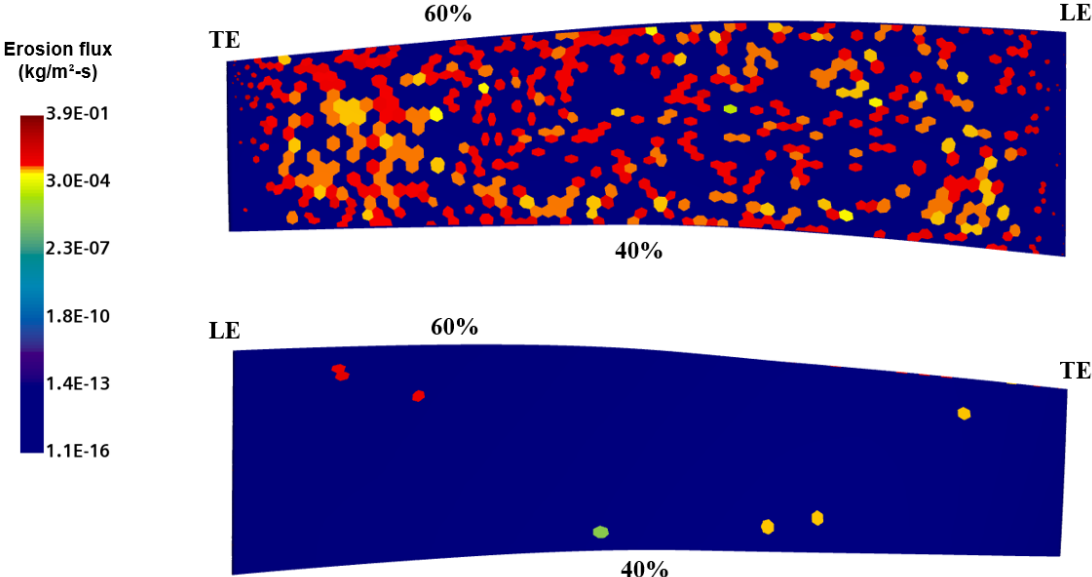


Figure 5.23. Surface erosion patterns on the section of Rotor 37, pressure side (top), suction side (bottom)

The erosion was computed in terms of wear depth per second and multiplied by a factor of 60 in order to simulate erosion at 60s. This erosion displacement was input into the Surface Morphing algorithm available in STAR-CCM+ [59]. Figure 5.25 shows the pressure side leading edge of the blade before and after the damage computation. The surface deformation was minimal (in the order of micrometers or less) as expected after 60s of simulated erosion. The difference is almost imperceptible in the figure. However, a close examination of the leading edge region showed differences in the surface indicated by the differences in the surface edges. A comparison of the domain volume before and after the surface

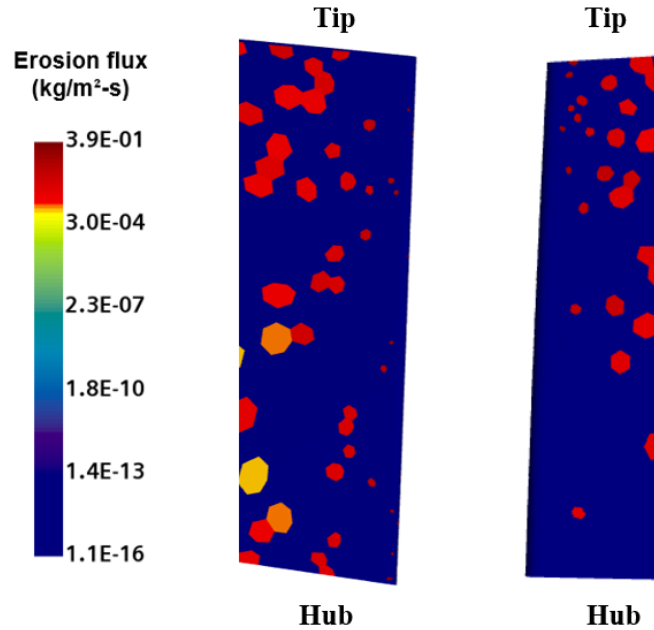


Figure 5.24. Surface erosion patterns on the section of Rotor 37, leading edge (left), trailing edge (right)

morphing showed that the volume increased by 0.0003% indicating that the rotor blade surface had been eroded. It was noted that these results were only illustrative of the effectiveness of the methodology described in this chapter and did not provide quantitative estimates of the erosion damage. With the inclusion of a time varying erosion model validated for erosion of axial compressor blades, the methodology outlined in this dissertation could prove to be an effective tool in erosion prediction and thereby provide performance assessment of these machines.

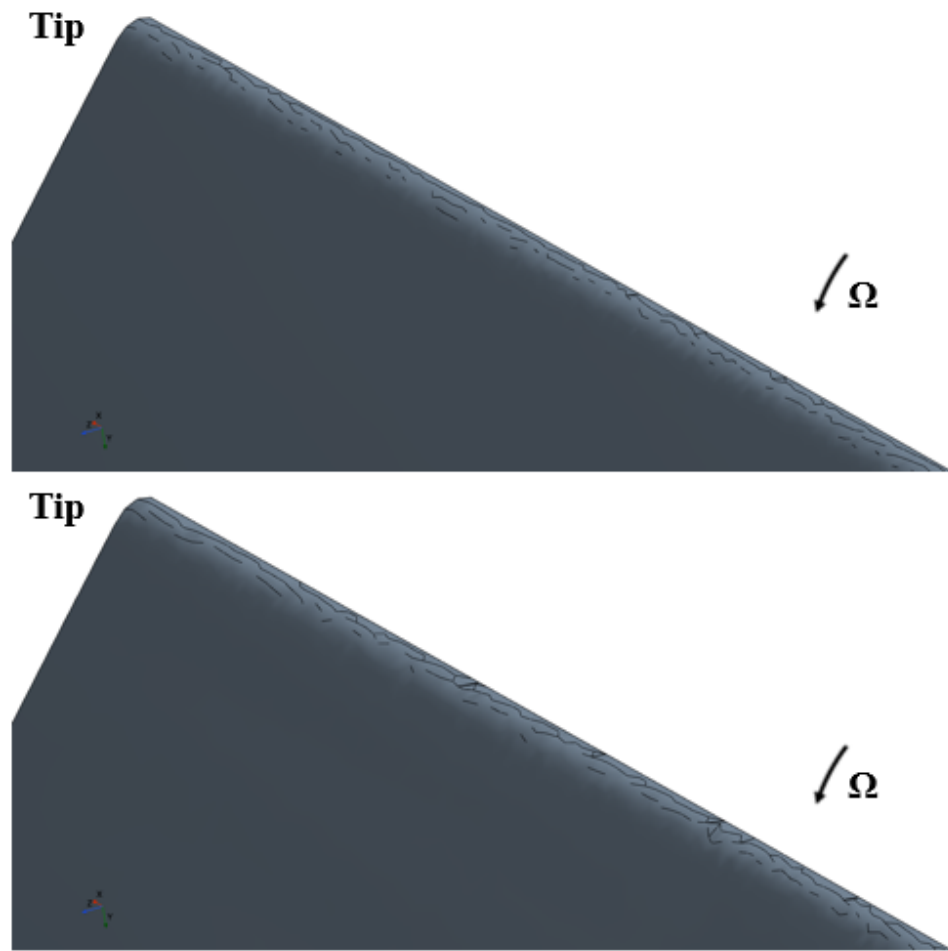


Figure 5.25. Pressure side leading edge of Rotor 37, before damage (top), after damage (bottom)

Chapter 6 |

Summary and Future Work

This chapter provides a summary of the research undertaken, research contributions and conclusions, and the scope of future work.

6.1 Summary

In Chapter 1, the background and motivation behind this dissertation was discussed. Ingestion of particulate matter into gas turbine engines has a particularly damaging effect on the front stages of the axial compressor leading to performance degradation, which in turn affects the overall engine performance, fuel consumption, maintenance issues and standby military readiness. The application of CFD along with high performance computing resources and the incorporation of real and fabricated geometries enabled the work presented in this dissertation.

In Chapter 2, the general methodology employed for the different CFD studies using STAR-CCM+ [59] was discussed. The meshing strategy and simulation parameters were presented. Grid independence studies were performed to determine the appropriate meshes for the CFD analyses of the NASA Rotor 37 and T700

first stage respectively. The target operating conditions that conform to real life damage protocols were devised and presented. The methodology was validated using NASA Rotor 37 as a test case.

In Chapter 3, steady-state simulation studies for 4 cases (one undamaged and three damaged) of a rotor only configuration were performed to model the effects of ballistic airfoil damage on axial compressor blading. The results were presented in terms of compressible wave field and secondary/tip flows, spanwise performance parameter distributions and efficiency. A simple scheme to estimate the effect of rotor damage on overall engine SFC was presented. The results enabled the rank ordering of the various damage modes in terms of expected impact on compressor and engine performance.

In Chapter 4, the results for unsteady full stage simulation studies performed for the 4 cases (one undamaged and three damaged) were presented. The results were also presented in terms of compressible wave field and secondary/tip flows, spanwise performance parameter distributions, efficiency and impact on SFC. The different damage modes were again classified according to impact on overall performance parameters. A comparison was made between the steady-state rotor only simulations and the unsteady full stage simulations. It was found that modifications of the flow field due to rotor-stator interaction in the unsteady simulations led to significant change in predictions of performance degradation for the damaged cases.

In Chapter 5, an improved combined Eulerian-Lagrangian methodology was devised to compute the deformation of geometry due to impact erosion. A method validation case using sand in air-jet was performed. The results and conclusions were discussed. A qualitative analysis of erosion for NASA Rotor 37 blade surface

was performed and discussed. A time dependent erosion model is required for making accurate quantitative predictions of erosion damage. An illustration of the erosion coupled surface deformation in STAR-CCM+ [59] of the Rotor 37 blade was discussed.

6.2 Original Contributions of this Dissertation

1. In this work, a thermoplastic Additive Manufacturing (AM) methodology was employed to build a number of baseline undamaged rotor blades, and then heat and tooling treatments were applied to obtain the several ballistic compressor blade damaged geometries, which were then optically scanned and incorporated into sublayer resolved RANS analyses. Specifically, the local aerodynamic and attendant performance implications of representative geometric models of three of these modes were studied – ballistically bent/curved leading edges, spanwise cragged erosion of leading edges, and eroded leading/tailing edges at outer spanwise locations. This new approach for blade damage assessment enabled steady and unsteady models to study the impact of damaged blades on compressor performance without relying on experimental data, which are expensive to obtain, often unreliable in terms of timeline and lack the richness in detail that CFD data provide. The damaged geometries were requested by and sent to NAVAIR for their inclusion in their upcoming experimental study.
2. Target conditions for running the simulation of damaged axial compressor configurations were presented which reflect real life operational scenarios. This

involved quasi-1D compressor meanline velocity triangle perturbation studies and the application of the Euler turbomachinery equation. For the damaged stage simulations, the rotation speed and the outlet hub static pressure were adjusted, during iteration, such that the converged mass flow rate matched that of the on-design mass flow rate, and the stagnation enthalpy rise for the damaged stage satisfies the derived target condition.

3. The transonic first stage of the axial compressor of the GE T700-401C was studied for the first time. The methodology was validated using the experimental data of the well-documented case of the transonic NASA Rotor 37. Steady-state simulations of the rotor only configuration yielded results in terms of flow field, spanwise distributions of performance parameters and impact on compressor pressure ratio and engine SFC. These analyses provided, for the first time, the local physics and performance degradation mechanisms, associated with several damage modes. An approach was developed to incorporate the effects of damage in first stage rotor blading into overall engine performance assessment. Unsteady full stage simulations of the T700 first stage were also performed for the first time. Specifically, full rotor-stator analyses were carried out. In both sets of simulations, the different damage morphologies were rank ordered based on their impact on the overall performance parameters. The differences in steady-state and transient simulations for the T700 first stage were discussed, providing future workers important guidance, and how to approach these models.
4. A combined Eulerian-Lagrangian methodology, used to evaluate the impact

of erosion due to sand particles impaction with improvements based on CFD principles, was devised and implemented in STAR-CCM+ [59] for the first time. The time-averaged erosion field was computed and an ensemble average of the eroded surface profile of several instances was taken to account for the stochastic effect of turbulence on the particle paths. Method validation using a well-documented case of an air jet containing sand particles impinging on a stainless steel sample was pursued and the results and the conclusions were discussed. In addition, a qualitative analysis of the erosion characteristics of NASA Rotor 37 blade surface due to sand ingestion was studied in STAR-CCM+ [59] and the results were presented in terms of erosion patterns and discussed. An illustration of the erosion coupled surface deformation in STAR-CCM+ [59] of the Rotor 37 blade was performed and discussed for the first time.

6.3 Scope for Future Work

There are many possible future directions for this research. There are mainly four recommendations for future work that can be pursued to build up on the research provided in this dissertation.

1. Perform CFD simulations for the full annulus of the compressor of the T700 including the intake geometries as well as the 5 axial compressor stages and the single centrifugal compressor stage and compare it to soon to be available experimental data for validation.

2. Perform CFD simulation of the T700 with scanned geometries of actual damaged blades from the experimental run at NAVAIR using the methodology outlined in this dissertation.
3. Collaborate with research groups studying erosion phenomena to build an erosion model that incorporates the time-dependent nature of erosion physics and validate it using CFD studies.
4. Perform CFD studies of the impact of particulate deposition and surface roughness changes of the blade geometry on the performance of axial compressors.

6.3.1 Full annulus CFD simulations of the T700

Since the experimental data for the T700 are forthcoming in Fall 2023, a full annulus CFD simulation of the T700 intake and compressor section would be very valuable in further lending credence to the methodology of CFD simulations for the undamaged configuration outlined in this dissertation. This will add to the validation provided by the CFD study of the NASA Rotor 37. It is hoped that measurements of average stagnation pressure and temperature as well as their spanwise distribution at different stations along the compressor could be used for the validation. The CFD could include all the intake geometry including the inlet, filter scroll, de-swirler, inlet guide vanes, the 5 stage axial compressor and the single stage centrifugal compressor.

6.3.2 CFD simulation with real damaged blades

Damaged blades from the forthcoming test at NAVAIR could be incorporated into CFD studies using the methodology outlined in Chapters 2, 3 and 4 in this dissertation. This will again lend additional credence to the robustness of the methodology and would also lead to validation of the data for the damaged configurations. In addition, the performance assessment of the axial compressor with damaged blades could be used to create a catalogue of damage modes and their associated performance degradation metrics. In the case when damaged blades are not available, more damage configurations could be obtained from literature and studied. A large array of damage modes incorporated in a catalogue format could be useful in future instruction of maintenance crews as they could be trained to assess the performance impact of the axial compressor through visual inspection and compare it to the CFD predictions of performance degradation.

6.3.3 Time-dependent erosion models

As evidenced in Chapter 5 of this dissertation, a time-dependent erosion model is necessary to capture the physics of the material removal involved in the erosion process. Currently, the available models namely, Oka [85], [86] and [87], DNV [88], Zhang [89] and Mansouri [49] fail to capture the time-varying nature of the erosion process. This could be attributed to the models being empirical in nature and not completely rooted in the physics of the erosion process. In the case of a physics based model not being achievable, an empirical model with the addition of time as a variable should be considered in addition to the existing parameters

such as impact velocity, impact angle and hardness value. This research could be pursued in collaboration with research groups specialized in erosion. There is a lack of collaboration between research groups pursuing erosion research and CFD research. This gap of research knowledge is worth exploring and could yield results beneficial to both communities. The new models could be utilized in more accurately predicting erosion in compressors using the CFD methodology outlined in this dissertation.

6.3.4 Deposition Damage and Surface Roughness

Deposition of particulate matter is another form of damage very often encountered in axial compressors and is described as compressor fouling. Meher-Homji et al. [28] and Kurz and Brun [29] are some of the studies cited earlier in this paper that described fouling mechanisms and illustrated their impact on performance of axial compressors and hence, gas turbine engines. Figure 6.1 shows a compressor blade with deposition damage on the pressure side.



Figure 6.1. Different examples of deposition of particulate matter on axial compressor blades [12]

Fouling impacts the performance of the compressor in two ways by changing the aerodynamic shape of the blade and the roughness of the blade surface. Blades that have sustained deposition damage or 3D printed representative blades could be analyzed for their performance implications by employing the methodology outlined in this dissertation. Further understanding of fouling patterns could lead to better protocols for compressor maintenance and compressor washing. Specifically, understanding the performance degradation due to fouling could lead to cost savings by understanding if the maintenance could be prolonged further and downtime in the operation of gas turbines could be minimized as much as possible. A combined Eulerian-Lagrangian study of deposition using models available in STAR-CCM+ [59] could also be pursued.

Appendix A |

Averaging Techniques

Cumpsty and Horlock [93] have stated that averaging non-uniform flow is important for the analysis of different quantities of interest in turbomachinery and gas turbines, especially with the advent of highly detailed results obtained through CFD. Different quantities require different treatment in order to preserve the essential features of the non-uniform flow.

A.1 Averaging of Stagnation Temperature

The appropriate averaging for stagnation temperature is mass averaging [93] since this gives the correct value of the enthalpy flux, according to the perfect gas assumptions. The mass averaged stagnation pressure is computed using the Equation A.1:

$$\bar{T}_0 = \frac{1}{\dot{m}} \int T_0 d\dot{m} \quad (\text{A.1})$$

where \bar{T}_0 is the mass averaged stagnation temperature, \dot{m} is the total mass flow rate, T_0 is the stagnation temperature of the differential mass flow element $d\dot{m}$.

A.2 Averaging of Stagnation Pressure

The appropriate averaging for stagnation pressure is enthalpy averaging. The expression was given by Pianko and Wazelt [94]. This is the most accurate averaging for flow entering a compressor or turbine as determined by the study conducted by Cumpsty and Horlock [93]. The averaged stagnation pressure should be based on uniform conditions giving work input/output from an ideal compressor or turbine equal to the work with the nonuniform pressure. The enthalpy averaged stagnation pressure is computed using the Equation A.2:

$$\bar{P}_0 = \left(\frac{\int T_0 d\dot{m}}{\int \frac{T_0}{P^{\frac{\gamma-1}{\gamma}}} d\dot{m}} \right)^{\frac{\gamma}{\gamma-1}} \quad (\text{A.2})$$

Bibliography

- [1] AUNGIER, R. (2003) *Axial-flow Compressors: A Strategy for Aerodynamic Design and Analysis*, EngineeringPro collection, ASME Press.
URL <https://books.google.com/books?id=E91SAAAAMAAJ>
- [2] HORLOCK, J. (1958) *Axial Flow Compressors: Fluid Mechanics and Thermodynamics*, Butterworths Scientific Publications.
URL <https://books.google.com/books?id=3SsIAQAIAAJ>
- [3] CUMPSTY, N. (2004) *Compressor Aerodynamics*, no. v. 10 in Compressor aerodynamics, Krieger Pub.
URL <https://books.google.com/books?id=AmM6PgAACAAJ>
- [4] HILL, P. and C. PETERSON (1992) *Mechanics and Thermodynamics of Propulsion*, Addison-Wesley, Reading, MA.
URL <https://books.google.com/books?id=uYJTAAAAMAAJ>
- [5] TARABRIN, A. P., V. A. SCHUROVSKY, A. I. BODROV, and J.-P. STALDER (1998) “An Analysis of Axial Compressor Fouling and a Blade Cleaning Method,” *Journal of Turbomachinery*, **120**(2), pp. 256–261.
URL <https://doi.org/10.1115/1.2841400>
- [6] VAN DONKELAAR, A., R. V. MARTIN, M. BRAUER, R. KAHN, R. LEVY, C. VERDUZCO, and P. J. VILLENEUVE (2010) “Global estimates of ambient fine particulate matter concentrations from satellite-based aerosol optical depth: development and application,” *Environmental health perspectives*, **118**(6), pp. 847–55.
URL <https://doi.org/10.1289/ehp.0901623>
- [7] EL-SAYED, A. (2017) *Aircraft Propulsion and Gas Turbine Engines*, Chap. 13, 2nd ed., CRC Press, Boca Raton, FL, pp. 927–1057.
URL https://books.google.com/books?id=_K0klwEACAAJ
- [8] NEILSON, J. and A. GILCHRIST (1968) “Erosion by a stream of solid particles,” *Wear*, **11**(2), pp. 111–122.
URL [https://doi.org/10.1016/0043-1648\(68\)90591-7](https://doi.org/10.1016/0043-1648(68)90591-7)

- [9] WALSH, W. S., K. A. THOLE, and C. JOE (2006) “Effects of Sand Ingestion on the Blockage of Film-Cooling Holes,” vol. 3: Heat Transfer, Parts A and B of *Turbo Expo: Power for Land, Sea, and Air*, pp. 81–90.
URL <https://doi.org/10.1115/GT2006-90067>
- [10] ZABA, T. and P. LOMBARDI (1984) “Experience in the Operation of Air Filters in Gas Turbine Installations,” vol. 4: Heat Transfer; Electric Power of *Turbo Expo: Power for Land, Sea, and Air*, p. V004T10A009.
URL <https://doi.org/10.1115/84-GT-39>
- [11] OSBORNE, R. E. (1977) “Design of an Industrial Gas Turbine Intake-A Critical Item,” in *Aerospace Meeting*, SAE International.
URL <https://doi.org/10.4271/770968>
- [12] AUST, J. and D. PONS (2019) “Taxonomy of Gas Turbine Blade Defects,” *Aerospace*, **6**, p. 58.
URL <https://doi.org/10.3390/aerospace6050058>
- [13] BALAN, C. and W. TABAKOFF (1984) “Axial flow compressor performance deterioration,” *20th Joint Propulsion Conference*, p. 1280.
URL <https://doi.org/10.2514/6.1984-1208>
- [14] TABAKOFF, W., A. N. LAKSHMINARASIMHA, and M. PASIN (1990) “Simulation of Compressor Performance Deterioration Due to Erosion,” *Journal of Turbomachinery*, **112**(1), pp. 78–83.
URL <https://doi.org/10.1115/1.2927424>
- [15] SALLEE, G. (1978) *Performance Deterioration Based on Existing (historical) Data: JT9D Jet Engine Diagnostics Program*, Tech. Rep. NASA-CR-135448, NASA.
URL <https://ntrs.nasa.gov/citations/19800013837>
- [16] GHENAIET, A., S. C. TAN, and R. L. ELDER (2004) “Experimental investigation of axial fan erosion and performance degradation,” *Proceedings of the Institution of Mechanical Engineers, Part A: Journal of Power and Energy*, **218**(6), pp. 437–450.
URL <https://doi.org/10.1243/0957650041761900>
- [17] "BATCHO, P. F. AND MOLLER, J. C. AND PADOVA, C. AND DUNN, M. G." (1986) *Interpretation of Gas Turbine Response Due to Dust Ingestion*, Tech. Rep. ADA227444, Calspan Advanced Technology Center.
URL <https://apps.dtic.mil/sti/citations/ADA227444>
- [18] BATCHO, P. F., J. C. MOLLER, C. PADOVA, and M. G. DUNN (1987) “Interpretation of Gas Turbine Response Due to Dust Ingestion,” *Journal of*

Engineering for Gas Turbines and Power, **109**(3), pp. 344–352.
URL <https://doi.org/10.1115/1.3240046>

- [19] LI, Y. and A. SAYMA (2012) “Effects of Blade Damage on the Performance of a Transonic Axial Compressor Rotor,” vol. 8: Turbomachinery, Parts A, B, and C of *Turbo Expo: Power for Land, Sea, and Air*, pp. 2427–2437.
URL <https://doi.org/10.1115/GT2012-68324>
- [20] FEDECHKIN, K. S., M. V. KUZMIN, and E. U. MARCHUKOV (2020) “The Design Analysis of the Damaged Compressor Blade Impact on the Aerodynamic Parameters,” vol. 2A: Turbomachinery of *Turbo Expo: Power for Land, Sea, and Air*.
URL <https://doi.org/10.1115/GT2020-16174>
- [21] SUZUKI, M. and M. YAMAMOTO (2011) “Numerical simulation of sand erosion phenomena in a single-stage axial compressor,” *Journal of Fluid Science and Technology*, **6**(1), pp. 98–113.
URL <https://doi.org/10.1299/jfst.6.98>
- [22] SUDER, K. L., R. V. CHIMA, A. J. STRAZISAR, and W. B. ROBERTS (1995) “The Effect of Adding Roughness and Thickness to a Transonic Axial Compressor Rotor,” *Journal of Turbomachinery*, **117**(4), pp. 491–505.
URL <https://doi.org/10.1115/1.2836561>
- [23] MORINI, M., M. PINELLI, P. R. SPINA, and M. VENTURINI (2009) “CFD Simulation of Fouling on Axial Compressor Stages,” vol. 5: Microturbines and Small Turbomachinery; Oil and Gas Applications of *Turbo Expo: Power for Land, Sea, and Air*, pp. 331–342.
URL <https://doi.org/10.1115/GT2009-59025>
- [24] GBADEBO, S. A., T. P. HYNES, and N. A. CUMPSTY (2004) “Influence of Surface Roughness on Three-Dimensional Separation in Axial Compressors,” *Journal of Turbomachinery*, **126**(4), pp. 455–463.
URL <https://doi.org/10.1115/1.1791281>
- [25] SYVERUD, E. and L. E. BAKKEN (2006) “The Impact of Surface Roughness on Axial Compressor Performance Deterioration,” vol. 5: Marine; Microturbines and Small Turbomachinery; Oil and Gas Applications; Structures and Dynamics, Parts A and B of *Turbo Expo: Power for Land, Sea, and Air*, pp. 491–501.
URL <https://doi.org/10.1115/GT2006-90004>
- [26] SYVERUD, E., O. BREKKE, and L. E. BAKKEN (2007) “Axial Compressor Deterioration Caused by Saltwater Ingestion,” *Journal of Turbomachinery*,

- 129**(1), pp. 119–126.
 URL <https://doi.org/10.1115/1.2219763>
- [27] WALTON, K., L. BLUNT, L. FLEMING, M. GOODHAND, and H. LUNG (2014) “Areal parametric characterisation of ex-service compressor blade leading edges,” *Wear*, **321**, pp. 79–86.
 URL <https://doi.org/10.1016/j.wear.2014.10.007>
- [28] MEHER-HOMJI, C. B., M. CHAKER, and A. F. BROMLEY (2006) “The Fouling of Axial Flow Compressors: Causes, Effects, Susceptibility, and Sensitivity,” vol. 4: Cycle Innovations; Industrial and Cogeneration; Manufacturing Materials and Metallurgy; Marine of *Turbo Expo: Power for Land, Sea, and Air*, pp. 571–590.
 URL <https://doi.org/10.1115/GT2009-59239>
- [29] KURZ, R. and K. BRUN (2012) “Fouling Mechanisms in Axial Compressors,” *Journal of Engineering for Gas Turbines and Power*, **134**(3).
 URL <https://doi.org/10.1115/1.4004403>
- [30] NEL, P. (2019) *Computational Fluid Dynamics-Modelling of a Multi-Stage Transonic Axial-Flow Compressor*, Master’s Thesis, Stellenbosch University, Stellenbosch, South Africa.
 URL <https://core.ac.uk/download/pdf/268882973.pdf>
- [31] WILSON, J., R. QIAO, M. KAPPES, J. LOEBIG, and R. CLARKSON (2022) “The Importance of Shape in Particle Rebound Behaviors,” *Journal of Turbomachinery*, **145**(4), 041005.
 URL <https://doi.org/10.1115/1.4055747>
- [32] PEPI, M., R. SQUILLACIOTI, L. PFLEDDERER, and A. PHELPS (2012) “Solid Particle Erosion Testing of Helicopter Rotor Blade Materials,” *Journal of Failure Analysis and Prevention*, **12**(3).
 URL <https://doi.org/10.1007/s11668-011-9531-3>
- [33] OLIANI, S., R. FRISO, N. CASARI, M. PINELLI, A. SUMAN, and M. CARNEVALE (2022) “Progresses in Particle-Laden Flows Simulations in Multistage Turbomachinery With OpenFOAM,” *Journal of Turbomachinery*, **144**(10), 101007.
 URL <https://doi.org/10.1115/1.4054076>
- [34] BRANDES, T., C. KOCH, and S. STAUDACHER (2021) “Estimation of Aircraft Engine Flight Mission Severity Caused by Erosion,” *Journal of Turbomachinery*, **143**(11), 111001.
 URL <https://doi.org/10.1115/1.4051000>

- [35] VULPIO, A., A. SUMAN, N. CASARI, and M. PINELLI (2022) “A Simplified Method for the Deposition Rate Assessment on the Vanes of a Multistage Axial-Flow Compressor,” *Journal of Turbomachinery*, **144**(7), 071009.
URL <https://doi.org/10.1115/1.4053288>
- [36] DÖRING, F., S. STAUDACHER, C. KOCH, and M. WEISSSCHUH (2017) “Modeling Particle Deposition Effects in Aircraft Engine Compressors,” *Journal of Turbomachinery*, **139**(5), 051003.
URL <https://doi.org/10.1115/1.4035072>
- [37] SAXENA, S., G. JOTHIPRASAD, C. BOURASSA, and B. PRITCHARD (2016) “Numerical Simulation of Particulates in Multistage Axial Compressors,” *Journal of Turbomachinery*, **139**(3), 031013.
URL <https://doi.org/10.1115/1.4034982>
- [38] BONIS, J. P., R. PRENTER, and S. WHITAKER (2017) “A Simple Physics-Based Model for Particle Rebound and Deposition in Turbomachinery,” *Journal of Turbomachinery*, **139**(8), p. 081009.
URL <https://doi.org/10.1115/1.4035921>
- [39] SUMAN, A., R. KURZ, N. ALDI, M. MORINI, K. BRUN, M. PINELLI, and P. RUGGERO SPINA (2014) “Quantitative Computational Fluid Dynamics Analyses of Particle Deposition on a Transonic Axial Compressor Blade—Part I: Particle Zones Impact,” *Journal of Turbomachinery*, **137**(2), p. 021009.
URL <https://doi.org/10.1115/1.4028295>
- [40] SUMAN, A., M. MORINI, R. KURZ, N. ALDI, K. BRUN, M. PINELLI, and P. RUGGERO SPINA (2014) “Quantitative Computational Fluid Dynamic Analyses of Particle Deposition on a Transonic Axial Compressor Blade—Part II: Impact Kinematics and Particle Sticking Analysis,” *Journal of Turbomachinery*, **137**(2), p. 021010.
URL <https://doi.org/10.1115/1.4028296>
- [41] YANG, H. and J. BOULANGER (2012) “The Whole Annulus Computations of Particulate Flow and Erosion in an Axial Fan,” *Journal of Turbomachinery*, **135**(1), p. 011040.
URL <https://doi.org/10.1115/1.4006564>
- [42] GHENAIET, A. (2012) “Study of Sand Particle Trajectories and Erosion Into the First Compression Stage of a Turbofan,” *Journal of Turbomachinery*, **134**(5), p. 051025.
URL <https://doi.org/10.1115/1.4004750>
- [43] GHENAIET, A. (2012) “Simulation of Particle Trajectories and Erosion in a Centrifugal Compressor,” *Journal of Turbomachinery*, **134**(5), p. 051022.
URL <https://doi.org/10.1115/1.4004448>

- [44] PARSI, M., K. NAJMI, F. NAJAFIFARD, S. HASSANI, B. S. MCCLAURY, and S. A. SHIRAZI (2014) “A comprehensive review of solid particle erosion modeling for oil and gas wells and pipelines applications,” *Journal of Natural Gas Science and Engineering*, **21**, pp. 850–873.
URL <https://doi.org/10.1016/j.jngse.2014.10.001>
- [45] WHITFIELD, S. (2017), “Managing the Effects of Sand Erosion,,” Retrieved from <https://jpt.spe.org/managing-effects-sand-erosion>.
- [46] EDIRIWEERA, M. (2021) *Impact erosion by solid particles in gas-particle flows*, PhD Thesis, University of South-Eastern Norway, Borre, Norway.
URL <https://hdl.handle.net/11250/2759821>
- [47] SWAMINATHAN, V. P., J. S. SMITH, and D. GANDY (2010) “High-temperature erosion testing standard and round robin testing,” *Advances in Materials Technology for Fossil Power Plants, Proceedings from the 6th International Conference*, pp. 470–486.
- [48] NGUYEN, Q. B., V. B. NGUYEN, C. Y. H. LIM, Q. T. TRINH, S. SANKARANARAYANAN, Y. W. ZHANG, and M. GUPTA (2014) “Effect of impact angle and testing time on erosion of stainless steel at higher velocities,” *Wear*, **321**, pp. 87–93.
URL <https://doi.org/10.1016/j.wear.2014.10.010>
- [49] MANSOURI, A. (2021) *Impact erosion by solid particles in gas-particle flows*, PhD Thesis, University of South-Eastern Norway, Borre, Norway.
URL <https://hdl.handle.net/11250/2759821>
- [50] LÓPEZ, A., M. T. STICKLAND, and W. M. DEMPSTER (2018) “CFD study of fluid flow changes with erosion,” *Computer Physics Communications*, **227**, pp. 27–41.
URL <https://doi.org/10.1016/j.cpc.2018.02.002>
- [51] NGUYEN, V., Q. NGUYEN, Z. LIU, S. WAN, C. LIM, and Y. ZHANG (2014) “A combined numerical–experimental study on the effect of surface evolution on the water–sand multiphase flow characteristics and the material erosion behavior,” *Wear*, **319**(1), pp. 96–109.
URL <https://doi.org/10.1016/j.wear.2014.07.017>
- [52] AGRAWAL, M., S. KHANNA, A. KOPLIKU, and T. LOCKETT (2019) “Prediction of sand erosion in CFD with dynamically deforming pipe geometry and implementing proper treatment of turbulence dispersion in particle tracking,” *Wear*, **426–427**, pp. 596–604, 22nd International Conference on Wear of Materials.
URL <https://doi.org/10.1016/j.wear.2019.01.018>

- [53] DUARTE, C. A. R. and F. J. DE SOUZA (2021) “Dynamic mesh approaches for eroded shape predictions,” *Wear*, **484-485**, p. 203438.
URL <https://doi.org/10.1016/j.wear.2020.203438>
- [54] GE Aviation *T700-401C/-701C Turboshift Engines Data Sheet*.
URL <https://www.ge.com/aviation>
- [55] KENNEDY, R. (2005), “GE’s T700/CT7 Engine Family Continues Its Pattern of Growth, Enhancement and Success,,” Retrieved from: <https://www.ge.com/news/press-releases/ges-t700ct7-engine-family-continues-its-pattern-growth-enhancement-and-success-0>.
- [56] CUTAWAYCREATIONS (2018), “GE Black Hawk T700 Engine,,” Retrieved from: <https://youtu.be/-Ox1wMXBo-A>.
- [57] Dassault Systèmes *SolidWorks 2020 Essentials*.
URL <https://www.solidworks.com/sw/support>
- [58] ZUNIGA, V. and M. OSVALDO (2007) *Analysis of gas turbine compressor fouling and washing on line*, PhD Thesis, Cranfield University, Cranfield, UK.
URL <http://hdl.handle.net/1826/2448>
- [59] Siemens *STAR-CCM+ v2021.1, User Manual*.
- [60] Pointwise, Inc. *Pointwise V18.2 R2, User Manual*.
- [61] ROE, P. L. (1981) “The use of the Riemann problem in finite difference schemes,” in *Seventh International Conference on Numerical Methods in Fluid Dynamics* (W. C. Reynolds and R. W. MacCormack, eds.), Springer Berlin Heidelberg, Berlin, Heidelberg, pp. 354–359.
URL https://doi.org/10.1007/3-540-10694-4_54
- [62] FERZIGER, J. H., M. PERIĆ, and R. L. STREET (2002) *Computational Methods for Fluid Dynamics*, Springer, Berlin, Germany.
URL <https://doi.org/10.1007/978-3-642-56026-2>
- [63] MENTER, F. R. (1994) “Two-equation eddy-viscosity turbulence models for engineering applications,” *AIAA Journal*, **32**(8), pp. 1598–1605.
URL <https://doi.org/10.2514/3.12149>
- [64] MENTER, F. and C. RUMSEY “Assessment of two-equation turbulence models for transonic flows,” in *Fluid Dynamics Conference*.
URL <https://arc.aiaa.org/doi/abs/10.2514/6.1994-2343>
- [65] ARAYA, G. (2019) “Turbulence Model Assessment in Compressible Flows around Complex Geometries with Unstructured Grids,” *Fluids*, **4**(2).
URL <https://www.mdpi.com/2311-5521/4/2/81>

- [66] BALASUBRAMANIAN, R., S. BARROWS, and J. CHEN “Investigation of Shear-Stress Transport Turbulence Model for Turbomachinery Applications,” in *46th AIAA Aerospace Sciences Meeting and Exhibit*.
URL <https://arc.aiaa.org/doi/abs/10.2514/6.2008-566>
- [67] REID, L. and R. D. MOORE (1978) *Performance of single-stage axial-flow transonic compressor with rotor and stator aspect ratios of 1.19 and 1.26, respectively, and with design pressure ratio of 1.82,, Tech. Rep. NASA-TP-1338*, NASA.
URL <https://ntrs.nasa.gov/citations/19790001889>
- [68] SUDER, K. L. (1996) *Experimental investigation of the flow field in a transonic, axial flow compressor with respect to the development of blockage and loss,, Tech. Rep. NASA-TM-107310*, NASA.
URL <https://ntrs.nasa.gov/citations/19970001675>
- [69] AMERI, ALI (2009) *NASA Rotor 37 CFD code validation using Glenn-HT code, Tech. Rep. NASA/CR-2010-216235*, NASA.
URL <https://ntrs.nasa.gov/citations/20100029589>
- [70] BRUNA, D. and M. G. TURNER (2013) “Isothermal Boundary Condition at Casing Applied to the Rotor 37 Transonic Axial Flow Compressor,” *Journal of Turbomachinery*, **135**(3), 034501.
URL <https://doi.org/10.1115/1.4007569>
- [71] SHABBIR, A., M. L. CELESTINA, J. J. ADAMCZYK, and A. J. STRAZISAR (1997) “The Effect of Hub Leakage Flow on Two High Speed Axial Flow Compressor Rotors,” vol. 1: Aircraft Engine; Marine; Turbomachinery; Microturbines and Small Turbomachinery of *Turbo Expo: Power for Land, Sea, and Air*, v02AT32A071.
URL <https://doi.org/10.1115/97-GT-346>
- [72] DENTON, J. D. (1997) “Lessons from Rotor 37,” *Journal of Thermal Science*, **6**(1), pp. 1–13.
URL <https://doi.org/10.1007/s11630-997-0010-9>
- [73] YAMADA, K., M. FURUKAWA, T. NAKANO, M. INOUE, and K. FUNAZAKI (2004) “Unsteady Three-Dimensional Flow Phenomena Due to Breakdown of Tip Leakage Vortex in a Transonic Axial Compressor Rotor,” vol. 5: Turbo Expo, Parts A and B of *Turbo Expo: Power for Land, Sea, and Air*, pp. 515–526.
URL <https://doi.org/10.1115/GT2004-53745>
- [74] CHIRAYATH, E., H. XU, X. YANG, and R. KUNZ (2023) “Full Stage Axial Compressor Performance Modeling Incorporating the Effects of Blade Damage

- Due to Particle Ingestion,” *Journal of Turbomachinery*, **145**(9), p. 091001.
URL <https://doi.org/10.1115/1.4062397>
- [75] CHIRAYATH, E., H. XU, X. YANG, and R. KUNZ (2021) “Modeling Effects of Transonic Axial Compressor Performance Degradation due to Rotor Blade Damage,” in *APS Division of Fluid Dynamics Meeting Abstracts*, APS Meeting Abstracts, p. M28.009.
URL <https://ui.adsabs.harvard.edu/abs/2021APS..DFDM28009C>
- [76] DENTON, J. D. (1993) “Loss Mechanisms in Turbomachines,” vol. 2: Combustion and Fuels; Oil and Gas Applications; Cycle Innovations; Heat Transfer; Electric Power; Industrial and Cogeneration; Ceramics; Structures and Dynamics; Controls, Diagnostics and Instrumentation; of *Turbo Expo: Power for Land, Sea, and Air*, pp. 515–526.
URL <https://doi.org/10.1115/93-GT-435>
- [77] KOCH, C. C. and J. SMITH, L. H. (1976) “Loss Sources and Magnitudes in Axial-Flow Compressors,” *Journal of Engineering for Power*, **98**(3), pp. 411–424.
URL <https://doi.org/10.1115/1.3446202>
- [78] BELAMRI, T., P. GALPIN, A. BRAUNE, and C. CORNELIUS (2005) “CFD Analysis of a 15 Stage Axial Compressor: Part II — Results,” vol. 6: Turbo Expo 2005, Parts A and B of *Turbo Expo: Power for Land, Sea, and Air*, pp. 1009–1017.
URL <https://doi.org/10.1115/GT2005-68262>
- [79] BURBERI, C., V. MICHELASSI, A. SCOTTI DEL GRECO, S. LORUSSO, L. TAPINASSI, M. MARCONCINI, and R. PACCIANI (2020) “Validation of steady and unsteady CFD strategies in the design of axial compressors for gas turbine engines,” *Aerospace Science and Technology*, **107**, p. 106307.
URL <https://doi.org/10.1016/j.ast.2020.106307>
- [80] BROWN, R. N. (2005) “6 - Axial Compressors,” in *Compressors (Third Edition)* (R. N. Brown, ed.), third edition ed., Gulf Professional Publishing, Burlington, pp. 262–294.
URL <https://doi.org/10.1016/B978-075067545-1/50008-0>
- [81] SCHILLER, V. L. (1933) “Über die grundlegenden Berechnungen bei der Schwerkraftaufbereitung,” *Z. Vereines Deutscher Inge.*, **77**, pp. 318–321.
- [82] AUTON, T. R., J. C. R. HUNT, and M. PRUD’HOMME (1988) “The force exerted on a body in inviscid unsteady non-uniform rotational flow,” *Journal of Fluid Mechanics*, **197**, p. 241–257.
URL <https://doi.org/10.1017/S0022112088003246>

- [83] TILLY, G. (1979) “Erosion Caused by Impact of Solid Particles,” *Treatise on Materials Science and Technology*, Elsevier, pp. 287–319.
URL [https://doi.org/10.1016/S0161-9160\(13\)70071-1](https://doi.org/10.1016/S0161-9160(13)70071-1)
- [84] RAASK, E. (1969) “Tube erosion by ash impaction,” *Wear*, **13**(4), pp. 301–315.
URL [https://doi.org/10.1016/0043-1648\(69\)90252-X](https://doi.org/10.1016/0043-1648(69)90252-X)
- [85] OKA, Y., H. OHNOGI, T. HOSOKAWA, and M. MATSUMURA (1997) “The impact angle dependence of erosion damage caused by solid particle impact,” *Wear*, **203-204**, pp. 573–579, 11th International Conference on Wear of Materials.
URL [https://doi.org/10.1016/S0043-1648\(96\)07430-3](https://doi.org/10.1016/S0043-1648(96)07430-3)
- [86] OKA, Y., K. OKAMURA, and T. YOSHIDA (2005) “Practical estimation of erosion damage caused by solid particle impact: Part 1: Effects of impact parameters on a predictive equation,” *Wear*, **259**(1), pp. 95–101, 15th International Conference on Wear of Materials.
URL <https://doi.org/10.1016/j.wear.2005.01.039>
- [87] OKA, Y. and T. YOSHIDA (2005) “Practical estimation of erosion damage caused by solid particle impact: Part 2: Mechanical properties of materials directly associated with erosion damage,” *Wear*, **259**(1), pp. 102–109, 15th International Conference on Wear of Materials.
URL <https://doi.org/10.1016/j.wear.2005.01.040>
- [88] HAUGEN, K., O. KVERNOLD, A. RONOLD, and R. SANDBERG (1995) “Sand erosion of wear-resistant materials: Erosion in choke valves,” *Wear*, **186-187**, pp. 179–188, 8th International Conference on Erosion by Liquid and Solid Impact.
URL [https://doi.org/10.1016/0043-1648\(95\)07158-X](https://doi.org/10.1016/0043-1648(95)07158-X)
- [89] ZHANG, Y., E. REUTERFORS, B. MCCLAURY, S. SHIRAZI, and E. RYBICKI (2007) “Comparison of computed and measured particle velocities and erosion in water and air flows,” *Wear*, **263**(1), pp. 330–338, 16th International Conference on Wear of Materials.
URL <https://doi.org/10.1016/j.wear.2006.12.048>
- [90] PENG, W. and X. CAO (2016) “Numerical prediction of erosion distributions and solid particle trajectories in elbows for gas–solid flow,” *Journal of Natural Gas Science and Engineering*, **30**, pp. 455–470.
URL <https://doi.org/10.1016/j.jngse.2016.02.008>
- [91] GRANT, G. and W. TABAKOFF (1975) “Erosion Prediction in Turbomachinery Resulting from Environmental Solid Particles,” *Journal of Aircraft*, **12**(5), pp.

471–478.

URL <https://doi.org/10.2514/3.59826>

- [92] EDWARDS, V. R. and P. L. ROUSE (1994) “US Army rotorcraft turboshaft engines sand and dust erosion considerations,” 83rd Symposium on Propulsion and Energetic Panels on Erosion, Corrosion and Foreign Object Damage Effects in Gas Turbines, pp. 3–1 – 3–10.

URL <https://apps.dtic.mil/sti/citations/ADA289820>

- [93] CUMPSTY, N. A. and J. H. HORLOCK (2005) “Averaging Nonuniform Flow for a Purpose,” *Journal of Turbomachinery*, **128**(1), pp. 120–129.

URL <https://doi.org/10.1115/1.2098807>

- [94] PIANKO, M. AND WAZELT, F. (1983) *Propulsion and Energetics Panel Working Group 14 on Suitable Averaging Techniques in Non-Uniform Internal Flows*, Tech. Rep. ADA133968, AGARD.

URL <https://apps.dtic.mil/sti/citations/ADA133968>

Vita

Emanuel Chirayath

Emanuel Chirayath is doctoral candidate in the Department of Mechanical Engineering in The Pennsylvania State University since Fall 2018. Emanuel received his Bachelor of Technology (B.Tech) in Mechanical Engineering from the National Institute of Technology Calicut, India in May 2014 and Master of Science in Engineering (M. S. E.) from the University of Michigan Ann Arbor in December 2015. Emanuel's primary research interest is in the simulation and studying the effects of particle ingestion in the cold section of gas turbine engines.

Research Publications

1. **Chirayath, E.**, Xu, H., Yang, X., and Kunz, R. (2023) "*Full Stage Axial Compressor Performance Modeling Incorporating the Effects of Blade Damage due to Particle Ingestion,*" ASME Journal of Turbomachinery, 145(9): 091001. <https://doi.org/10.1115/1.4062397>
2. **Chirayath, E.**, Xu, H., Yang, X., Kunz, R. (2021) Modeling Effects of Transonic Axial Compressor Performance Degradation due to Rotor Blade Damage. Presented at the 74th Annual Meeting of the APS Division of Fluid Dynamics. November 21-23, 2021. Phoenix, USA.
3. Ishiyama, C., Miyazaki, K., Harvey, C., **Chirayath, E.**, Matsuoka, K., Kasahara, J., Matsuo, A., Funaki, I. (2015) Research and Development of Centrifugal-Compressor-Axial-Turbine Type Rotating Detonation Engine. Presented at the 53rd Symposium (Japanese) on Combustion. November 16-18, 2015. Tsukuba, Japan.